UNIVERSIDAD DE CONCEPCIÓN
FACULTAD DE CIENCIAS FÍSICAS Y MATEMÁTICAS

Origin of magnetism in early-type stars

Protostellar magnetic fields and core dynamo.

Origen del magnetismo en estrellas de tipo temprano

Campos magnéticos protoestelares y dínamo del núcleo.

Profesor Guía: Dominik Schleicher

Departamento de Astronomía
Facultad de Ciencias Físicas y Matemáticas
Universidad de Concepción

Tesis presentada a la Dirección de Postgrado de la Universidad de Concepción para optar al grado académico de Magíster en Astronomía

Juan Pablo Sebastián Hidalgo Rivas

Noviembre de 2023

Concepción, Chile

Acknowledgements

I would like to express my gratitude to all the people with whom I shared experiences during this process, contributing to the development of this thesis.

First, to my whole family from Iquique (including my cat), giving special remarks to my mother Alejandra Rivas, who always believed in me and gave me her unconditional support. I express my absolute gratitude to my partner Dr. Paulina Karczmarek, whose support, suggestions, love, scientific conversations, time spent in La Cocina, and outlook on life defined fundamental parts of who I am today, learning that there is more out there than just equations. Special thanks to my friends Matías and Dani, with whom I shared relevant time during my master studies (and before).

I thank Dr. Dominik Schleicher, my supervisor; his knowledge, support, useful comments, and guidance have been a fundamental part of the development of my scientific career. I would also like to express my gratitude to Dr. Petri Käpylä, who provided the setup used in this project. Without his knowledge, innovate ideas, patience, and the time I spent in Freiburg, this thesis would not be as it is now. Finally, thanks to Dr. Felipe Navarrete and Carolina Ortiz-Rodríguez, who helped me a lot to solve code problems with very useful discussions during our meetings.

Financial support from Fondecyt Regular (project code 1201280) and ANID BASAL project FB210003 is gratefully acknowledged. Special thanks to SOCHIAS, and the support provided by Beca Adelina Gutierrez. The simulations were performed using the KULTRUN cluster at the Astronomy Department of the Universidad de Concepción.

Resumen

Las estrellas de tipo temprano tienen envolturas radiativas con núcleos convectivos debido a un fuerte gradiente de temperatura producido por el ciclo CNO. Las estrellas químicamente peculiares Ap y Bp poseen campos magnéticos de gran escala desde 200 G hasta 34 kG. El origen de estos campos magnéticos es incierto, pero se han desarrollado algunas hipótesis. En la primera parte de esta tesis, presentamos simulaciones magnetohidrodinámicas (MHD) en 3D de una estrella con $2M_{\odot}$ totalmente convectiva, como una forma de modelar su fase protoestelar y encontrar campos magnéticos *fósiles*, que eventualmente podrían permanecer estables durante su vida en la secuencia principal. Encontramos configuraciones de dínamo en su mayoría estacionarias con rotación diferencial anti-solar, similar a lo que se ha encontrado previamente en estrellas totalmente convectivas. En la segunda parte de este trabajo, presentamos simulaciones numéricas en 3D de una estrella con $2M_{\odot}$ de secuencia principal con un núcleo convectivo que ocupa el 20% su extensión radial, rodeado por una envoltura radiativa, como una forma de estudiar el magnetismo producido por el dinamo del núcleo, y por primera vez, la relación entre su cíclo magnético y el periodo de rotación de la estrella. Exploramos periodos de rotación de 8 a 20 días, y definimos tres sets de simulaciones, cuyas principales diferencias son el perfil radial de las difusividades, y el tamaño de la caja, lo que nos permite explorar no sólo el magnetismo en el núcleo, sino también en la superficie. Todos los modelos con núcleos convectivos tienen rotación diferencial solar y generan dínamos hemisféricos con valores del campo magnético toroidal muy fuertes de hasta 200 kG. En los rotadores rápidos la energía magnética es cercana a la energía cinética, alcanzando un régimen cercano a la equipartición. La superficie estelar también tiene campos magnéticos, sin embargo, son débiles en todas partes excepto en los polos, lo que al igual que resultados anteriores, parece indicar que un dínamo en el núcleo no es suficiente para explicar los campos magnéticos observados en estas estrellas. Finalmente, este modelo se puede utilizar para estudiar cómo un campo fósil inicial cambia la naturaleza del dínamo hemisférico en el núcleo, y también el campo magnético a gran escala resultante.

Keywords – Campos magnéticos, estrellas de tipo temprano, magnetohidrodinámica (MHD), dínamos

Abstract

Early-type stars have radiative envelopes and convective cores due to a steep temperature gradient produced by the CNO cycle. The chemically peculiar Ap and Bp stars host large-scale magnetic fields in the order of 200 G to 34 kG. The origin of these magnetic field remains uncertain, although, some hypotheses have been developed. In the first part of this thesis, we present 3D magnetohydrodynamical (MHD) simulations of a fully convective $2M_{\odot}$ star, as a way to model the protostellar phase of the star and find *fossil* magnetic field configurations, that could eventually remain stable during the main-sequence life of the star. We find mostly steady dynamo configurations with anti-solar differential rotation, similar to what has been found previously in fully convective stars. In the second part of this work, we present 3D numerical simulations of a $2M_{\odot}$ main-sequence star with a convective core of 20% its radial extent, surrounded by a radiative envelope, as a way to study the magnetism produced by a core dynamo, and for the first time, the relation between its magnetic cycle and the rotation period of the star. We explore rotation periods from 8 to 20 days, and defined three sets of simulations, whose main differences are the radial profiles of the diffusivities, and the size of the box, allowing us to explore not only the magnetism in the core, but also at the surface. All the convective core models have solar-like differential rotation and drive dynamos which are hemispheric with very strong toroidal magnetic fields up to 200 kG. In the fast rotators the magnetic energy is close to the kinetic energy, reaching a nearly equipartition regime. The stellar surface also has magnetic fields, however, they are weak everywhere except at the poles, which similarly to previous results, seems to indicate that a core dynamo is not enough to explain the observed magnetic fields of these stars. Finally, this model can be used to study how an initial fossil field changes the nature of the hemispheric core dynamo, and also the resulting large-scale magnetic field.

Keywords – Magnetic fields, early-type stars, magnetohydrodynamics (MHD), dynamos

Contents

ACKNOWLEDGEMENTS i

Resumen ii

Abstract iii

1 Introduction 1
- 1.1 Context . . . 1
- 1.2 Magnetic fields . . . 3
  - 1.2.1 Solar magnetism . . . 3
  - 1.2.2 Ap/Bp stars magnetism . . . 4
- 1.3 Possible explanations of magnetism in early-type stars . . . 6
  - 1.3.1 A dynamo driven in the convective core . . . 6
  - 1.3.2 Fossil fields . . . 8
  - 1.3.3 Dynamo in the radiative zone . . . 9
- 1.4 This project . . . 10

2 Stellar structure and magnetohydrodynamics 12
- 2.1 Energy transport mechanisms . . . 12
  - 2.1.1 Radiation . . . 13
  - 2.1.2 Convection . . . 14
    - 2.1.2.1 Convective stability . . . 15
    - 2.1.2.2 Mixing length theory . . . 16
- 2.2 Magnetohydrodynamics . . . 17
  - 2.2.1 The induction equation . . . 17
  - 2.2.2 Full set of non-ideal MHD equations . . . 19
  - 2.2.3 Dimensionless numbers . . . 22

3 Numerical models and methods 24
- 3.1 MESA code . . . 24
  - 3.1.1 Online version . . . 24
  - 3.1.2 Input parameters . . . 25
  - 3.1.3 A-type star model . . . 25
- 3.2 The Pencil code . . . 27
  - 3.2.1 Modularity . . . 28

3.2.2 Files in the run directories . . . 29
3.2.3 Output files . . . 30
3.3 The models . . . 31
3.3.1 Whole star setup . . . 31
3.3.2 Zoom setup . . . 35
3.3.3 Physical units and relation to reality . . . 36
3.3.4 Diagnostic quantities . . . 38

4 Three-dimensional MHD simulations of a fully convective star: protostellar phase 39
4.1 Simulations . . . 39
4.2 Dynamo solutions . . . 40
4.3 Large-scale flows . . . 43
4.4 Energy analysis . . . 47
4.5 Spherical harmonic decomposition and power spectra . . . 48

5 Simulations of the dynamo driven by the convective core of the star: main-sequence phase 52
5.1 Simulations . . . 52
5.1.1 Root-mean-square magnetic fields . . . 53
5.1.2 Stratification . . . 54
5.2 Dynamo solutions . . . 56
5.2.1 Dynamos driven in the core . . . 57
5.2.2 Surface magnetic fields . . . 60
5.3 Large-scale flows . . . 62
5.4 Rotational scaling of magnetic cycles . . . 68
5.5 Energy analysis . . . 70
5.5.1 Global and core energies . . . 70
5.5.2 Energy fluxes and luminosities . . . 72
5.6 Power Spectra . . . 74

6 Summary and conclusions 77

Bibliography 81

List of Tables

3.1.1 Stellar parameters obtained from the 2 $M_\odot$ MESA-Web model, averaged over a time range from $t = 2.5 \cdot 10^6$ years to $t = 4.5 \cdot 10^8$ years. 26
3.3.1 Dimensionless luminosities computed with the simulation and stellar parameters, for the protostar (fully convective) and the main-sequence (partially convective) models. The third column gives the ratio between both. 37

4.1.1 Summary of all the fully convective model runs. From left to right the columns correspond to the rotation period $P_{\rm rot} = 2\pi/\Omega_0$, the volume-averaged root-mean-square flow velocity $\langle u_{\rm rms}\rangle$, the volume-averaged root-mean-square magnetic field $\langle B_{\rm rms}\rangle$, the Coriolis number, the Reynolds number and the magnetic Reynolds number (which equals the SGS Péclet number in both groups). 40
4.3.1 Differential rotation parameters for all simulations, obtained from the averaged (azimuthally and temporally) angular velocity $\overline{\Omega}(r,\theta)$. 44
4.4.1 Kinetic and magnetic energies, averaged over time and volume. The total kinetic and magnetic energies have units of 10^{35}J, while the rest of energies are written as fractions of these quantities. . . 48

5.1.1 Summary of all the "main-sequence" model runs. From left to right the columns correspond to the rotation period $P_{\rm rot} = 2\pi/\Omega_0$, the volume-averaged (over the convective zone) root-mean-square flow velocity $\langle u_{\rm rms}\rangle$, the volume-averaged root-mean-square magnetic field $\langle B_{\rm rms}\rangle$, the Coriolis number, the SGS Péclet number, the fluid and magnetic Reynolds numbers. 53
5.2.1 Maximum, root-mean-square, and minimum value of the averaged toroidal magnetic field at $r = 0.2R$ from groups MHD, MHD* and zMHD. 60
5.3.1 Differential rotation parameters for all simulations, obtained from the averaged (azimuthally and temporally) angular velocity $\overline{\Omega}(r,\theta)$. 63
5.4.1 Magnetic cycle period $P_{\rm cyc,c}$, and the averaged rotation period $P_{\rm rot,c} = 2\pi/\overline{\Omega}$ at $r = 0.2R$. 68

5.5.1 Kinetic and magnetic energies, averaged over time and volume. The total kinetic and magnetic energies have units of 10^{33}J, while the rest of energies are written as fractions of these quantities. . . 71

List of Figures

1.1.1 Internal structure of main-sequence stars, where closed curves represent convection and open arrows radiation. The diagrams of each spectral type (mentioned above the star) are examples of stars inside the corresponding mass range. 2
1.2.1 Solar butterfly diagram showing sunspots as a function of time and latitude (with EQ being the equator). Courtesy of Dr. David Hathaway and NASA. 4
1.2.2 Time evolution of the averaged solar surface magnetic field (Butterfly diagram) from 1975 to 2015. Image adapted from Charbonneau (2014). 5
1.2.3 Histogram of best fit dipole field strengths, from the sample of 27 Ap/Bp stars described in Aurière et al. (2007). 6

3.1.1 The superadiabaticity $\nabla - \nabla_{\rm ad}$, where the dashed line is the Schwarzschild criterion (*upper panel*) and the convective velocity (*lower panel*) of the MESA-Web models for a 2 $M_\odot$ A-type star, at $t_{\rm age} = 2.26 \cdot 10^8$ year. 27

4.1.1 *Top panel*: Density profile from Ar1 and Br1. *Bottom panel*: Entropy profiles from the same runs. Both quantities are time-averaged over the thermally relaxed times. 41
4.1.2 Temperature profile from Ar1 and Br1. $\overline{T}$ is averaged over the thermally relaxed times. 41
4.2.1 Time-latitude diagrams of the azimuthally averaged toroidal magnetic field $\overline{B}_\phi(R, \theta, t)$, where the run is indicated in the upper left, and the minimum and maximum field strength at the bottom of each panel. 42
4.3.1 Profiles of the temporally and azimuthally averaged rotation rate $\overline{\Omega}(\varpi, z)$ for runs from group A. The colorbar was clipped in some cases to highlight different features in the plot. The maximum and minimum values are indicated in parenthesis above and below the colorbar. The streamlines indicate the mass flux due to meridional circulation and the dotted line is the equator. 45
4.3.2 Rotation profiles $\overline{\Omega}(\varpi, z)$. Same as Figure 4.3.1, but for runs from group B. 46

4.3.3 Snapshot from run Ar3 at $t = 115$ [yr]. The left plot corresponds to the equatorial plane, and the middle and right plots to the planes that contain the axis of rotation (zx and zy respectively). The colorbar represents the radial component of the flow velocity u_r. . 47
4.5.1 Power spectra of the velocity ($E_{\rm K}$) and the magnetic field ($E_{\rm M}$). The solid line represents the radial component, the dotted line the horizontal, and the dashed (slightly darker) line the non-axisymmetric contributions ($m \neq 0$). 51

5.1.1 Time evolution of the volume-averaged root-mean-square magnetic field from the runs in MHD group that generate core dynamos. . . 54
5.1.2 *Top panel*: Density profile from the slowest rotating run (with no dynamo), and the magnetic slowest rotators. *Lower panel*: Entropy profiles from the same runs. Both quantities are time-averaged over the thermally relaxed phase. 55
5.1.3 Temperature profile from same runs as in Figure 5.1.2. $\overline{T}$ is averaged over the thermally relaxed phase. 55
5.1.4 Density, entropy (*upper panel*) and temperature (*lower panel*) profiles from the simulations from group zMHD. All the quantities are averaged over the thermally relaxed phase. 56
5.2.1 Time-latitude diagrams of the azimuthally averaged toroidal magnetic field $\overline{B}_\phi(r = 0.2R, \theta, t)$ of the MHD group, where the run is indicated in the upper left of each plot. 58
5.2.2 Time-latitude diagrams of the azimuthally averaged toroidal magnetic field $\overline{B}_\phi(r = 0.2R, \theta, t)$ of the MHD* group, where the run is indicated in the upper left of each plot. 59
5.2.3 Time-latitude diagrams of the azimuthally averaged toroidal magnetic field $\overline{B}_\phi(r = 0.2R, t)$ from run zMHDr2. 60
5.2.4 Time-latitude diagrams of the azimuthally averaged toroidal magnetic field $\overline{B}_\phi(r = R, \theta, t)$ of the groups MHD (*left*) and MHD* (*right*), where the run is indicated in the upper left of each plot. . 61
5.3.1 Profile of the temporally and azimuthally averaged rotation rate $\overline{\Omega}(\varpi, z)$ for MHDr3 in the whole star. 62
5.3.2 Profiles of the temporally and azimuthally averaged rotation rate $\overline{\Omega}(\varpi, z)$ for runs from the MHD group. The streamlines indicate the mass flux due to meridional circulation and the maximum averaged meridional flow is indicated in the lower left side of each plot. The dashed line represents the equator. 64
5.3.3 Profiles of the temporally and azimuthally averaged rotation rate $\overline{\Omega}(\varpi, z)$. Same as Figure 5.3.2 but for runs from the MHD* group. 65
5.3.4 Snapshot from MHDr3 at $t = 82$ [yr]. The left plot corresponds to the equatorial plane, and the middle and right plots to the planes that contain the axis of rotation (zx and zy respectively). The colorbar represents the radial component of the flow velocity u_r. . 66
5.3.5 Profiles of the temporally and azimuthally averaged rotation rate $\overline{\Omega}(\varpi, z)$. Same as Figure 5.3.2 but for runs from the zMHD group. 67

5.3.6 Snapshot from zMHDr2 at $t = 68$ [yr]. The left plot corresponds to the equatorial plane, and the middle and right plots to the planes that contain the axis of rotation (zx and zy respectively). The colorbar represents the radial component of the flow velocity u_r. . 67
5.4.1 The magnetic cycle period $P_{\rm cyc,c}$ as a function of the averaged rotation period of the core $P_{\rm rot,c}$. The dashed lines are the best power-law fits to the data. 69
5.4.2 Ratios of rotation to cycle period as a function of the Coriolis number. Simulations from groups MHD and MHD* are indicated in blue and orange respectively. Additional data are from (Strugarek et al., 2018, red), and (Warnecke, 2018, purple). The dashed lines are the best power-law fits to the data. 70
5.5.1 Temporal evolution of the magnetic (blue) and kinetic (orange) energies extracted from the time series of the runs MHDr2 (*left*) and MHDr4 (*right*). 72
5.5.2 Luminosity contributions from kinetic energy, enthalpy, radiative, cooling and heating fluxes from MHDr2* (*left panel*) and MHDr3 (*right panel*). 73
5.5.3 Luminosity contributions from zMHDr1 (*left panel*) and zMHDr2 (*right panel*). 74
5.6.1 Power spectra of the velocity ($E_{\rm K}$) and the magnetic field ($E_{\rm M}$). The solid line represents the radial component, the dotted line the horizontal, and the dashed (slightly darker) line the non-axisymmetric contributions ($m \neq 0$). 75
5.6.2 Same as Figure 5.6.1, but for run zMHDr2. 76

Chapter 1

Introduction

1.1 Context

Magnetic fields are everywhere in the Universe. It is possible to infer them in a lot of astrophysical systems, like terrestrial and gas planets, galaxies, accretion disks, and in the interstellar medium. They can also be found in a wide variety of stars, and there is a general consensus that most of them are amplified and maintained via self-excited dynamos. In this context, these processes typically require rotation and convection, and therefore are most likely to occur inside convection zones (see Brandenburg and Subramanian 2005). The most obvious example is the Sun, which has a cyclic large-scale magnetic field driven by a self-excited dynamo operating in its convective envelope. This field can be measured directly from the surface of the Sun with the Zeeman effect in the sunspots spectra (see Section 1.2.1). Like the Sun, other late-type stars (M, K, F) have convective envelopes, and the observed magnetic field in these stars also has a convective-driven origin. An interesting example are M dwarfs, which are believe to be fully convective with masses below $M \approx 0.35\ M_{\odot}$ (see Kochukhov, 2021). Numerical simulations have reproduced different dynamos coming from these stars (Dobler et al., 2006; Browning, 2008; Brown et al., 2020; Käpylä, 2021; Ortiz-Rodríguez et al., 2023).

Early-type stars are main-sequence stars with higher masses ($M > 1.5 M_{\odot}$) and temperatures than late-type stars and only roughly 5% are magnetic (Kochukhov and Bagnulo, 2006). According to our understanding of stellar evolution, stars

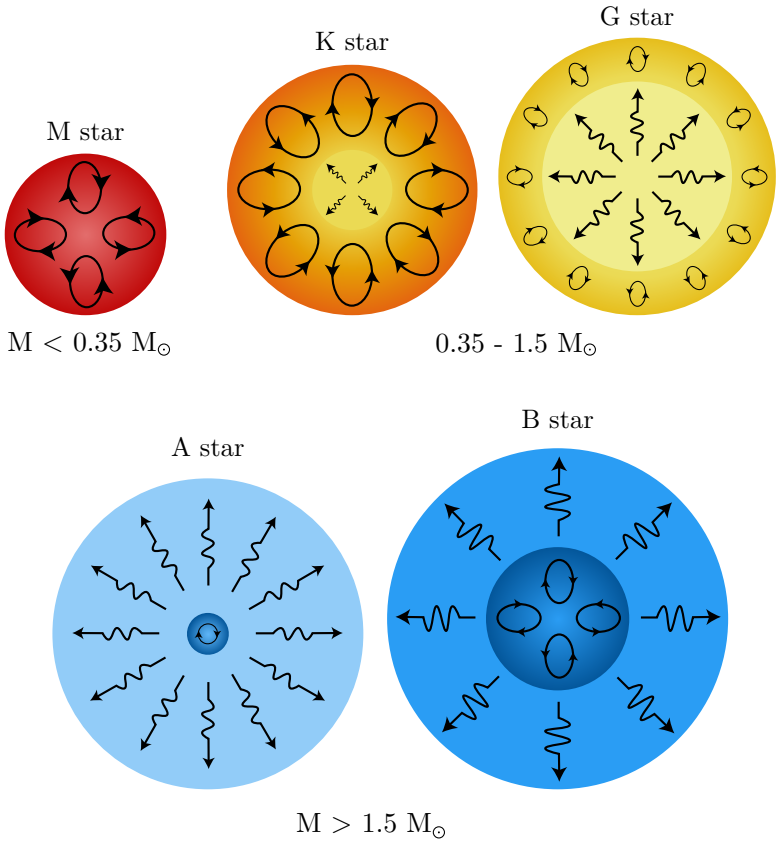

Figure 1.1.1: Internal structure of main-sequence stars, where closed curves represent convection and open arrows radiation. The diagrams of each spectral type (mentioned above the star) are examples of stars inside the corresponding mass range.

with masses above ~ 1.5 M$_\odot$ have stably stratified envelopes, this means that they are stable against convection and therefore, energy is transported by radiation (see Figure 1.1.1). This might explain why a dynamo can not usually operate at the surface of these stars, since in principle vigorous convective motions are required (see Section 2.2.1). However, some stars in the range of $1.5\ M_\odot - 6\ M_\odot$ host observable large-scale magnetic fields. A good example is the subgroup of chemically peculiar main-sequence stars, classified as Ap/Bp. These stars host magnetic fields with mean field strengths ranging from 200 G to 30 kG (Aurière et al., 2007), while the highest magnetic field detected, coming from HD 215441, reached 34 kG (Babcock, 1960). Roughly 10% of A-type stars belong to the sub-classification Ap and have detectable strong fields (Moss, 2001). Furthermore, Grunhut et al. (2017) analyzed 108 individual O-type stars finding a magnetic incident rate of $7 \pm 3\%$, which might indicate a similar distribution as in Ap/Bp

stars, although magnetic fields of O-type stars are much weaker. This is one of the reasons of why we will focus more in Ap/Bp stars in this thesis. More information about these stars is given in Section 1.2.2.

Unlike late-type stars, whose magnetic fields (believed to be dynamo originated) have complex surface structures and evolve on relatively short time scales, early-type stars have simple fields, usually dipoles with a magnetic axis misaligned with the rotational axis (Landstreet and Mathys, 2000), and they are very stable over long timescales, at least several decades (Briquet, 2015). The origin of these large-scale magnetic fields remains uncertain. Nevertheless some theories have been proposed. In Section 1.3 we will review the main theories, including numerical results from previous work, and then, describe our own approach to this question in Section 1.4.

In order to strengthen the context and the objectives of this thesis, we will provide an overview of astrophysical magnetic fields. Starting with the most well-known example, the Sun, followed by the chemically peculiar magnetic stars, i.e. Ap and Bp, and the contrast with their non-magnetic counterparts.

1.2 Magnetic fields

1.2.1 Solar magnetism

The most direct proof of an astronomical object with a large-scale magnetic field is our planet, the Earth, whose magnetic field has a maximum value in the surface of roughly 0.6 G (Choudhuri, 1998). However, although it is possible to study the geodynamo over geological times, it is an approximately static field over short timescales (decades). On the other hand we have the Sun, which works as the gateway to stellar magnetism, and due to its well-known magnetic cycle it is useful to improve and test our theories about astronomical magnetic fields.
The main observational evidence of the Sun's magnetic field are the sunspots, which have been registered from at least 800 BC. The first time it was discovered that they are associated with magnetic fields, was in the study of Hale (1908), who directly measured strong fields in the sunspots spectra using the Zeeman effect. Sunspots are regions with a very strong magnetic field. Due to this, the convective heat transport is inhibited, producing darker areas with lower temperature than

the rest of the photosphere. From the observation of the sunspots we can infer that the magnetic field of Sun is in fact quasi-cyclic.

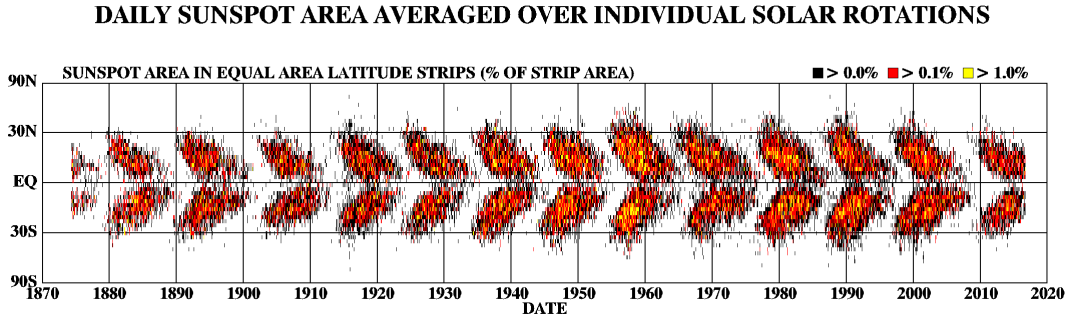

Figure 1.2.1: Solar butterfly diagram showing sunspots as a function of time and latitude (with EQ being the equator). Courtesy of Dr. David Hathaway and NASA.

In Figure 1.2.1 we show the position of sunspots on the Sun's surface from 1870 to 2020. It is possible to observe that sunspots appear at latitudes $\pm 40°$ and then they migrate towards the equator in roughly 11 years, subsequently repeating the cycle. Nevertheless, this cycle also includes changes in the polarity of the magnetic field, as we can see from Figure 1.2.2. Notice that after one cycle of 11 years, the large-scale magnetic field changes its polarity, so the solar magnetic cycle has in fact an average length of 22 years, while the sunspot cycle has a length of half of it. These magnetic cycles occur due to a dynamo operating in the convective zone of the Sun (see e.g. Charbonneau, 2020), above its radiative core. A detailed overview about the energy transportation mechanisms is given in Section 2.1.

1.2.2 Ap/Bp stars magnetism

As discussed in Chapter 1.1, a good example of magnetized early-type stars are Ap/Bp stars. Since the Zeeman effect observations by Babcock (1947), we know that they can host strong large-scale magnetic fields. The p comes from their chemical composition, because they show peculiar abundances of rare earths and some lighter elements such as silicon, as well as surface patterns of these elements, which are linked to the magnetic field. These may originate from gravitational settling and radiative levitation (Michaud, 1970). It is worth noting that there is a clear bimodality in this spectral type; Ap stars have magnetic fields that range

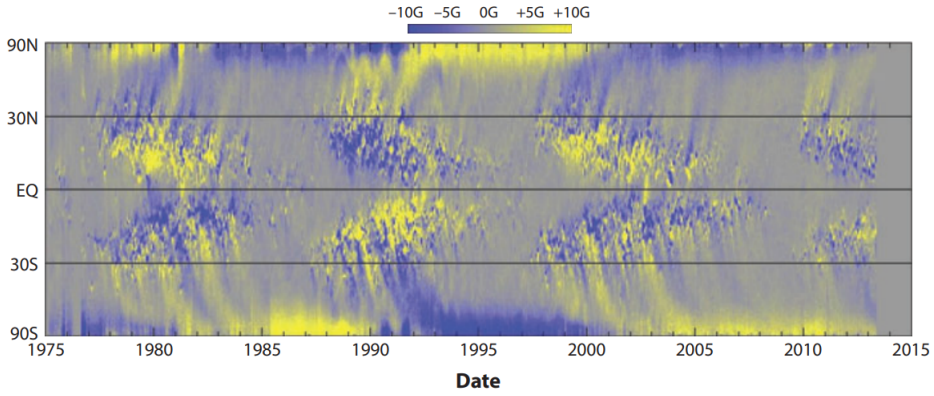

Figure 1.2.2: Time evolution of the averaged solar surface magnetic field (Butterfly diagram) from 1975 to 2015. Image adapted from Charbonneau (2014).

from 200 G to 34 kG, while their non-magnetized counterparts ("normal" A-type stars) usually have very weak fields below the detection limit. Nevertheless, weak magnetic fields have even been detected in the normal population, for example in Sirius and Vega. In the case of Vega, Zeeman polarimetry measured a magnetic field strength of 0.6 ± 0.3 G (Lignières et al., 2009; Petit et al., 2010, 2022), and 0.2 ± 0.1 G in Sirius (Petit et al., 2011). A-type stars are fast rotators (Royer et al., 2007), however, Ap stars rotate more slowly than their non-magnetic counterparts (Abt and Morrell, 1995). Indeed, Mathys (2008) have shown that non-magnetic A stars have rotation periods ranging from a few hours to a day, while most Ap stars have periods between one and ten days. The most extreme cases have periods of the order of 300 years, and some of them possibly around 1000 years (Mathys, 2015). This could be an indication of magnetic braking, however, there is no clear correlation between rotation and magnetic fields (Kochukhov and Bagnulo, 2006).

Interestingly, there seems to be a cutoff around 300 G in the Ap/Bp population. This is clearly visible in Figure 1.2.3, which corresponds to the dipole field strength (as mentioned, this is a good approximation for early-type stars) of a sample of 27 Ap/Bp stars, from Aurière et al. (2007). The dotted vertical line represents the cutoff at 300 G; below this value there are only 2 stars of the sample (HD 32650 and HD 96707), even though the sensitivity of the observations was much lower.

This also shows the previously mentioned bimodality of A-type stars. It is worth mentioning that a possible explanation of this could be fossil fields (see Section 1.3.2). In this context, the intensity of the magnetic field in the progenitor molecular cloud will determine if the star has a strong field during the main

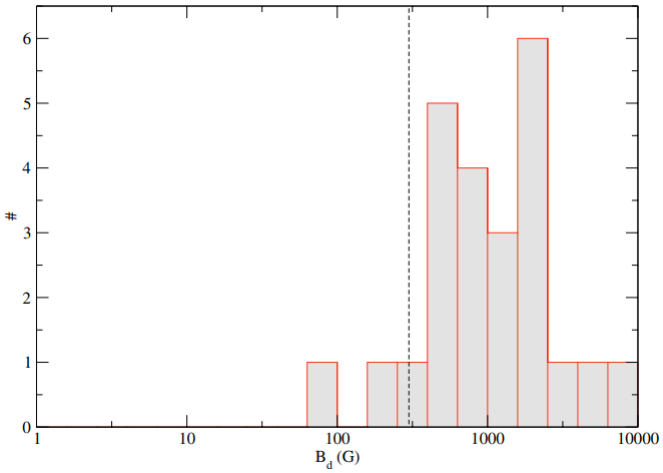

Figure 1.2.3: Histogram of best fit dipole field strengths, from the sample of 27 Ap/Bp stars described in Aurière et al. (2007).

sequence or not. However, it is unclear how or at which point specifically this magnetic seed is formed.

1.3 Possible explanations of magnetism in early-type stars

1.3.1 A dynamo driven in the convective core

Figure 1.1.1, shows that massive stars have a convective core. Indeed, it can be roughly 30% of the stellar radius in stars with masses higher than 5 $M_{\odot}$. This happens essentially because the main energy production mechanism in these stars is the CNO cycle, which is very temperature dependent. Therefore, the energy production is more concentrated in the center of the star, leading to a steep temperature gradient and a large energy flux, driving convection (for more information about the occurrence of convection, see Section 2.1.2.1). In A-type stars, it has been suspected that this convective core may host dynamo action (Krause and Oetken, 1976). Indeed, simulations by Browning et al. (2004) noted that these cores have differential rotation, and strong regions of shear that makes dynamo activity almost inevitable. This was reported by Brun et al. (2005), performing numerical simulations of the inner 30% by radius (where 15% is the core) of a 2 $M_{\odot}$ A-type star, obtaining magnetic fields with typical strengths

around the equipartition value with the kinetic energy. In B-type stars, magnetic activity has been found as well. Simulations by Augustson et al. (2016) of the core of a 10 $M_{\odot}$ B-type star, reported vigorous dynamo action, generating magnetic fields with peaks exceeding a megagauss in the fast rotators, and reaching super-equipartition values. However, although these studies show that a convective core can lead to strong dynamo action, the nature of these dynamos has not been explored in details. The relation between the magnetic cycle period of the core dynamo and the rotation of the core is unknown.

However, the natural question is if these magnetic fields can reach the surface of the star. In principle, this could happen under the action of buoyancy. Nevertheless, the timescale of this process has been estimated to be longer than the main-sequence life of these stars (Schuessler and Paehler, 1978; Parker, 1979; Moss, 1989), unless the magnetic structures are very small. This was reported by MacGregor and Cassinelli (2003), modelling a buoyant magnetic flux ring in the radiative interior of an early-type star (with $M < 10\ M_{\odot}$), finding reasonable transport times from the core to the surface of the star (less than the star main-sequence life). Nonetheless, MacDonald and Mullan (2004) re-examined the conclusions of MacGregor and Cassinelli (2003), but adding more realistic parameters (based on detailed evolutionary models), like differential rotation, and realistic strong compositional gradients in the radiative layers. This slows down the buoyancy process considerably, and magnetic fields higher than the equipartition values are required to make this process feasible. One mechanism that could counter this situation, is convective overshooting. This could allow mixing in the stably stratified zone above the convective core, reducing the compositional gradient. Also, the field that penetrates the radiative envelope might be strengthened by the shearing produced by the differential rotation, making it strong enough to reach the surface via buoyancy.

It is worth mentioning that stellar models have predicted thin convective layers close to surface of early-type stars (Richard et al., 2001; Cantiello et al., 2009). This happens due to bumps in the stellar opacities, i.e. the so-called Iron-peak (Iglesias et al., 1992), and often another peak related to Helium ionization. These layers could host dynamo action very close to the stellar surface. Cantiello and Braithwaite (2011) reported that the resulting magnetic field can easily rise buoyantly to the surface due to the low density in the radiative layer, giving

a very short thermal timescale. However, the surface fields are expected to be smaller than a few hundred Gauss, which makes it unlikely that these layers are responsible for the large scale magnetic fields of these stars.

1.3.2 Fossil fields

Magnetic fields of late-type stars coming from dynamo processes evolve on relatively short timescales, while the large-scale fields in early-type stars seem to be very stable over long timescales (see Section 1.2.2 for more observed properties). Also, as we discussed, all these stars seem to have stably stratified envelopes. These observations suggest that the origin of these magnetic fields are indeed *fossil fields*, i.e. magnetic configurations that were originated at some early evolutionary phase of the star. The idea behind this, is that forces that contribute to the momentum equation (2.2.7) may eventually reach an equilibrium, including the Lorentz force and therefore one may expect a magnetic field in the star, and no flow velocity $u \sim 0$. This would transform the induction equation, i.e. the equation that describe the evolution of the magnetic field, into a diffusion equation (see Section 2.2.1 for more information). Therefore, the magnetic field will evolve on a diffusive timescale, the Ohmic diffusion time $t_{\rm diff} = R^2/\eta$, where $\eta = (\mu_0\sigma)^{-1}$ is the magnetic diffusivity (or resistivity), a quantity inversely proportional to the electric conductivity σ of the star, and μ_0 is the vacuum magnetic permeability.

Cowling (1945) realized that in the radiative core of the Sun, this timescale is of the order of 10^{10} years, and therefore, a field in equilibrium inside this zone could last for the whole main-sequence lifetime of the star. However, the problem is to find stable configurations. Analytical techniques have had limited success in order to convincingly demonstrate the existence of these stable equilibria, and some methods seem to indicate possible instabilities rather than demonstrating stability. For example, the energy method of Bernstein et al. (1958) showed that purely poloidal and purely toroidal fields in highly ideal conditions are unstable under perturbations (Tayler, 1973; Markey and Tayler, 1973, 1974; Wright, 1973).

Numerical MHD simulations by Braithwaite and Nordlund (2006), produced stable configurations in the radiative interior of a 2 $M_\odot$ A-type star starting from an initially random field, which relaxed to a stable roughly axisymmetric torus inside the star, with poloidal and toroidal components of comparable strength. This solution leads to a roughly dipolar surface field. Non-axisymmetric configurations

consisting of twisted flux tubes lying horizontally below the surface of the star were found by Braithwaite (2008), starting from turbulent initial conditions. Mitchell et al. (2015) performed simulations of a barotropic (isentropic) star, testing random disordered magnetic fields, and mixed toroidal-poloidal axisymmetric fields. None of these configurations were stable in this type of star, indicating that stable stratification is an essential ingredient for the stability of magnetic fields. Becerra et al. (2022) modelled a stably stratified and barotropic stars, confirming previous results. No stable configurations were found for the barotropic model, while initially random fields evolved to stable equilibrium in the radiative model. However, the final state of the equilibrium depends directly on the chosen dissipation mechanisms.

It is worth mentioning that this idea is not mutually exclusive with the dynamo driven by the convective core of the star. In fact, a fossil field in the radiative envelope might affect the nature of the core dynamo (see Boyer and Levy 1984, in the context of the Sun). Featherstone et al. (2009) performed MHD simulations of the inner 30% by radius of a 2 $M_\odot$ A-type star, and they found an equipartition dynamo-originated field in the core. However, the inclusion of a twisted toroidal fossil field can lead to a super-equipartition state in the core dynamo, where the magnetic energy is roughly 10 times stronger than the kinetic energy of convection.

1.3.3 Dynamo in the radiative zone

As discussed in Section 1.1, dynamo action typically requires convection and rotation. These are the required ingredients for a stellar convective dynamo. In this context, the field lines from an initially poloidal magnetic field get stretched by differential rotation producing a toroidal magnetic field (Ω effect). Furthermore, a new poloidal magnetic field can be created by twisting the field lines from the existing toroidal field, closing the dynamo loop. As initially proposed by Parker (1955), this can be done via helical fluid motions, typical of rotating convection in the solar convection zone. After the work by Steenbeck et al. (1966) with mean-field dynamo theory, this process is commonly known as the α effect.

However, this is one of the possibilities, but in principle, convection is not really necessary. A magnetic instability in the toroidal magnetic field can generate a poloidal field, replacing the role of convection and closing the dynamo loop. Such an instability is the Tayler instability (Tayler, 1973) which can also take place in

the stably stratified zones inside a star. This instability combined with differential rotation is the Tayler-Spruit dynamo scenario, proposed by Spruit (2002).

It is worth mentioning that recently Petitdemange et al. (2023a,b) modelled the dynamics of a stably stratified, differentially rotating, magnetized fluid in a spherical shell. Reporting the first numerical simulations of the Tayler-Spruit dynamo, verifying theoretical assumptions made by Spruit (2002).

1.4 This project

The objective of this project is to perform 3D magnetohydrodynamic simulations using the star-in-a-box model, adapted from Käpylä (2021, 2022), as a way to understand the origin of the large-scale magnetic fields in A-type stars.

In order to do this, we explore two scenarios:

- **Protostellar phase:** In the first part, we perform numerical simulations of a fully convective 2 $M_\odot$ star, which is believed to be representative of the pre-main-sequence evolution of chemically peculiar Ap subclass as they descend their Hayashi tracks (Hayashi et al., 1962; Siess et al., 2000). In principle, using realistic resistivities only a small fraction of the generated magnetic flux is able to survive turbulent decay during this phase (Moss, 2003; Schleicher et al., 2023). However, if the magnetic field is strong enough this small fraction could be enough to be a representative fossil field once the star reaches the main sequence, i.e. the magnetic field configurations produced by these models could be potential inputs to look for stable configurations in a main-sequence stellar model. These fully convective simulations explore rotation periods from 20 to 280 days, which gives a range of Coriolis numbers from 1 to ~ 30 (see Section 2.2.3). The dynamo solutions, as well as the analysis of the large-scale flows, energies, and differential rotation, are described in Chapter 4.

- **Main-sequence phase:** The second part consists of numerical simulations of the main-sequence phase of a 2 $M_\odot$ star. This model has a convective core of roughly 20% of the stellar radial extent surrounded by a stably stratified envelope. These simulations allow us to explore dynamos generated by convection in the core of the star, not only in the interior of it but also in the

stellar surface. Additionally, like the models of Browning et al. (2004), Brun et al. (2005) and Featherstone et al. (2009), we develop a "zoom" model which encompasses the convective core and a part of the radiative zone. This is convenient to explore the core with more resolution, however, the surface of the star is outside the domain of the simulation. Data from this setup will be used to characterize the relation between rotation period and magnetic activity period of the core dynamo for the first time. This relation and an analysis similar to the protostellar model is presented in Chapter 5, with the addition that this analysis was done at $r = R$ and at $r = 0.2R$, where R is the stellar radius. Rotation periods from 8 to 20 days are explored.

The models mentioned above are described more extensively in Section 3.3.1. In both, the compressible non-ideal magneto-hydrodynamics equations are solved using the Pencil Code (Pencil Code Collaboration et al., 2021).

Chapter 2

Stellar structure and magnetohydrodynamics

As discussed in Section 1, stars have a very wide range of magnetic fields, depending on their internal structure and possibly also on pre-main-sequence mechanisms (like in the fossil field theory). However, there are some key elements that are required in order to have a dynamo, or to study if an existing magnetic field can survive in a stable configuration. In this chapter, a brief description of stellar physics will be given, including the energy transport mechanisms, and how to establish the stability against convection in a specific layer. Furthermore, non-ideal magnetohydrodynamics is also discussed, as well as its equations, and useful dimensionless parameters to characterize the system.

2.1 Energy transport mechanisms

The energy that a star radiates away from its surface comes from its central region. The energy transport between the core and the surface is possible because the star has a non-zero temperature gradient. This is a key factor in both transport mechanisms that will be reviewed in this section, radiation and convection. The local physical situation inside the star will determine which one occurs. A general overview will be given, and then a criteria that determines if a layer is stable or not against convection.

2.1.1 Radiation

Inside a star, photons that carry the energy from the core are constantly scattered, absorbed, and re-emitted in random directions by particles such as electrons. This is because stellar matter is very opaque, and therefore, photons have a very short mean free path of $l_{\rm ph} \sim 2$ cm $\ll R_\odot$ (Kippenhahn et al., 2013). The radiation field inside a star is extremely close to a black-body radiation. However, it is still possible to find a small anisotropy due to tiny temperature differences, e.g. for the Sun the temperature variation over a distance $l_{\rm ph}$ is $\Delta T \sim 10^{-4}$ K. This gives a temperature difference of $\Delta T/T \sim 10^{-11}$, quite small but enough to carry the whole energy flux of the Sun (Pols, 2011).

These considerations allow us to simplify the physical description of radiation as a diffusion process, obtaining:

$$\boldsymbol{F}_{\rm rad} = -K_{\rm rad}\boldsymbol{\nabla} T, \tag{2.1.1}$$

for the radiative energy flux, where $K_{\rm rad}$ is known as radiative heat conductivity (for a detailed formulation, see e.g. Weiss et al., 2004). It works as a coefficient of conduction for the radiative (diffusive) transfer, formally defined as:

$$K_{\rm rad} = \frac{1}{3}\overline{v} l_{\rm ph} c_{\rm V}. \tag{2.1.2}$$

For photons, we have the mean velocity as the speed of light $\overline{v} = c$, the mean free path is given by $l_{\rm ph} \sim 1/\kappa\rho$, where κ is the opacity, ρ is the density, and $c_{\rm V}$ is the heat capacity at constant volume:

$$c_{\rm V} = \frac{dU}{dT} = \frac{d}{dT}\left[\frac{1}{c}\int_0^\infty I(\nu, T)d\nu \int d\Omega\right] = \frac{d}{dT}\left[\frac{4}{c}\left(\frac{2\pi^5 k_B^4}{15c^2h^3}\right)T^4\right] = 4aT^3,$$

where $I(\nu, T)$ is the intensity of a radiation beam at a frequency ν and temperature T, and $a \equiv \frac{4}{c}\left(\frac{2\pi^5 k_B^4}{15c^2h^3}\right)$ is the radiation density constant. Therefore, replacing this in equation (2.1.2), we obtain:

$$K_{\rm rad} = \frac{4}{3}\frac{acT^3}{\kappa\rho}. \tag{2.1.3}$$

Then, expressing the energy flux in terms of the local luminosity $L_r = 4\pi r^2 F_{\rm rad}(r)$,

and also considering spherical symmetry, i.e. $\boldsymbol{\nabla} T = (\partial T/\partial r)\hat{\boldsymbol{r}}$, we obtain:

$$\left.\frac{\partial T}{\partial r}\right|_{\text{rad}} = -\frac{3}{16\pi ac}\frac{\kappa\rho L_r}{r^2 T^3}. \tag{2.1.4}$$

Using this expression and $dm = 4\pi\rho r^2 dr$, where m is the mass coordinate, we can define the radiative temperature gradient:

$$\nabla_{\text{rad}} = \left(\frac{d\ln T}{d\ln P}\right)_{\text{rad}} = \frac{3}{16\pi acG}\frac{\kappa L_r P}{mT^4}, \tag{2.1.5}$$

a dimensionless parameter that will be very useful to establish a criterion that determines when the star (or a certain zone of it) is in radiative equilibrium, i.e., stable against convection.

Finally, notice that this is valid as long as $l_{\text{ph}} \ll R$. If the medium is optically thin, then the diffusion approximation is not valid anymore and we will have to solve the complete radiative transfer equations. This, for example, is required in the photosphere where photons escape, and therefore $l_{\text{ph}} \geq R$.

2.1.2 Convection

The temperature gradient required to carry a luminosity L_r by the radiation, is given by equation (2.1.4). The larger the luminosity that has to be carried, the larger the temperature gradient required. However, the temperature gradient has an upper limit given by the adiabatic temperature gradient (see Section 2.1.2.1), and if this value is exceeded then the region will become dynamically unstable, producing cyclic macroscopic motions known as convection.

Inside convection zones, we clearly expect to have a lot of movement in the fluid, and therefore a non-zero flow velocity. In section 2.2.1, we describe the equation that describes the temporal evolution of the magnetic field in magnetohydrodynamics, noticing that one of the key ingredients in order to have a growing magnetic field, is a non-zero flow velocity, this is why these amplification processes are most likely to occur where convection happens (see Brandenburg and Subramanian, 2005).

2.1.2.1 Convective stability

As a first approximation, it is possible to estimate where convection happens in simulations by checking some of variables, like flow velocity or entropy. Convection zones are expected to be nearly isentropic (nearly constant), while on the other hand, radiative zones are expected to have entropy gradients. However, there is an analytic way to check this stability with some gradients previously defined, and also considering the chemical composition of the star.

A layer inside a star will be stable against convection if the Ledoux criterion is fulfilled, this is:

$$\nabla_{\rm rad} < \nabla_{\rm ad} - \frac{\chi_\mu}{\chi_T}\nabla_\mu, \tag{2.1.6}$$

where $\nabla_{\rm rad}$ is the radiative temperature gradient (2.1.5), and $\nabla_{\rm ad}$ is the adiabatic temperature gradient:

$$\nabla_{\rm ad} = \left(\frac{d\ln T}{d\ln p}\right)_{\rm ad}. \tag{2.1.7}$$

Note that adiabatic here implies changes in T with respect to p at constant entropy s, and therefore no heat Q is added or extracted in the system ($dQ = 0$). Furthermore, ∇_μ is the mean molecular weight gradient, defined as:

$$\nabla_\mu = \frac{d\ln\mu}{d\ln P}. \tag{2.1.8}$$

Also:

$$\chi_T = \left(\frac{\partial\ln P}{\partial\ln T}\right)_{\rho,X_i} = \frac{T}{P}\left(\frac{\partial P}{\partial T}\right)_{\rho,X_i}, \quad \chi_\mu = \left(\frac{\partial\ln P}{\partial\ln\mu}\right)_{\rho,T} = \frac{\mu}{P}\left(\frac{\partial P}{\partial\mu}\right)_{\rho,T},$$

where X_i means that the composition is held constant. If the layer is chemically homogeneous, we have $\nabla_\mu = 0$, and therefore, the Ledoux criterion is reduced to:

$$\nabla_{\rm rad} < \nabla_{\rm ad}, \tag{2.1.9}$$

which is known as Schwarzschild criterion. From this expression, and also (2.1.5), we can infer that a large value of κ or regions with a large energy flux (L_r/m) can drive convection. Finally, we can write down an equivalent expression to (2.1.9)

in terms of the radial temperature gradients:

$$\left(\frac{\partial T}{\partial r}\right)_{\text{rad}} > \left(\frac{\partial T}{\partial r}\right)_{\text{ad}}, \tag{2.1.10}$$

where $\frac{\partial T}{\partial r}|_{\text{rad}}$ is given by (2.1.4). As both gradients are negative it is common to express (2.1.10) with absolute values, obtaining:

$$\left|\frac{\partial T}{\partial r}\right|_{\text{rad}} < \left|\frac{\partial T}{\partial r}\right|_{\text{ad}}. \tag{2.1.11}$$

From here, we notice that the layer will be stable against convection as long as the radiative temperature gradient is shallower than the adiabatic temperature gradient.

2.1.2.2 Mixing length theory

Despite the importance of convection in stellar structure, a formal and rigorous mathematical description of it has not been developed yet, and it is a poorly understood process in stellar physics. However, as a basic approach to formulate an analytic theory to treat convection, we have the mixing length theory. Initially formulated independently by Taylor (1915), Schmidt (1917) and Prandtl (1925), and later applied in the stellar context by Biermann (1932), Vitense (1953) and Böhm-Vitense (1958), its basic idea is that the fluid movements inside convection zones can be approximated as *blobs* in pressure equilibrium with its surroundings, moving up (or down) in a straight line before dissolving into a new environment. The *blobs* are not in thermal equilibrium with the environment, so a relatively hot *blob* will move a distance l_{m} (known as the mixing length) to the colder environment, where it will merge adding energy to it. On the other hand, cooler *blobs* will move towards hotter regions, dissolving itself and reducing the energy of the new environment. This happens because hot *blobs* are less dense than the surrounding, and therefore buoyancy forces cause them to rise and expand, while cooler *blobs* shrink and compress.

Using this formulation, we can obtain an expression for the convective energy flux, analogous to equation (2.1.1) for the radiative case, given by (Kippenhahn et al.,

2013; Schleicher and Mennickent, 2017):

$$F_{\text{conv}} = \rho c_{\text{P}} T \left(\frac{l_m}{H_p}\right)^2 \sqrt{\frac{1}{2} g H_p} (\nabla - \nabla_{\text{ad}})^{3/2}, \tag{2.1.12}$$

where c_{P} is the heat capacity at constant pressure, g is the gravitational acceleration, H_p is the local pressure scale height, where a common assumption is $l_m \sim H_p$ (Pols, 2011), ∇_{ad} is the adiabatic temperature gradient (2.1.7), and:

$$\nabla = \frac{d \ln T}{d \ln p} \tag{2.1.13}$$

is the actual temperature gradient.

For a complete review of mixing length theory see Gough (1977) and Joyce and Tayar (2023).

2.2 Magnetohydrodynamics

Magnetohydrodynamics (MHD), also known as magneto-fluid dynamics, is a branch of physics dedicated to the study of the magnetic properties in plasma, treated as an electrically conducting and magnetized fluid. In this context, the one-fluid model is used, therefore, the formalism is valid only when charge separation is negligible, i.e. when electrons and ions do not respond very differently (Choudhuri, 1998). The full description of the set of MHD equations depends on the characteristics of the astrophysical system (viscosity, compressible or incompressible flows, resistivity, etc), but basically, it consists in a combination of Maxwell's equations of electromagnetism and the hydrodynamics equations (see Section 2.2.2 for a overview of the non-ideal MHD equations).

2.2.1 The induction equation

The microscopic interpretation of Ohm's law establishes that currents inside a material are proportional to the electric field, this is $\boldsymbol{J} = \sigma \boldsymbol{E}$, where the constant of proportionality σ is known as the conductivity of the material. However, this is a stationary situation. If we consider a moving charge with velocity $\boldsymbol{u}$, and a co-moving frame of reference K', then the Ohm's law in this frame can be written as $\boldsymbol{J} = \sigma \boldsymbol{E}'$. We also can express $\boldsymbol{E}'$ in terms of the electric field in a fixed frame

($\boldsymbol{E}$), obtaining:

$$\boldsymbol{J} = \sigma(\boldsymbol{E} + \boldsymbol{u} \times \boldsymbol{B}). \tag{2.2.1}$$

Now, the Ampère-Maxwell law is given by:

$$\boldsymbol{\nabla} \times \boldsymbol{B} = \mu_0 \boldsymbol{J} + \frac{1}{c} \frac{\partial \boldsymbol{E}}{\partial t}. \tag{2.2.2}$$

In the classic MHD model it is assumed that fluid flows are non-relativistic ($u \ll c$), and from equation (2.2.1) it is easy to prove that $E \sim u/c\, B$ (see e.g. Schekochihin, 2021), and therefore the displacement current can be neglected:

$$\frac{\left|\frac{1}{c}\frac{\partial \boldsymbol{E}}{\partial t}\right|}{|\boldsymbol{\nabla} \times \boldsymbol{B}|} \sim \frac{\frac{1}{c}\frac{E}{t}}{\frac{B}{l}} \sim \frac{u^2}{c^2} \ll 1.$$

Thus, equation (2.2.2) reduces to the original pre-Maxwell form of the Ampère's law:

$$\boldsymbol{\nabla} \times \boldsymbol{B} = \mu_0 \boldsymbol{J}. \tag{2.2.3}$$

Now, inserting (2.2.3) into (2.2.1) and solving for $\boldsymbol{E}$, we find:

$$\boldsymbol{E} = \frac{\boldsymbol{\nabla} \times \boldsymbol{B}}{\mu_0 \sigma} - \boldsymbol{u} \times \boldsymbol{B}.$$

Finally, replacing this expression into Faraday's law $\boldsymbol{\nabla} \times \boldsymbol{E} = -\partial_t \boldsymbol{B}$, and also defining $\eta = (\mu_0 \sigma)^{-1}$ as the magnetic diffusivity, we obtain:

$$\frac{\partial \boldsymbol{B}}{\partial t} = \boldsymbol{\nabla} \times (\boldsymbol{u} \times \boldsymbol{B} - \eta \boldsymbol{\nabla} \times \boldsymbol{B}), \tag{2.2.4}$$

which is known as the induction equation.

Notice that if η is constant, using the relation $\boldsymbol{\nabla} \times (\boldsymbol{\nabla} \times \boldsymbol{B}) = \boldsymbol{\nabla}(\boldsymbol{\nabla} \cdot \boldsymbol{B}) - \nabla^2 \boldsymbol{B}$, and the solenoidal constrain of the magnetic field ($\boldsymbol{\nabla} \cdot \boldsymbol{B} = 0$), we can reduce the expression (2.2.4) into:

$$\frac{\partial \boldsymbol{B}}{\partial t} = \boldsymbol{\nabla} \times (\boldsymbol{u} \times \boldsymbol{B}) + \eta \nabla^2 \boldsymbol{B} \tag{2.2.5}$$

and this expression is useful, because if the solenoidal condition was satisfied initially, then any solution of (2.2.5) will have the solenoidal constraint too, i.e. be divergence-free. Another way of keeping this constraint, is to write the induction equation in terms of the magnetic vector potential $\boldsymbol{B} = \boldsymbol{\nabla} \times \boldsymbol{A}$, and therefore

$\boldsymbol{\nabla} \cdot (\boldsymbol{\nabla} \times \boldsymbol{A}) = 0.$

Notice that the first term of (2.2.5) is an advection term that quantifies the evolution of the magnetic field by the flow of a fluid, and the second one is a diffusive term, which quantifies the diffusion of the magnetic field.

If we have $\eta = 0$, then the fluid will become a perfect conductor ($\sigma \to \infty$), and we will obtain the ideal MHD case. In this regime any fluid element that lies on a magnetic field line in a certain time t will remain on that field line for every other time, so the fluid will drag the field lines, or in other words, the field lines are "frozen" into the fluid. This has an implication: if the fluid tries to compress or bend the field lines, the field will resist as if it possesses a restoring force. This property gives elasticity to MHD fluids and is known as Alfvén's theorem (Davidson, 2002).

Also, notice that if we have a fluid at rest ($u = 0$), then we can neglect the advection term, and equation (2.2.5) reduces to:

$$\frac{\partial \boldsymbol{B}}{\partial t} = \eta \nabla^2 \boldsymbol{B},$$

which is a diffusion equation. This is a direct proof that magnetic field decays in the absence of motions, i.e., every fluid requires $u \neq 0$ to amplify a magnetic field.

2.2.2 Full set of non-ideal MHD equations

The non-ideal MHD equations that will be reviewed in this thesis provide a description of the fluid evolution (including diffusivities) with compressible flows ($\boldsymbol{\nabla} \cdot \boldsymbol{u} \neq 0$), and the evolution of magnetic fields. First, we have the continuity equation, that describes the conservation of mass, given by:

$$\frac{D \ln \rho}{Dt} = -\boldsymbol{\nabla} \cdot \boldsymbol{u}, \tag{2.2.6}$$

where $D/Dt = \partial/\partial t + \boldsymbol{u} \cdot \boldsymbol{\nabla}$ is the advective (or material) derivative, ρ is the density of the fluid, and $\boldsymbol{u}$ is the flow velocity. Considering a non-inertial co-rotating frame of reference with angular velocity $\boldsymbol{\Omega}$, the Navier-Stokes equation

(which describes the conservation of momentum) is given by:

$$\frac{D\boldsymbol{u}}{Dt} = -\frac{1}{\rho}\boldsymbol{\nabla} p - \boldsymbol{g} + \boldsymbol{F}_{\text{visc}} + \boldsymbol{F}_{\text{cor}} + \boldsymbol{F}_{\text{cent}} + \boldsymbol{F}_{\text{Lor}} + \boldsymbol{F}, \tag{2.2.7}$$

where p is the pressure, and $\boldsymbol{g}$ is the gravitational acceleration, which is usually written in terms of the Newtonian gravitational potential $\boldsymbol{g} = -\boldsymbol{\nabla}\Phi$ that fulfills the Poisson equation:

$$\nabla^2\Phi = 4\pi G\rho, \tag{2.2.8}$$

where G is the gravitational constant. The additional forces acting on the fluid are viscosity, fictional forces related to the non-inertial frame of reference i.e. Coriolis and centrifugal force, the Lorentz force, and $\boldsymbol{F}$ denotes any other external force per unit acting on the fluid. Therefore:

$$\begin{aligned}
\boldsymbol{F}_{\text{visc}} &= \frac{1}{\rho}\boldsymbol{\nabla}\cdot\left[2\mu\boldsymbol{S} + \xi(\boldsymbol{\nabla}\cdot\boldsymbol{u})\boldsymbol{I}\right], \\
\boldsymbol{F}_{\text{cor}} &= -2\boldsymbol{\Omega}\times\boldsymbol{u}, \\
\boldsymbol{F}_{\text{cent}} &= -\boldsymbol{\Omega}\times(\boldsymbol{\Omega}\times\boldsymbol{x}), \\
\boldsymbol{F}_{\text{Lor}} &= \frac{1}{\rho}\boldsymbol{J}\times\boldsymbol{B},
\end{aligned}$$

where $\mu = \nu\rho$ is the dynamical viscosity, $\boldsymbol{I} = \delta_{ij}$ is the identity matrix defined as the Kronecker delta, ξ is the bulk (or second) viscosity, which describes the irreversible resistance, over and above the reversible resistance to changes of volume (Hoover et al., 1980). At least in the context of this thesis, we will assume the Stokes' hypothesis ($\xi = 0$), and thus, this parameter will be neglected. Usually high values of $\boldsymbol{\nabla}\cdot\boldsymbol{u}$ make this assumption wrong, e.g. inside a shock wave (Sharma and Kumar, 2019), but otherwise, this approximation is usually valid. Also, it has been proven that for monatomic gases, ξ can be totally neglected (see Buresti, 2015). $\boldsymbol{S}$ is the trace-less rate-of-strain rank-2 tensor, defined as:

$$S_{ij} = \frac{1}{2}(\partial_j u_i + \partial_i u_j) - \frac{1}{3}\delta_{ij}\partial_k u_k. \tag{2.2.9}$$

Note that the viscous term can as well be written in terms of the viscous stress tensor, where $\tau_{ij} = 2\mu_0 S_{ij}$, and also, some sources combine that term with pressure, expressing both in terms of the Cauchy stress tensor, following $\boldsymbol{\nabla}\cdot\boldsymbol{\sigma} = \boldsymbol{\nabla}\cdot\boldsymbol{\tau} - \boldsymbol{\nabla} p$. In the *rotational forces*, the rotation rate is denoted by $\boldsymbol{\Omega}$, and $\boldsymbol{x}$ is the distance

from the axis of rotation. Finally, $\boldsymbol{J}$ is the current density, given by Ampère's law (2.2.3).

The energy equation is usually expressed in terms of the entropy per mass unit s, and it is given by:

$$\rho T \frac{Ds}{DT} = -\boldsymbol{\nabla} \cdot \boldsymbol{\mathcal{F}}_{\rm rad} + 2\mu_0 \boldsymbol{S}^2 + \xi(\boldsymbol{\nabla} \cdot \boldsymbol{u})^2 + \eta\mu_0 \boldsymbol{J}^2 + \mathcal{H} - \mathcal{C}, \tag{2.2.10}$$

where T is the temperature, μ_0 is the vacuum magnetic permeability, and $\boldsymbol{\mathcal{F}}_{\rm rad}$ represents the radiative energy flux. In principle, the radiative energy transfer equations could be solved here, however, as we already discussed in Section 2.1.1, small temperature variations and $l_{\rm ph} \ll R_*$ allow us to approximate the radiative energy transport as a diffusion process, obtaining:

$$\boldsymbol{\mathcal{F}}_{\rm rad} = -K_{\rm rad} \boldsymbol{\nabla} T. \tag{2.2.11}$$

In principle $K_{\rm rad}$ can be described with equation (2.1.3), but the opacity κ is not an easy quantity to determine, because it tends to be a complicated function of the density, chemical composition, and temperature. This is why, in numerical simulations it is convenient to define an specific profile for $K_{\rm rad}$, e.g. constant, vertical or radial, or based on Kramers opacity law:

$$K_{\rm rad}(\rho, T) = K_0 \left(\frac{\rho}{\rho_0}\right)^{a-1} \left(\frac{T}{T_0}\right)^{b+3}. \tag{2.2.12}$$

When most of the opacity comes from free-free and bound-free transitions, we have $a = -1$ and $b = 7/2$ (Brandenburg et al., 2000; Weiss et al., 2004; Käpylä, 2021). The last terms, $\mathcal{H}$ and $\mathcal{C}$ represent explicit heating and cooling (respectively) of the system due to other sources or sinks of energy.

Finally, we need to add an equation for the evolution of the magnetic field, i.e. the induction equation (2.2.5), which will be written again in its most common formulation for completeness (with constant η):

$$\frac{\partial \boldsymbol{B}}{\partial t} = \boldsymbol{\nabla} \times (\boldsymbol{u} \times \boldsymbol{B}) + \eta \nabla^2 \boldsymbol{B}.$$

Also, note that the solenoidal constrain $\boldsymbol{\nabla} \cdot \boldsymbol{B} = 0$ must be fulfilled the whole time, so in principle (if it is not imposed to the induction equation as we discussed

in section 2.2.1) it is part of the equations that must be solved as well.

To fully characterize the fluid, it is necessary to add an equation of state which relates the thermodynamic variables. This is not easy to formulate, but in the most simple cases, we can relate p and ρ using a polytropic equation of state (Bartelmann, 2021):

$$p = K\rho^{\gamma}, \tag{2.2.13}$$

where K is a constant of proportionality, $\gamma = \frac{1}{n} + 1$ is the adiabatic index, and n is the polytropic index.

The ideal gas law can also be used as an idealized and simple scenario:

$$p = (\gamma - 1)\rho e = \mathcal{R}\rho T, \tag{2.2.14}$$

where $e = c_{\mathrm{V}}T$ is the internal energy of the gas, c_{V} is the heat capacity at constant volume, and $\mathcal{R}$ is the ideal gas constant.

2.2.3 Dimensionless numbers

To characterize an astrophysical system it is very useful to define dimensionless parameters that are ratios of terms that describe different processes in an equation. Related to fluids and plasmas, we can define:

- The Reynolds number (Re), is the ratio between inertial and viscous forces. It is formally defined as:

  $$\mathrm{Re} = \frac{uL}{\nu}$$

  where u is the typical velocity of the fluid, L is the typical length scale of the system, and ν the kinematic viscosity. This number determines if the flow is laminar (low values of Re) or turbulent (high values of Re) (Choudhuri, 1998).

- The Coriolis number (Co), is the inverse of the Rossby number (Rossby, 1939) and it is the ratio between the Coriolis force and the acceleration of the fluid, formally defined as:

  $$\mathrm{Co} = \frac{Lf}{u}$$

  where $f = 2\Omega$ is the Coriolis frequency, given by the angular speed Ω.

- The magnetic Reynolds number ($\mathrm{Re_M}$), is the ratio between the advection term and the diffusion term in the induction equation, formally defined as:

$$\mathrm{Re_M} = \frac{|\boldsymbol{\nabla} \times (\boldsymbol{u} \times \boldsymbol{B})|}{|\eta \nabla^2 \boldsymbol{B}|} \sim \frac{uL}{\eta}.$$

  This means that if $\mathrm{Re_M} \gg 1$ then the evolution of the magnetic field on the fluid will be due to flow. Otherwise, if $\mathrm{Re_M} \ll 1$ then the evolution will be mainly due to diffusion and the energy will be lost via Ohmic dissipation.

- The Prandtl number (Pr), is the ratio between the kinematic viscosity ν (also known as momentum diffusivity) and the thermal diffusivity χ:

$$\mathrm{Pr} = \frac{\nu}{\chi},$$

  Therefore, it gives the relation between the momentum transport and the thermal transport capacity of a fluid. In other words, if $\mathrm{Pr} \ll 1$ then the heat transfer is most likely to occur by fluid conduction rather than by fluid momentum. Notice that this number is not related to the flows, so it can be understood as an intrinsic property of the plasma.

- The magnetic Prandtl number ($\mathrm{Pr_M}$), is the ratio of the magnetic Reynolds number and the Reynolds number:

$$\mathrm{Pr_M} = \frac{\mathrm{Re_M}}{\mathrm{Re}} = \frac{\nu}{\eta}$$

  so it can also be defined as a ratio between the kinematic viscosity ν and the magnetic diffusivity η. It is also an intrinsic property of the plasma.

Chapter 3

Numerical models and methods

In this chapter, we describe the numerical models used in this project, starting from the MESA code, which was used to obtain the stellar parameters of the star, and the Pencil Code, which was used to produce the MHD simulations. A brief description of the output files, the setups, the simulation strategy, the physical units and diagnostic quantities are given.

3.1 MESA code

Modules for Experiments in Stellar Astrophysics (Paxton et al., 2011, 2013, 2015, 2018, 2019)[1] is an open source one-dimensional stellar evolution code, that allows to model a wide range of stars, ranging from very low mass to massive stars, and advanced evolutionary phases. It provides adaptive mesh refinement, sophisticated timestep control, and OpenMP-based shared memory parallelism.

3.1.1 Online version

Here, we use the online version MESA-Web[2] created by Rich Townsend, which is a re-implementation of a previous version hosted in the Arizona State University created by Carl Fields and Frank Timmes, based on the original MESA code.

[1] https://docs.mesastar.org/en/release-r22.11.1/
[2] http://user.astro.wisc.edu/~townsend/static.php?ref=mesa-web

3.1.2 Input parameters

The input parameters of the model must be introduced in the calculation submission page. The input are divided as follows:

- Initial properties, where we have to specify the initial mass of the star in solar masses. Metallicity expressed as the mass fraction of metals, and the rotation rate of the star, in terms of $\Omega_{\rm ZAMS}/\Omega_{\rm crit}$, which corresponds to ratio between the angular velocity of the star in the zero-age main sequence (ZAMS), and the critical angular velocity, given by $\Omega_{\rm crit} = \sqrt{GM/R^3}$.
- Nuclear reactions, where the chemical reactions inside the core of the star are defined (e.g. General H/He burning, H/He/C/O burning, evolved massive stars, etc).
- Mixing, which contain parameters of stellar convection based on the mixing length formulation, including overshooting and thermohaline.
- Stellar winds.
- Numerical resolution, where we can define the mass and time resolution for the global simulation.
- General. Here, we can define the frequency of the output files, and the version of MESA that will be used.

3.1.3 A-type star model

In order to model a main-sequence A-type star, we used a stellar mass of 2 $M_\odot$, and a metallicity of 0.02. For the rotation rate we tried a non-rotating model ($\Omega_{\rm ZAMS}/\Omega_{\rm crit} = 0$), and two rotating models with $\Omega_{\rm ZAMS}/\Omega_{\rm crit} = 0.05$ and $\Omega_{\rm ZAMS}/\Omega_{\rm crit} = 0.5$. Nuclear reactions contain the isotopes ^{1}H, ^{3}He, ^{4}He, ^{12}C, ^{14}N, ^{16}O, ^{20}Ne, ^{24}Mg for general H/He burning. For convection we assumed $\alpha_{\rm MLT} = 2$, which defines the mixing length as $l_m = \alpha_{\rm MLT} H_p$ (in units of the local pressure scale height H_p), and the prescription described in Cox and Giuli (1968). Overshoot is described with the coefficient $D_{\rm OD}$, given by:

$$D_{\rm OD} = D_{\rm conv,0} \exp\left(-\frac{2z}{f H_p}\right),$$

where $D_{\mathrm{conv},0}$ is the MLT derived diffusion coefficient, z is the distance in the radiative layer away from the overshoot zone, and $f = 0.0001$ is an adjustable parameter (see Heger et al. 2000). Semi-convection follows equation (12) of Paxton et al. (2013), with $\alpha_{\mathrm{sc}} = 0.01$. Thermohaline mixing is approximated as a diffusion process, whose diffusion coefficient is given by equation (14) of Paxton et al. (2013) with an efficiency of $\alpha_{\mathrm{th}} = 1.0$ following the prescription of Kippenhahn et al. (1980). The implementation of Red Giant Branch winds is not necessary, as we are looking for main-sequence parameters.

The required stellar parameters from this model are the luminosity L_*, the mass density ρ_* and temperature T of the stellar center, and the radius R_*. These quantities averaged over a representative main-sequence phase of the star are given in Table 3.1.1.

Table 3.1.1: Stellar parameters obtained from the 2 $M_\odot$ MESA-Web model, averaged over a time range from $t = 2.5 \cdot 10^6$ years to $t = 4.5 \cdot 10^8$ years.

Model	$\Omega_{\mathrm{ZAMS}}/\Omega_{\mathrm{crit}}$	$\overline{R}_*$ $[R_\odot]$	$\overline{\rho}_*$ $[\mathrm{kg\,m^{-3}}]$	$\overline{T}$ [K]	$\overline{L}_*$ $[L_\odot]$
A	0	2.18	$5.59 \cdot 10^4$	$2.29 \cdot 10^7$	24.20
B	0.05	2.17	$5.65 \cdot 10^4$	$2.27 \cdot 10^7$	24.30
C	0.5	2.22	$5.50 \cdot 10^4$	$2.25 \cdot 10^7$	22.79

It is clear that rotation does not seem to affect very much these parameters (as expected). Therefore, based on these results, the final parameters that will be used are $M_* = 2\ M_\odot$, $R_* = 2\ R_\odot$, $\rho_* = 5.6 \cdot 10^4\ \mathrm{kg\,m^{-3}}$, $T_* = 2.25 \cdot 10^7$ K and $L_* = 23\ L_\odot$.

Using these models it is also possible to estimate the size of the convective core Δr, information that will be useful to the setup of the MHD simulations. The upper panel of Figure 3.1.1 shows the superadiabaticity $\nabla - \nabla_{\mathrm{ad}}$ with the Schwarzschild criterion, and the lower panel the convective velocity of all models. These radial profiles correspond to $t_{\mathrm{age}} = 2.26 \cdot 10^8$ year. From both methods we can conclude that all models shows convection at roughly 13% of the normalized radius r/R, i.e. $\Delta r \sim 0.13\ R$. At other times during the main-sequence lifetime this value does not seem to change significantly.

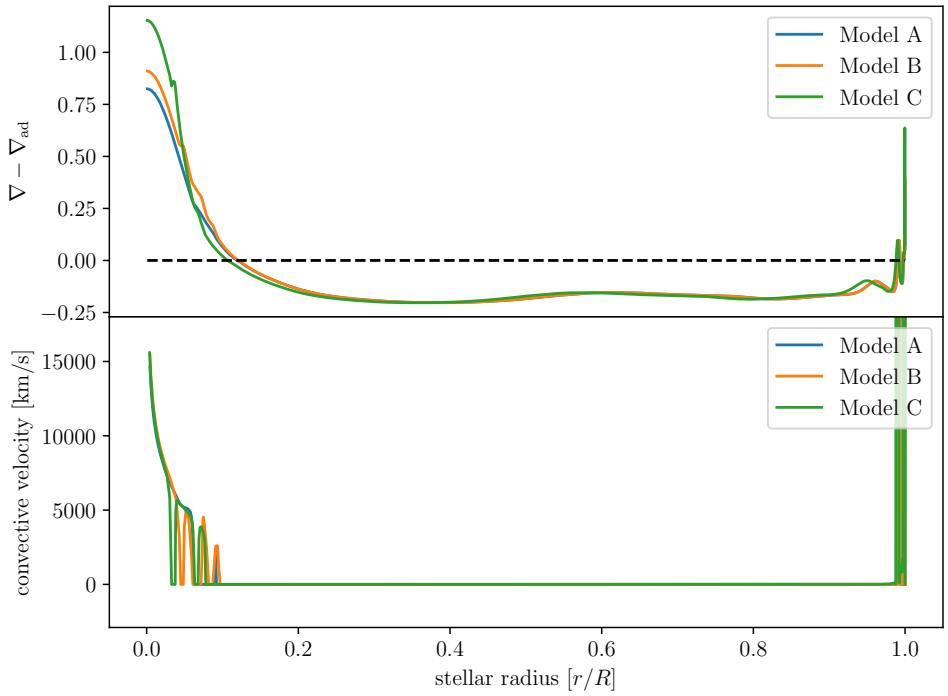

Figure 3.1.1: The superadiabaticity $\nabla - \nabla_{\rm ad}$, where the dashed line is the Schwarzschild criterion (*upper panel*) and the convective velocity (*lower panel*) of the MESA-Web models for a 2 $M_\odot$ A-type star, at $t_{\rm age} = 2.26 \cdot 10^8$ year.

3.2 The Pencil code

The Pencil Code[3] (Brandenburg and Dobler, 2002; Pencil Code Collaboration et al., 2021) is a high-order finite-difference code written in Fortran 95, primarily designed for turbulent flows, but well suited to deal with many dynamo problems, solving the non-ideal compressible magnetohydrodynamic equations. The code runs efficiently under MPI (Message Passing Interface) on multiprocessor computers with shared memory. Its first and second derivatives are defined as sixth order centered differences, giving it a high numerical accuracy. Furthermore, it uses an RK-2N time step, which refers to the third order Runge-Kutta scheme (Williamson, 1980), and it is defined in terms of the coefficients $c_{\delta t}$, $c_{\delta t,v}$ and $c_{\delta t,s}$

[3] http://pencil-code.nordita.org/

(which are inputs of the code) as:

$$\delta t = \min\left(c_{\delta t}\frac{\delta x_{\min}}{u_{\max}}, c_{\delta t,v}\frac{\delta x_{\min}^2}{D_{\max}}, c_{\delta t,s}\frac{1}{H_{\max}}\right), \tag{3.2.1}$$

where:

$$\begin{aligned}
\delta x_{\min} &= \min(\delta x, \delta y, \delta z),\\
u_{\max} &= \max(u + \sqrt{c_s^2 + v_A^2}),\\
D_{\max} &= \max(\nu, \gamma\chi, \eta, D),\\
H_{\max} &= \max\left(\frac{\text{entropy}_{\text{rhs}}}{c_{\text{V}}T}\right).
\end{aligned}$$

Here, c_s is the speed of sound, v_A is the Alfvén speed, ν is the kinematic viscosity, χ is the thermal diffusivity, γ is the adiabatic index, η is the magnetic diffusivity, and D is the passive scalar diffusivity. The quantity $\text{entropy}_{\text{rms}}$ describes the terms on the right side of the entropy equation.

3.2.1 Modularity

The Pencil Code is flexible to model many kinds of different systems. This is because individual physical processes are contained in *modules*, and they can be switched on or off depending on the modeled system. All the modules are contained in the file `src/Makefile.local`, inside the folder of the run. As an example, we have:

```
MPICOMM   =   mpicomm
IO        =   io_dist
FILE_IO   =   file_io_f95

HYDRO     =   hydro
DENSITY   =   density
ENTROPY   =   entropy
MAGNETIC  =   magnetic
RADIATION = noradiation
PSCALAR   = nopscalar
EOS       =   eos_idealgas
```

```
GRAVITY   =   gravity_r
FORCING   = noforcing
SHEAR     = noshear
TIMEAVG   = notimeavg

REAL_PRECISION = double
INITIAL_CONDITION = initial_condition/star_in_a_box_poly
```

which are the settings for the runs presented in Section 5.1. Here, the first line indicates that MPI communication will be used, for single processor runs we should use the module nompicomm. The 2nd line indicates that the input/output will be distributed, and the 3rd one states that a Fortran95-compatible input/output is used. The following lines are physics modules, where we have hydrodynamics (the equation of motion), density, the entropy equation, and magnetic field activated, while radiation and the passive scalar transport are not. Furthermore, the equation of state (`EOS`) is that of an ideal gas, the gravity will use the radial module, forcing and shear are switched off, and time averages are disabled. Double precision is used, i.e. 8-byte floating point numbers, and the last line corresponds to the polytropic initial condition for the star-in-a-box model.

3.2.2 Files in the run directories

As discussed, all the selected modules are contained in the file `src/Makefile.local` (from the run directory). The grid of the simulation and the total number of processors as well as how they are distributed along different directions (`nprocx`, `nprocy` and `nprocz`) is contained in the file `src/cparam.local`.

The initial conditions of the selected modules, along with the boundary conditions of the simulation, which are implemented through three layers of ghost points, are contained in the file `start.in`. The run parameters, like the mentioned coefficients to define the RK-2N time step, the time intervals to write the output files, and some physical quantities such as the rotation rate, diffusivities, and heat conductivity are defined in `run.in`.

Finally, the list of diagnostic variables that will appear in the time series and in the

phi-averages outputs (see section 3.2.3) are written in `print.in` and `phiaver.in`, respectively.

3.2.3 Output files

As an output of the code we have the time series, a text file which collects the evolution of the diagnostic quantities listed in `print.in`. Some useful variables to check the time evolution of the simulation, are:

- `it`: the current iteration of the run (where the step is defined as `it1` in `run.in`).
- `t`: the simulation time.
- `dt`: the simulation timestep.
- `urms`: the root-mean-square velocity $\sqrt{\langle \boldsymbol{u}^2 \rangle}$.
- `umax`: the maximum velocity $\max |\boldsymbol{u}|$.
- `brms`: the root-mean-square magnetic field $\sqrt{\langle \boldsymbol{B}^2 \rangle}$.
- `rhom`: the mean mass density $\langle \rho \rangle$.
- `ethm`: the mean thermal (internal) energy $\langle \rho e \rangle$.

The snapshot files contain the most primary quantities of the run (i.e. logarithmic density, flow velocity, magnetic vector potential and entropy), enough to restart the simulation at that specific time where the snapshot was written. There are two types of snapshots:

- The permanent ones `data/proc*/VAR`N, where $*$ denotes a folder per processor, and N is the number of the snapshot. The code writes them at a frequency `dsnap` indicated in `run.in`.
- The current one `data/proc*/var.dat`. This file will be overwritten with a frequency `isave`, indicated in `run.in`. The simulation as a default will start from this point if the run continues after some stop.

The slice files (also known as video files), contain the time evolution of specific variables on a specific plane. In `run.in`, the frequency of this output can be changed with `dvid`, and for spherical coordinates the parameters `r_rslice`,

`nth_rslice` and `nph_rslice` determine the position and the resolution of the slice.

Averages can be one- or two-dimensional, and they contain averaged quantities along one (or two) direction(s). For example, the variables contained in the files `xyaver.in`, `xzaver.in` and `yzaver.in`, are averaged over the direction of the first letters of each file. Finally, the Azimuthal averages (or phi-averages) correspond to quantities averaged over the azimuthal direction. In cylindrical coordinates, this is:

$$\overline{f}(\varpi, z, t) = \frac{1}{2\pi} \int f(\varpi, \phi, z) d\phi, \tag{3.2.2}$$

where $\varpi = r \sin\theta$ is the cylindrical radius. As mentioned earlier, the variables that are azimuthally averaged are listed inside `phiaver.in`.

3.3 The models

3.3.1 Whole star setup

The model used here is based in the star-in-a-box setup presented by Käpylä (2021), which is based in the setup by Dobler et al. (2006). The computational domain corresponds to a box of side $l = 2.2R$, where R is the stellar radius and all coordinates (x, y, z) range from $-l/2$ to $l/2$. The boundary conditions are impenetrable and stress-free conditions for flow ($u_n = 0$, $\partial_n \boldsymbol{u}_{\rm tan} = 0$, with $n = x, y, z$). The magnetic field is assumed to be perpendicular to the boundary ($\partial_n B_n = 0$, $\boldsymbol{B}_{\rm tan} = 0$). We further assume a vanishing second derivative for $\ln\rho$, and an assumed symmetric temperature across the exterior boundaries of the box. For the initial conditions, we considered low amplitude Gaussian noise for the flow and the magnetic field (which works as a magnetic initial seed).

We created two models, the first one corresponds initially to an isentropic polytrope i.e., with constant entropy, and therefore, it has a fully convective initial state. This model can be considered as an early pre-main-sequence evolutionary phase of an A-type star. This means it can work as a way of studying possible dynamos created during this phase, that in principle could become fossil fields later in its evolution. The results of this model are discussed in Chapter 4. The second model corresponds to a main-sequence A-type star. Here, we assumed a piecewise polytropic initial state between the gas pressure and density. A polytrope is

defined by:

$$p(\rho) = K_0 \rho^{\gamma}, \tag{3.3.1}$$

where K_0 is a constant, and:

$$\gamma = \frac{d \ln p}{d \ln \rho} = 1 + \frac{1}{n} \tag{3.3.2}$$

is the adiabatic index written in terms of the polytropic index n. Usually, values of n between 1 and 1.5 are used to describe unstable stratification, while values around 3 to describe stable layers (Braithwaite and Nordlund, 2006; Käpylä et al., 2010, 2020; Becerra et al., 2022). For this model, we defined a smooth profile for n given by:

$$n = \begin{cases} 1.5 & \text{if} \quad r < 0.2R \\ \\ 3.25 & \text{if} \quad r > 0.2R \end{cases}, \tag{3.3.3}$$

where the convective core is assumed to encompass 20% of the stellar radius. Numerical studies seem to agree that the convective core in A-type stars corresponds to $\sim 15\%$ of the stellar radius (see e.g. Browning et al., 2004; Brun et al., 2005; Featherstone et al., 2009). Also, as discussed in Section 3.1.3, our MESA models seem to indicate that this happens at roughly 13% of the stellar radius. Here, the choice of 20% represents a compromise between the size based in our MESA results (also, previous simulations), and computational feasibility, because modeling the whole star with a smaller core would require a higher resolution, and therefore more computational resources. The results of this model are discussed in Chapter 5.

The non-ideal fully compressible MHD equation set that is solved in each run (for both models) is given by:

$$\frac{\partial \boldsymbol{A}}{\partial t} = \boldsymbol{u} \times \boldsymbol{B} - \eta \mu_0 \boldsymbol{J}, \tag{3.3.4}$$

$$\frac{D \ln \rho}{D t} = -\boldsymbol{\nabla} \cdot \boldsymbol{u}, \tag{3.3.5}$$

$$\frac{D \boldsymbol{u}}{D t} = -\boldsymbol{\nabla} \Phi - \frac{1}{\rho} \left(\boldsymbol{\nabla} p - \boldsymbol{\nabla} \cdot 2 \nu \rho \boldsymbol{S} + \boldsymbol{J} \times \boldsymbol{B} \right) - 2 \boldsymbol{\Omega} \times \boldsymbol{u} + \boldsymbol{f}_d, \tag{3.3.6}$$

$$T \frac{D s}{D t} = -\frac{1}{\rho} \left[\boldsymbol{\nabla} \cdot \left(\boldsymbol{F}_{\text{rad}} + \boldsymbol{F}_{\text{SGS}} \right) + \mathcal{H} - \mathcal{C} + \mu_0 \eta \boldsymbol{J}^2 \right] + 2 \nu \boldsymbol{S}^2, \tag{3.3.7}$$

where $\boldsymbol{A}$ is the magnetic vector potential. It is worth to mention that writing the

induction equation (3.3.4) in terms of $\boldsymbol{A}$ allows to ensure the solenoidal conduction ($\boldsymbol{\nabla}\cdot\boldsymbol{B}=0$) during the whole run. $\boldsymbol{u}$ is the flow velocity, $\boldsymbol{B}=\boldsymbol{\nabla}\times\boldsymbol{A}$ is the magnetic field, η is the magnetic diffusivity, μ_0 is the magnetic permeability of vacuum, $\boldsymbol{J}=\boldsymbol{\nabla}\times\boldsymbol{B}/\mu_0$ is the current density given by Ampère's law, $D/Dt=\partial/\partial t+\boldsymbol{u}\cdot\boldsymbol{\nabla}$ is the advective (or material) derivative, ρ is the mass density, p is the pressure, Φ is the gravitational potential, that is fixed in space and it is given by the Padé approximation obtained from a spherically symmetric, hydrostatic, selfgravitating model (see Appendix A of Dobler et al., 2006):

$$\Phi(r)=-\frac{GM}{R}\frac{a_0+a_2r'^2+a_3r'^3}{1+b_2r'^2+b_3r'^3+a_3r'^4}, \tag{3.3.8}$$

where $r'=r/R$, G is the gravitational constant, M is the mass of the star, and for an A0-type star the coefficients are given by $a_0=4.3641$, $a_2=-1.5612$, $a_3=0.4841$, $b_2=4.0678$ and $b_3=1.2548$. $\boldsymbol{S}$ is the traceless rate-of-strain tensor, given by:

$$S_{ij}=\frac{1}{2}(\partial_j u_i+\partial_i u_j)-\frac{1}{3}\delta_{ij}\boldsymbol{\nabla}\cdot\boldsymbol{u} \tag{3.3.9}$$

that corresponds to equation (2.2.9). T is the temperature, $\boldsymbol{\Omega}=(0,0,\Omega_0)$ is the rotation rate of the star along the z axis. $\boldsymbol{f}_{\rm d}$ describes damping of flows exterior to the star, given by:

$$\boldsymbol{f}_d=-\frac{\boldsymbol{u}}{\tau_{\rm damp}}f_e(r), \tag{3.3.10}$$

where $\tau_{\rm damp}\approx 1.4$ days is the damping timescale, which is short compared to other timescales in the simulation. The function $f_e(r)$ is defined as:

$$f_e(r)=\frac{1}{2}\left(1+\tanh\frac{r-r_{\rm damp}}{w_{\rm damp}}\right), \tag{3.3.11}$$

where $r_{\rm damp}=1.03R$ is the damping radius and $w_{\rm damp}=0.02R$ its width. Radiation inside the star is approximated as a diffusion process. Therefore, the radiative flux is given by:

$$\boldsymbol{F}_{\rm rad}=-K\boldsymbol{\nabla}T, \tag{3.3.12}$$

where K is the radiative heat conductivity, a quantity that is assumed to be constant. In addition, it is convenient to introduce a subgrid-scale (SGS) entropy diffusion that does not contribute to the net energy transport, but damps

fluctuations near the grid scale. This is given by the SGS entropy flux:

$$\boldsymbol{F}_{\rm SGS} = -\chi_{\rm SGS}\rho\boldsymbol{\nabla}s', \tag{3.3.13}$$

where $\chi_{\rm SGS}$ is the SGS diffusion coefficient, and:

$$s' = s - \langle s\rangle_t$$

is the fluctuating entropy, where $\langle s\rangle_t$ is defined as a running temporal mean of the specific entropy. $\mathcal{H}$ and $\mathcal{C}$ describe additional heating and cooling, respectively, and we adopted similar expressions as Dobler et al. (2006) and Käpylä (2021), where

$$\mathcal{H}(r) = \frac{L_{\rm sim}}{(2\pi w_L^2)^{3/2}}\exp\left(-\frac{r^2}{2w_L^2}\right)$$

is a normalized Gaussian profile given by the parameterization of the nuclear energy production inside the core of the star, where $L_{\rm sim}$ is the luminosity in the simulation, and $w_L = 0.1R$ is the width of the Gaussian. And $\mathcal{C}(\boldsymbol{x})$ models the radiative losses above the stellar surface, and it is given by:

$$\mathcal{C}(\boldsymbol{x}) = \rho c_{\rm P}\frac{T(\boldsymbol{x}) - T_{\rm surf}}{\tau_{\rm cool}}f_e(r),$$

where $c_{\rm P}$ is the heat capacity at constant pressure, $T_{\rm surf} = T(R)$ is the temperature on the surface of the star, $\tau_{\rm cool} = \tau_{\rm damp}$ is a cooling timescale, and $f_e(r)$ is given by equation (3.3.11), with the same parameters. We assume an ideal gas equation of state:

$$p = \mathcal{R}\rho T = (\gamma - 1)\rho e, \tag{3.3.14}$$

where $\mathcal{R}$ is the ideal gas constant, and e is the internal energy of the gas.

Following Käpylä (2022), in order to avoid diffusive spreading of magnetic fields and flows from the core to the envelope, the convective core model has radial profiles for the diffusivities ν and η, where the radiative layers have values 10^2 times smaller than the core. The disadvantage of this implementation is that we already had low diffusivities in the convective core, otherwise the Reynolds number would have been too low. This produces values in the radiative envelope that are hard to resolve using our current resolution. However, a way to deal with this issue, is adding artificial sixth-order hyper diffusivity terms in the dynamical equations.

This works as a numerical tool which smooths out the smallest scales, dissipating the energy and preventing instabilities (for some examples, see Brandenburg and Sarson, 2002; Johansen and Klahr, 2005). In this context, the momentum equation (3.3.6) requires an additional term, given by the hyperviscosity force. To define it, we used the resolution-independent mesh hyper-Reynolds number method described in Appendix A of Lyra et al. (2017). The idea of this method is to keep the (3rd-order) quantity:

$$\mathrm{Re}^{(3)}_{\mathrm{grid}} = \frac{u_{\mathrm{rms}}}{\nu_3^{\mathrm{mesh}} k_{\mathrm{Ny}}^5} = \frac{u_{\mathrm{rms}} \Delta q^5}{\nu_3^{\mathrm{mesh}} \pi^5}$$

constant with resolution, where $k_{\mathrm{Ny}} = \pi/\Delta q$ is the Nyquist wavenumber, and Δq is the line element. Now, the coefficient ν_3^{mesh} can be obtained as:

$$\nu_3^{\mathrm{mesh}} = \frac{u_{\mathrm{rms}} \Delta q^5}{\mathrm{Re}^{(3)}_{\mathrm{grid}} \pi^5}.$$

Furthermore, the hyperviscous force is given by:

$$f_{\mathrm{visc}}^{(\mathrm{hyper})} = \nu_3^{\mathrm{mesh}} \frac{\Delta^6 \nu}{\Delta q^6} = \frac{u_{\mathrm{rms}}}{\mathrm{Re}^{(3)}_{\mathrm{grid}} \pi^5} \frac{\Delta^6 \nu}{\Delta q}.$$

Analogously, the induction equation (3.3.4) requires an additional term related to the magnetic hyperdiffusivity. Using the same approach we obtained:

$$f_{\mathrm{diff}}^{(\mathrm{hyper})} = \eta_3^{\mathrm{mesh}} \frac{\Delta^6 \eta}{\Delta q^6} = \frac{u_{\mathrm{rms}}}{\mathrm{Re}^{(3)}_{\mathrm{Mgrid}} \pi^5} \frac{\Delta^6 \eta}{\Delta q}$$

3.3.2 Zoom setup

Modelling the whole star allows us to study the convective core and also the surface of the star. However, this also reduces the number of grid points available to resolve convection inside the core. The result of this is that slow rotators might not be dynamos due to the too low $\mathrm{Re_M}$ in the core.

As a way to deal with this problem without increasing the resolution, and computation time, we ran some simulations using a zoom model, which is otherwise essentially the same as the polytropic model, but the box has a side of $l = 1.1R$. This excludes the surface of the star, and gives higher resolution and Reynolds

numbers in the core.

The radius of the damping of flows was changed to $r_{\rm damp} = 0.45R$ with $\tau_{\rm damp} \approx 0.15$ days, and $w_{\rm damp} = 0.01R$. Finally, as a way to preserve the thermal equilibrium of the star, the cooling now starts at $r_{\rm cool} = 0.52R$, inside the radiative zone. Both radii were conveniently modified to give stability to the model. However, this does not affect the main results as we are not interested in what is happening far away from the core.

This model is denoted as "zMHD" in Chapter 5, while the model of the whole star is "MHD".

3.3.3 Physical units and relation to reality

The Pencil Code expresses all the output variables in dimensionless code units. Therefore, in order to analyze the results in physical units it is necessary to do a relation to reality through scale factors. This requires the stellar parameters of the star to be known. For the stellar radius R_*, the luminosity L_*, the mass M_*, and the central density ρ_* we will be using the values computed from our MESA models in Section 3.1.3. These models also give the surface gravity:

$$g_* = \frac{GM_*}{R_*^2} \approx \frac{2}{2^2}\frac{GM_\odot}{R_\odot^2} \approx 150\ \frac{\rm m}{\rm s^2}. \tag{3.3.15}$$

However, using realistic parameters we would notice a gap between the acoustic (dynamic) and the Kelvin-Helmholtz (thermal) timescales:

$$\tau_{\rm dyn} = \sqrt{\frac{R^3}{GM}}, \qquad\qquad \tau_{\rm KH} = \frac{GM^2}{RL},$$

so in principle, both could not be resolved in one single simulation (running it for a feasible amount of time). A solution to this problem was originally pointed out by Chan and Sofia (1986), and it consists of exaggerating the luminosity in numerical simulations. Here we use the enhanced luminosity approach, originally defined by Dobler et al. (2006), where the dimensionless luminosity (which corresponds to the ratio between $\tau_{\rm dyn}$ and $\tau_{\rm KH}$) is given by:

$$\mathcal{L} = \frac{L}{\sqrt{G^3M^5/R^5}}. \tag{3.3.16}$$

This allows to define the luminosity ratio $L_{\rm ratio} = \mathcal{L}_{\rm sim}/\mathcal{L}_{\rm star}$, and therefore, now the Kelvin-Helmholtz timescale scales as $\tau_{\rm KH} \propto L_{\rm ratio}^{-1}$. The temperature scales as $T \propto L_{\rm ratio}^{-2/3}$ (Käpylä et al., 2020), and therefore, this produces a rescaling proportional to $L_{\rm ratio}^{-1/3}$ for the sound speed c_s. For a star close to hydrostatic equilibrium, $\tau_{\rm dym}$ can be also estimated by the time it takes for a sound wave to travel from the centre to the stellar surface if the gravity suddenly disappears. Therefore, we assume that $\tau_{\rm dym} \propto L_{\rm ratio}^{1/3}$. Now, the gap between both timescales is reduced by a cumulative factor of $L_{\rm ratio}^{4/3}$.

We used the mentioned stellar parameter for both models, which implies that the fully convective protostar is close to entering the main sequence. However, the pre-main sequence model has a different input luminosity, and therefore the values of $L_{\rm ratio}$ between both models are different; as we can see in Table 3.3.1. This is why a comparison between both should be made with caution. Notice that both values of $\mathcal{L}$ are smaller than the unity, which in principle is good because it is something that we might expect from realistic models.

Table 3.3.1: Dimensionless luminosities computed with the simulation and stellar parameters, for the protostar (fully convective) and the main-sequence (partially convective) models. The third column gives the ratio between both.

Model	$\mathcal{L}_{\rm sim}$	$\mathcal{L}_{\rm star}$	$L_{\rm ratio}$
Protostar	$8.64 \cdot 10^{-4}$	$2.98 \cdot 10^{-11}$	$2.90 \cdot 10^{7}$
A-type star	$2.59 \cdot 10^{-4}$	$2.98 \cdot 10^{-11}$	$8.69 \cdot 10^{6}$

Numerical simulations have reported that the convective velocity scales with the luminosity as $u_{\rm conv} \propto L^{1/3}$ (Jones et al., 2017; Andrassy et al., 2020; Käpylä et al., 2020; Baraffe et al., 2023). This implies $u_{\rm conv} \propto L_{\rm ratio}^{1/3}$ in our simulations. Therefore, in order to have a consistent rotational influence on the flow, we need to enhance the rotation rate by the same factor. Following Appendix A of Käpylä et al. (2020), we have:

$$\Omega_{\rm sim} = L_{\rm ratio}^{1/3} \left(\frac{g_{\rm sim}}{g_*} \frac{R_*}{R_{\rm sim}} \right)^{1/2} \Omega. \tag{3.3.17}$$

For length, time, and velocity we have the following conversions:

$$[x] = \frac{R_*}{R_{\rm sim}}, \qquad [t] = \frac{\Omega_{\rm sim}}{\Omega_*}, \qquad [\boldsymbol{u}] = \frac{[x]}{[t]} = \frac{R_* \Omega_*}{R_{\rm sim} \Omega_{\rm sim}}, \tag{3.3.18}$$

and for the density and the magnetic field:

$$[\rho] = \rho_*, \qquad [\boldsymbol{B}] = \left[\frac{\mu_0 \rho_* (\Omega_* R_*)^2}{\mu_{\rm sim} \rho_{\rm sim} (\Omega_{\rm sim} R_{\rm sim})^2}\right]^{1/2}. \tag{3.3.19}$$

Note that the subindex sim corresponds to the values chosen in the simulation (code units), and in this model $R_{\rm sim} = \mu_{\rm sim} = \rho_{\rm sim} = g_{\rm sim} = 1$.

3.3.4 Diagnostic quantities

The dimensionless parameters described in Section 2.2.3 are used to characterize the system in our simulations, more specifically:

$$\mathrm{Re} = \frac{u_{\rm rms}}{\nu k_R}, \qquad \mathrm{Re_M} = \frac{u_{\rm rms}}{\eta k_R},$$

for the fluid and magnetic Reynolds numbers, respectively, where $k_R = 2\pi/\Delta r$ is the scale of largest convective eddies. The Coriolis number is given by:

$$\mathrm{Co} = \frac{2\Omega_0}{u_{\rm urms} k_R}.$$

The magnetic and SGS Prandtl number are:

$$\mathrm{Pr_M} = \frac{\nu}{\eta}, \qquad \mathrm{Pr_{SGS}} = \frac{\nu}{\chi_{\rm SGS}},$$

and the SGS Péclet number is defined as:

$$\mathrm{Pe} = \frac{u_{\rm urms}}{\chi_{\rm SGS} k_R}.$$

Chapter 4

Three-dimensional MHD simulations of a fully convective star: protostellar phase

In this Chapter, the results of the fully convective model described in Section 3.3.1 are listed, including dynamo solutions with time-latitude diagrams of the averaged toroidal magnetic field, the analysis of large-scale flows, energies, i.e., kinetic (total, differential rotation, and meridional circulation) and magnetic (total, toroidal, and poloidal), and the spherical harmonics decomposition. Some of these results were published in Hidalgo et al. (2023). The analysis of the magnetic field was made during the saturated phase of the simulations, i.e., we start with a magnetic field seed (~ 1 G) which is amplified exponentially during the kinematic phase, and once this growth ceases we perform the analysis (for an example, see Figure 5.1.1 and Chapter 5).

4.1 Simulations

As discussed before, this fully convective setup has an isentropic initial state ($\Delta r = 1$). This is a useful scenario to test the setup, and also as we discussed in Section 3.3.1, it is representative of the pre-main-sequence evolution of the star.

These simulations were divided into two groups. The first group (A) corresponds to a set with heat conductivity $K = 0.01K_0$, where K_0 is the value required to

obtain a fully radiative saturated configuration. The diffusivities are given by $\nu = 2.08 \cdot 10^9$ [m^2/s], and $\eta = \chi_{\rm SGS} = 1.04 \cdot 10^9$ [m^2/s], except in Ar3* where diffusivities where diminished by a factor of 10. The second group (B) has an enhanced heat conductivity $K = 0.04K_0$, which also gives a fully convective configuration once relaxed, and diffusivities given by $\nu = 1.19 \cdot 10^9$ [m^2/s], and again, $\eta = \chi_{\rm SGS} = 1.04 \cdot 10^9$ [m^2/s]. This gives $\mathrm{Pr_M} = \mathrm{Pr_{SGS}} = 2$ for group A and $\mathrm{Pr_M} = \mathrm{Pr_{SGS}} = 1.14$ for group B. The runs, as well as the diagnostic quantities, are listed in Table 4.1.1. All simulations were run on a grid of 128^3.

Table 4.1.1: Summary of all the fully convective model runs. From left to right the columns correspond to the rotation period $P_{\rm rot} = 2\pi/\Omega_0$, the volume-averaged root-mean-square flow velocity $\langle u_{\rm rms} \rangle$, the volume-averaged root-mean-square magnetic field $\langle B_{\rm rms} \rangle$, the Coriolis number, the Reynolds number and the magnetic Reynolds number (which equals the SGS Péclet number in both groups).

Run	$P_{\rm rot}$ [days]	$\langle u_{\rm rms} \rangle$ [m/s]	$\langle B_{\rm rms} \rangle$ [kG]	Co	Re	$\mathrm{Re_M}$
Ar0	-	165	no dynamo	0	18	35
Ar1	192	126	84	1.3	14	27
Ar2	38	82	50	10.2	9	18
Ar3	20	53	127	31.6	6	11
Ar3*	20	57	152	29.4	61	121
Br0	-	117	no dynamo	0	22	25
Br1	280	113	56	1	21	24
Br2	140	98	83	2.5	18	20

The density and entropy profiles of Ar1 and Br1 are shown in Figure 4.1.1. Both thermodynamic quantities are averaged in time and azimuth over the thermally saturated phase. The density stratification is $\overline{\rho}_{\rm center}/\overline{\rho}_{\rm surface} \approx 9.5$ in both groups. And both entropy profiles have a gradient close to zero inside the star, which is the expected configuration for a fully convective star. The temperature profiles of the same runs are shown in Figure 4.1.2. Here, we used $[T] = T_* = 2.25 \cdot 10^7$ K (see Section 3.1.3) to obtain the physical units. Again, T is azimuthally and temporally averaged, and the ratio between the temperature at the center and at surface is $\overline{T}_{\rm center}/\overline{T}_{\rm surface} \approx 5$.

4.2 Dynamo solutions

All rotating runs (Ar[1-3] and Br[1-2]) generate large-scale magnetic fields. The azimuthally averaged toroidal magnetic field B_ϕ following equation (3.2.2), at the

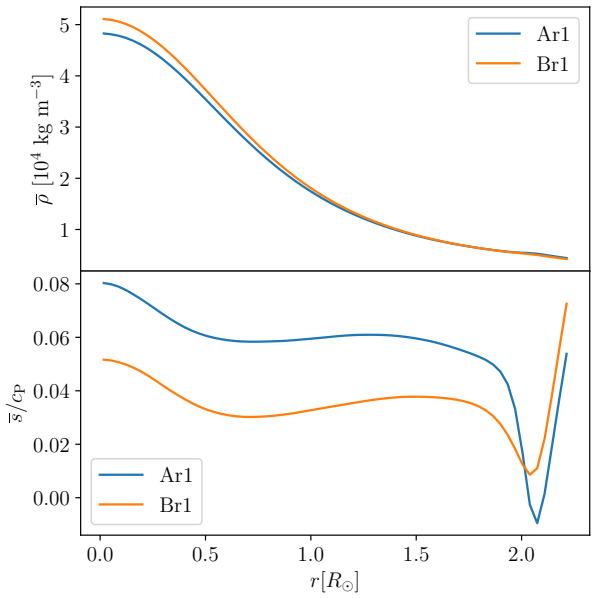

Figure 4.1.1: *Top panel*: Density profile from Ar1 and Br1. *Bottom panel*: Entropy profiles from the same runs. Both quantities are time-averaged over the thermally relaxed times.

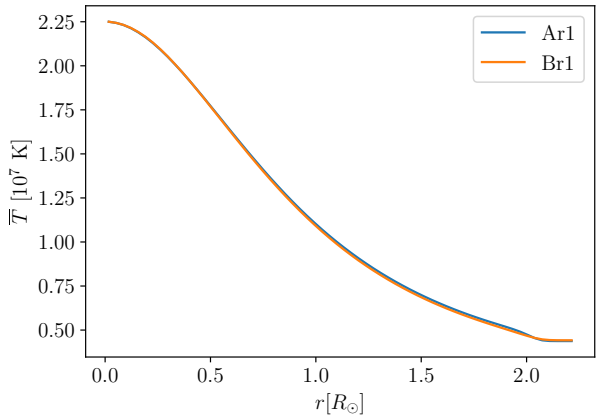

Figure 4.1.2: Temperature profile from Ar1 and Br1. $\overline{T}$ is averaged over the thermally relaxed times.

surface of the star ($r = R$) are shown in Figure 4.2.1 as time-latitude diagrams. The upper left panel shows $\overline{B}_\phi(R, \theta, t)$ from run Ar1. A quasi-stationary magnetic field with no cyclic sign reversals is visible. Furthermore, the field has a dipolar structure where both polarities are located in the northern hemisphere, more specifically, the positive is located between $60° < \theta < 90°$, and the negative roughly between $-20° < \theta < 60°$. Interestingly, steady dipolar configurations

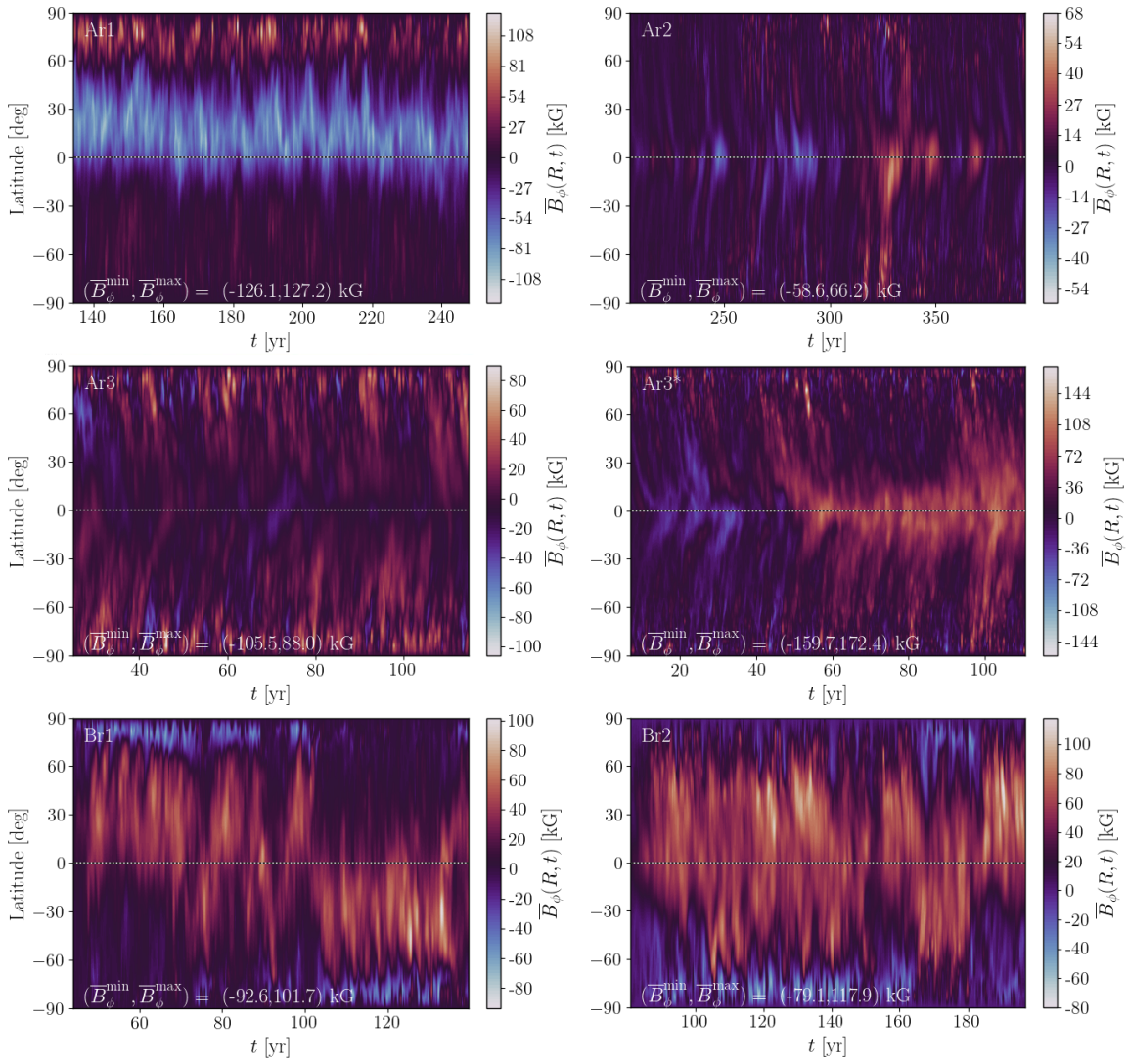

Figure 4.2.1: Time-latitude diagrams of the azimuthally averaged toroidal magnetic field $\overline{B}_\phi(R, \theta, t)$, where the run is indicated in the upper left, and the minimum and maximum field strength at the bottom of each panel.

have been found in slow rotators previously (Käpylä, 2021; Ortiz-Rodríguez et al., 2023), but with no single-hemispheric behavior. The upper right panel shows the results for Ar2. Here we present 400 years in order to address a relevant portion of the magnetic evolution. The magnetic activity seems to be concentrated at the equator, having a polarity change after $\sim$ 100 years, although it is not clear if this behavior is cyclic or not. Structures at different latitudes seem to migrate towards the equator in short periods of time. The diagrams of Ar3 and Ar3* are given in the middle panels, left and right, respectively. Ar3 has no clear cycle nor a steady solution; however, the magnetic activity seem to be stronger close to the

pole, with some sign reversals and structures which move to the equator before vanishing. On the other hand, Ar3* is similar to Ar2, with stronger values in the equator, and structures that come from regions close to the poles. Run Ar3* has a polarity change in the equator after roughly 40 years, which in principle seems to happen faster than in Ar2, but this behavior is most likely random, so a conclusion based on the global time is not very relevant. The lower panels of Figure 4.2.1 represent the rotating runs from group B. On the left side, we find a quasi-steady configuration for Br1, which corresponds to a single-hemispheric dipole similar to Ar1 but with opposite polarity. In the first years of the simulation the activity is more concentrated in the northern hemisphere, and after ~ 50 years it migrates towards the southern hemisphere, keeping the negative polarity at the pole. On the right side of the lower plots, we can also find a quasi-stationary large-scale field without sign reversals for Br2, unlike Ar1 and Br1, this field is not hemispheric. This configuration is similar to the slow rotator in the fully convective model of Käpylä (2021).

4.3 Large-scale flows

The time- and azimuthally-averaged rotation rate is given by:

$$\overline{\Omega}(\varpi, z) = \Omega_0 + \overline{U}_\phi(\varpi, z)/\varpi, \tag{4.3.1}$$

where $\varpi = r\sin\theta$ is the cylindrical radius. The profiles of this quantity are given in Figure 4.3.1 for simulations from group A, and in Figure 4.3.2 for group B. Each plot includes the maximum value of the averaged meridional flow, which is given by:

$$\overline{\boldsymbol{U}}_{\rm mer}(\varpi, z) = (\overline{U}_\varpi, 0, \overline{U}_z). \tag{4.3.2}$$

Also, the plots are clipped for a better display of the zones with rotation different than Ω_0. The vertical axis of the plots represents the z axis of the simulations, that is the direction where the rotation axis is pointing, as mentioned in Section 3.3.1. The dashed line at $z = 0$ on each plot represents the equator.

The differential rotation parameters $\Delta_\Omega^{(r)}$ and $\Delta_\Omega^{(\bar{\theta})}$ (Käpylä et al., 2013; Käpylä, 2021; Ortiz-Rodríguez et al., 2023) are used to quantify the amplitude of the radial

and latitudinal differential rotation, given by:

$$\Delta_{\Omega}^{(r)} = \frac{\overline{\Omega}(r_{\rm top}, \theta_{\rm eq}) - \overline{\Omega}(r_{\rm bot}, \theta_{\rm eq})}{\overline{\Omega}(r_{\rm top}, \theta_{\rm eq})}, \qquad \Delta_{\Omega}^{(\bar{\theta})} = \frac{\overline{\Omega}(r_{\rm top}, \theta_{\rm eq}) - \overline{\Omega}(r_{\rm top}, \bar{\theta})}{\overline{\Omega}(r_{\rm top}, \theta_{\rm eq})}, \tag{4.3.3}$$

where $r_{\rm top} = 0.9R$ and $r_{\rm bot} = 0.1R$ are the radius near the top and bottom of the star, respectively. $\theta_{\rm eq}$ corresponds to the latitude at the equator, and $\bar{\theta}$ is an average of $\overline{\Omega}$ between latitudes $-\theta$ and θ. These parameters are summarized in Table 4.3.1.

Table 4.3.1: Differential rotation parameters for all simulations, obtained from the averaged (azimuthally and temporally) angular velocity $\overline{\Omega}(r, \theta)$.

Run	$\Delta_{\Omega}^{(r)}$	$\Delta_{\Omega}^{\bar{\theta}}(60°)$	$\Delta_{\Omega}^{\bar{\theta}}(75°)$
Ar1	-1.0119	-0.0225	-0.0915
Ar2	-0.1336	0.0088	0.0265
Ar3	-0.0475	0.0085	0.0072
Ar3*	-0.0225	0.0091	0.0181
Br1	-1.8823	-0.5047	-0.9792
Br2	-0.4099	0.0871	0.1089

From this table we find that all the runs have anti-solar differential rotation in the equator. This is described by negative values of $\Delta_{\Omega}^{(r)}$, that indicate that the star is rotating faster near the center than near the surface. This result is similar to the one reported in Dobler et al. (2006), where all the runs have anti-solar differential rotation. Moreover, the slowest rotators from both groups (Ar1 and Br1) have also negative $\Delta_{\Omega}^{(\bar{\theta})}$, and the biggest differential rotation amplitudes ($|\Delta_{\Omega}^{(r)}|$ and $|\Delta_{\Omega}^{(\bar{\theta})}|$). This is something that can be also found in the slowest rotator from Käpylä (2021). Besides, run MHD1 from that work has a very similar rotation profile to Br1 (see the left panel of Figure 4.3.2), i.e., symmetric with respect to the equator, even though its large-scale magnetic field seems to be closer to Br2, as we already discussed. However, the rotation profile of Br2 seems to be hemispheric and asymmetric, there is no clear reason of why this is happening, but something similar was found by Dobler et al. (2006) (see the rotation profiles of their runs 2d and 2e). It is worth mentioning that their run 2b also has a similar rotation profile to Br1.

From the upper left panel of Figure 4.3.1, we notice that the differential rotation of Ar1 at $r_{\rm top}$ is more prominent in the southern hemisphere. This is in agreement

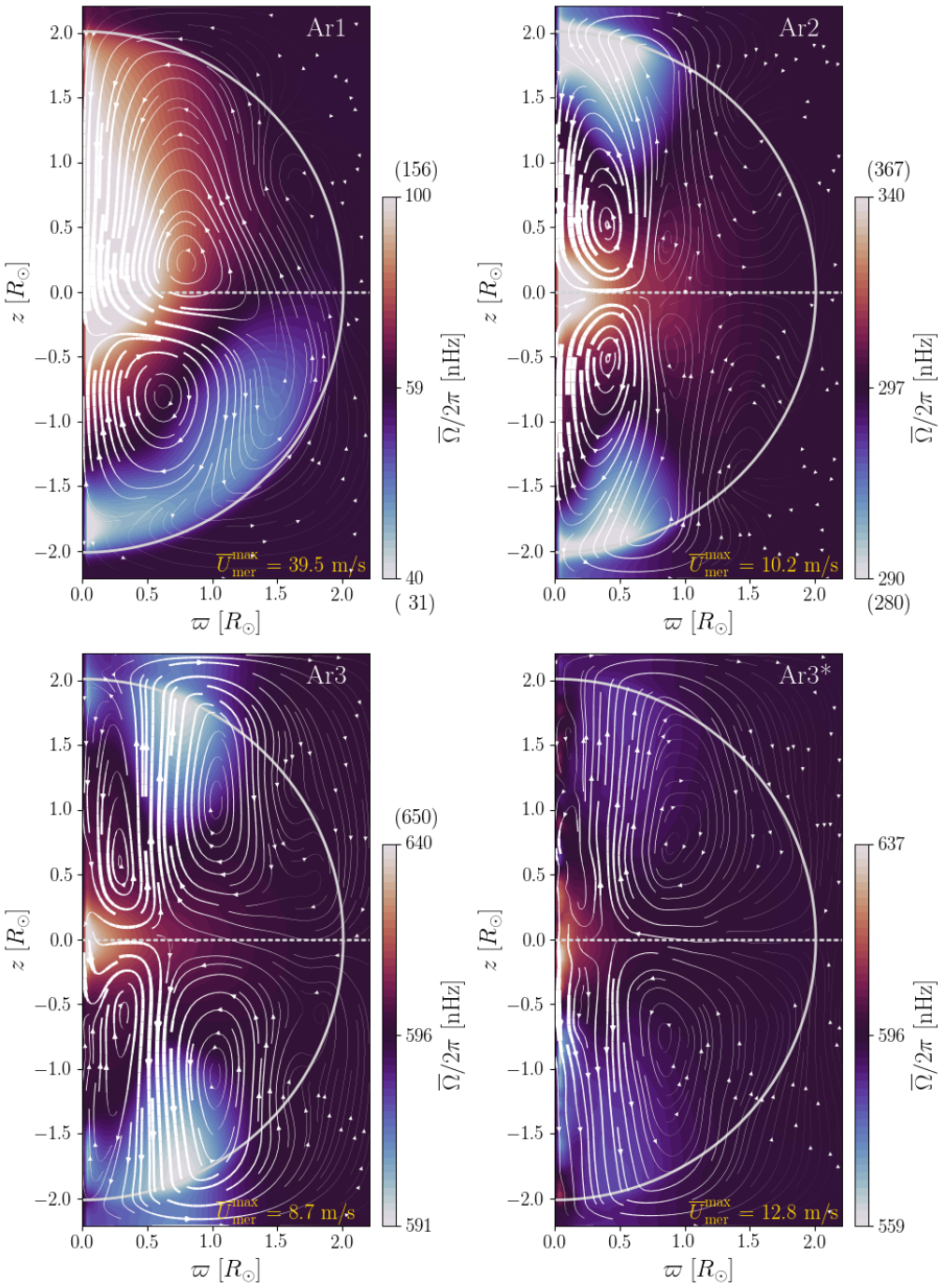

Figure 4.3.1: Profiles of the temporally and azimuthally averaged rotation rate $\overline{\Omega}(\varpi, z)$ for runs from group A. The colorbar was clipped in some cases to highlight different features in the plot. The maximum and minimum values are indicated in parenthesis above and below the colorbar. The streamlines indicate the mass flux due to meridional circulation and the dotted line is the equator.

with the time-latitude diagram of $\overline{B}(R, t)$ showed in Figure 4.2.1; the magnetic field is mostly located in the northern hemisphere, and this might be quenching

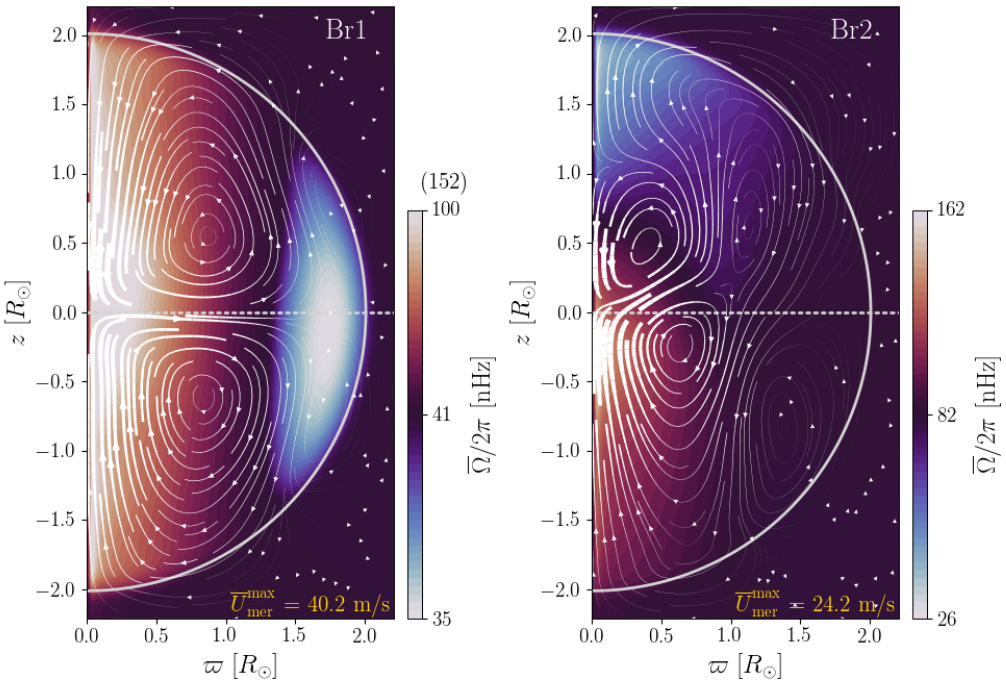

Figure 4.3.2: Rotation profiles $\overline{\Omega}(\varpi, z)$. Same as Figure 4.3.1, but for runs from group B.

the differential rotation in this zone. The rest of runs can be considered fast rotators, because in all the remaining cases (Ar[2-3] and Ar3*) the Coriolis number is exceeding 10. From Table 4.3.1 we can see that $\Delta_\Omega^{(\bar{\theta})}$ is very close to zero in all these runs, which means that the star is rotating almost as a rigid body, with very small variations of $\overline{\Omega}(\varpi, z)$. Furthermore, from Figure 4.3.1, we can see that the maximum and minimum values of Ar3 and Ar3* are very close to Ω_0. Moreover, the differential rotation seems to quench even more as a consequence of reducing the diffusivities. Also, these runs seem to follow the Taylor-Proudman state, because the fluid tends to be aligned parallel to the axis of rotation, due to the Coriolis force. This is more visible in snapshots of the runs (see Figure 4.3.3).

Finally, we notice that as we increase the rotation rate, the maximum value of the averaged meridional flow decreases. However, decreasing the diffusivities seems to also affect this value, as we can see from Ar3*, where the maximum value is slightly higher than in Ar3.

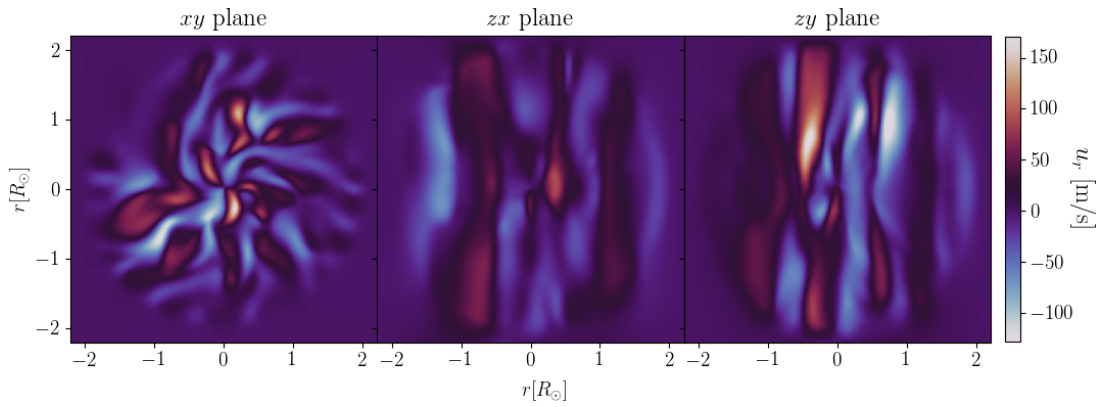

Figure 4.3.3: Snapshot from run Ar3 at $t = 115$ [yr]. The left plot corresponds to the equatorial plane, and the middle and right plots to the planes that contain the axis of rotation (zx and zy respectively). The colorbar represents the radial component of the flow velocity u_r.

4.4 Energy analysis

The total kinetic and magnetic energies, respectively, are given by:

$$E_{\rm kin} = \frac{1}{2}\int \langle \rho \boldsymbol{U}^2 \rangle dV, \qquad E_{\rm mag} = \frac{1}{2\mu_0}\int \langle \boldsymbol{B}^2 \rangle dV, \tag{4.4.1}$$

where the brackets denote volume average for radii $r < R$. The energies for the differential rotation (DR) and meridional circulation (MC), are defined as:

$$E^{\rm DR}_{\rm kin} = \frac{1}{2}\int \langle \rho \overline{U}^2_\phi \rangle dV, \qquad E^{\rm MC}_{\rm kin} = \frac{1}{2}\int \langle \rho (\overline{U}^2_\varpi + \overline{U}^2_z) \rangle dV. \tag{4.4.2}$$

The toroidal and poloidal magnetic energies are given by:

$$E^{\rm tor}_{\rm mag} = \frac{1}{2\mu_0}\int \langle \overline{B}^2_\phi \rangle dV, \qquad E^{\rm pol}_{\rm mag} = \int \frac{1}{2\mu_0} \langle (\overline{B}^2_\varpi + \overline{B}^2_z) \rangle dV. \tag{4.4.3}$$

These energies from both sets of simulations are listed in Table 4.4.1.

The slowest rotators Ar1 and Br1, have the highest kinetic energies, and also the highest energies for the differential rotation, i.e, 21% and 31%, respectively. This is consistent with the values shown in Table 4.3.1. Also, the meridional circulation energy is also the highest in these runs. The ratio $E^{\rm DR}_{\rm kin}/E_{\rm kin} = 0.312$ of Br1 is comparable to the ratio of MHD1 (0.306) from Käpylä (2021). This is an expected result, as we already discussed how the rotation profiles of these

Table 4.4.1: Kinetic and magnetic energies, averaged over time and volume. The total kinetic and magnetic energies have units of 10^{35}J, while the rest of energies are written as fractions of these quantities.

Run	$E_{\rm kin}$	$E_{\rm kin}^{\rm DR}/E_{\rm kin}$	$E_{\rm kin}^{\rm MC}/E_{\rm kin}$	$E_{\rm mag}$	$E_{\rm mag}^{\rm tor}/E_{\rm mag}$	$E_{\rm mag}^{\rm pol}/E_{\rm mag}$
Ar1	11.53	0.211	0.077	2.84	0.182	0.116
Ar2	6.23	0.113	0.021	0.65	0.057	0.050
Ar3	2.89	0.085	0.022	5.96	0.035	0.041
Ar3*	3.58	0.052	0.040	11.24	0.072	0.064
Br1	11.94	0.312	0.070	1.59	0.190	0.114
Br2	8.46	0.216	0.068	2.92	0.224	0.100

runs are very similar. Notice that Coriolis numbers are similar, with Co = 0.7 and Co = 1 for MHD1 and Br1, respectively. Br2 has the highest toroidal energy (22%), and 10% of the magnetic energy corresponds to poloidal energy. This is the highest value after Ar1 and Br1. Futhermore, Ar2 has the lowest value of the total magnetic energy. This is consistent with the latitude-diagram of the run. In Figure 4.2.1 it is visible that the lowest maximum and minimum (in amplitude) values of the averaged toroidal field correspond to Ar2. The fast rotators, Ar3 and Ar3* have the lowest values of the total kinetic energy; as rotation increases the flow velocity reduces (see Figure 4.3.1). However, Ar3* shows the highest value of magnetic energy, and this is an expected result, because diffusivities are lower in this run. This can be confirmed in Table 4.1.1, where Ar3* has the highest value of $\langle B_{\rm rms}\rangle$ with 95 kG; and in Figure 4.2.1, where Ar3* has also the highest amplitude values for the maximum and minimum $\overline{B}_\phi(R,t)$, with -159.7 kG and 172.4 kG respectively. Finally, analyzing columns 2 and 5 of Table 4.4.1, we find that the slow rotators have magnetic energies below equipartition (where equipartition is $E_{\rm mag}/E_{\rm kin} = 1$), with 0.247 for Ar1, 0.105 for Ar2, 0.133 for Br1 and 0.345 for Br2. However, the fast rotators reach super-equipartition, where the magnetic energy is roughly twice the kinetic energy in Ar3, and thrice in Ar3*.

4.5 Spherical harmonic decomposition and power spectra

In principle, an astrophysical dynamo can operate on large scales, but also on small scales. This is something that can be analyzed using the spherical harmonic decomposition. These functions come originally from the solution of the Laplace

equation, and they are given by:

$$Y_l^m(\theta,\phi) = (-1)^m \sqrt{\frac{2l+1}{4\pi}} \cdot \sqrt{\frac{(l-m)!}{(l+m)!}} \cdot P_l^m(\cos\theta) \cdot e^{im\phi}, \tag{4.5.1}$$

where $P_l^m(\cos\theta)$ are the associated Legendre polynomials, and e the exponential function. The advantage of the spherical harmonics, is that any function $F(\theta,\phi)$ whose integral converges, i.e.:

$$\int |F(\theta,\phi)|^2 d\Omega < \infty, \tag{4.5.2}$$

evaluated over the surface of a sphere can be expanded via Laplace series, i.e.:

$$F(\theta,\phi) = \sum_{l=0}^{\infty} \sum_{m=-l}^{l} F_l^m Y_l^m(\theta,\phi), \tag{4.5.3}$$

where the coefficients F_l^m are given by:

$$F_l^m = \oint F(\theta,\phi) Y_l^{m*}(\theta,\phi) d\Omega, \tag{4.5.4}$$

with $\int d\Omega = \int_0^{2\pi} \int_0^{\pi} \sin\theta d\theta d\phi$ for spherical coordinates.

Here, we decompose the velocity and magnetic fields following Krause and Rädler (1980). The idea is that a vector field $\boldsymbol{F}$ can be represented in terms of three scalar fields F_1, F_2 and F_3 that fulfil:

$$\boldsymbol{F} = \boldsymbol{r} \times \boldsymbol{\nabla} F_1 + \boldsymbol{r} F_2 + \boldsymbol{\nabla} F_3.$$

These three functions can be expanded using equation (4.5.3), where the coefficients ${F_1}_l^m$, ${F_2}_l^m$ and ${F_3}_l^m$ have to be found. This can be done assuming ${F_{1,2,3}}_l^{m*} = {F_{1,2,3}}_l^{-m}$, because $F_{1,2,3}$ should be real. Using the orthogonality relation:

$$\oint Y_l^m Y_\nu^{-\mu} d\Omega = \begin{cases} A_l^m & \text{if} \quad l = \nu \text{ and } m = \mu \\ 0 & \text{otherwise} \end{cases},$$

with:

$$A_l^m = \frac{4\pi(l+|m|)!}{(2n+1)(l-|m|)!}.$$

And the differential equation:

$$Y_l^m d\Omega + n(n+1)Y_l^m = 0.$$

Finally, we obtain:

$$F_{1_l}^m = -\frac{1}{n(n+1)A_l^m} \oint \boldsymbol{r} \cdot (\boldsymbol{\nabla} \times \boldsymbol{F}) Y_l^{-m} d\Omega.$$
$$F_{2_l}^m = \frac{1}{n(n+1)A_l^m} \oint \boldsymbol{r} \cdot \boldsymbol{\nabla} \times (\boldsymbol{\nabla} \times \boldsymbol{F}) Y_l^{-m} d\Omega.$$
$$F_{3_l}^m = -\frac{1}{n(n+1)A_l^m} \oint \boldsymbol{r} \cdot \boldsymbol{\nabla} \times (\boldsymbol{r} \times \boldsymbol{F}) Y_l^{-m} d\Omega.$$

These are the coefficients that are computed numerically. The contribution of $l = 0$ for the magnetic field was dropped due to the solenoidal condition.

For more information, see the Chapter 13 of Krause and Rädler (1980), and the Chapter about Legendre Functions of Arfken et al. (2013).

Now, using the coefficients F_l^m of the spherical harmonic decomposition, we can compute the corresponding power spectra as follows:

$$E(\ell) \propto \sum_{m=-l}^{l} |F_l^m|^2. \tag{4.5.5}$$

We computed the power spectra from $l = 1$ to $l_{\max} = 50$, because this is enough to capture all the relevant scales in the simulations.

The power spectra of the velocity and the magnetic field at $r = 0.98R$ from all simulations are shown in Figure 4.5.1.

All the runs have the peak of the horizontal magnetic field (the green dotted line) and the non-axisymmetric (dark green dashed line) magnetic field contribution at $l = 1$, which represents the largest possible scale, and then both decay at smaller scales. In group A, the maximum value of the radial magnetic field seems to move to larger scales as we increase the rotation, starting from $l = 4$ for Ar1, $l = 3$ for Ar2 and $l = 2$ for Ar3. However, Ar3* has this peak at $l = 4$, which might be a consequence of smaller diffusivities. The power spectra of the radial velocity moves to smaller scales as we increase the rotation of the star. Ar1 and Ar2 have their peak at $l = 9$ and $l = 11$ respectively, while Ar3 and Ar3* have this peak

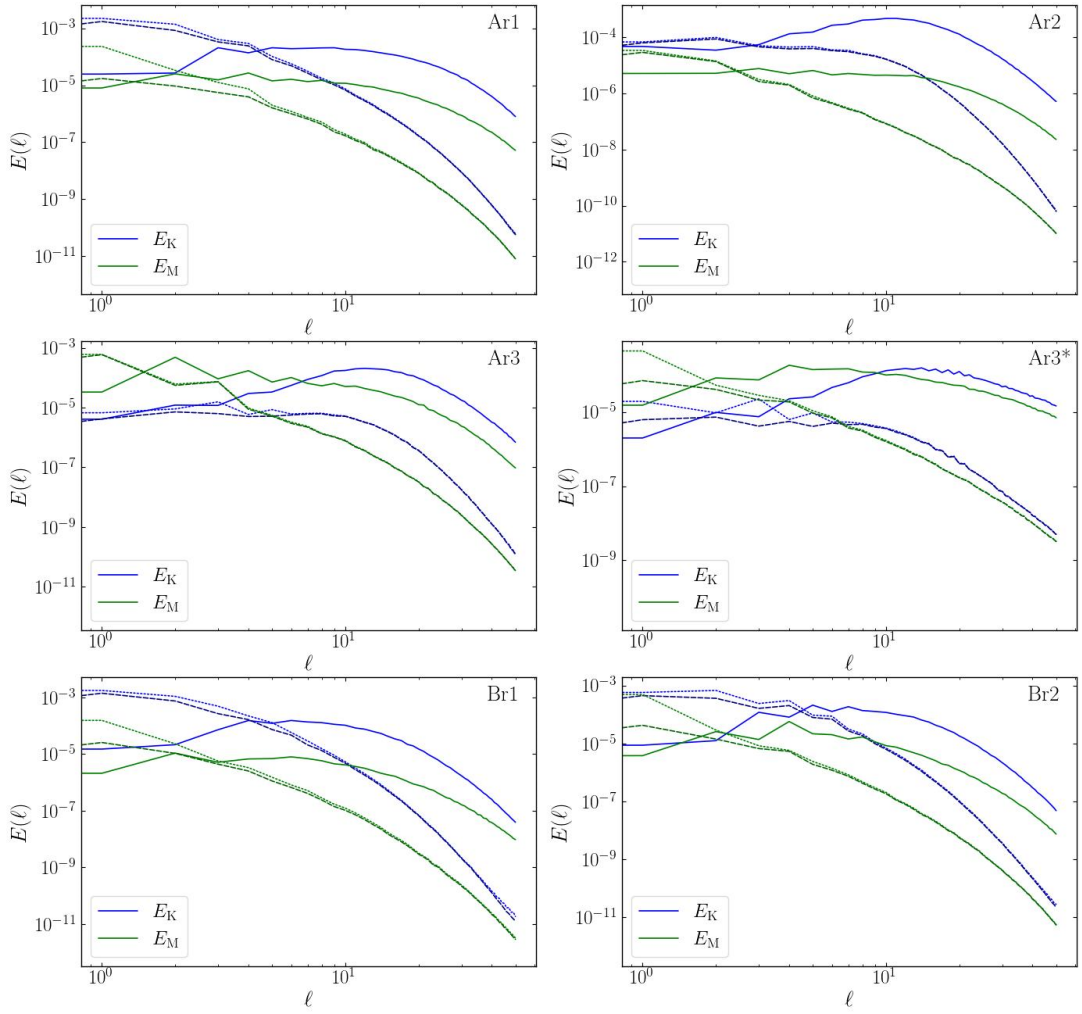

Figure 4.5.1: Power spectra of the velocity (E_K) and the magnetic field (E_M). The solid line represents the radial component, the dotted line the horizontal, and the dashed (slightly darker) line the non-axisymmetric contributions ($m \neq 0$).

at $l = 12$ and $l = 14$. From the middle panels of Figure 4.5.1 it is visible how the magnetic field dominates at bigger scales, and then it decays when the flow velocity rises at smaller scales. This is not visible in group B or in Ar1, where the horizontal velocity and its non-axisymmetric contributions have their peak at $l = 1$ (except for Br2, that has the horizontal peak at $l = 2$). Then, in group B the radial velocity gets its peak around $l = 5$, and in Br2 this peak is close to the peak of the radial magnetic field, which happens at $l = 4$, so both seem to operate at similar scales.

Chapter 5

Simulations of the dynamo driven by the convective core of the star: main-sequence phase

In this Chapter, the results of the convective core model described in Section 3.3.1 are presented. This includes a similar analysis as in Chapter 4, but now, most of the analysis is done not only at the surface of the star, but also at 20% of the stellar radius, where the convective core ends. This allows us to study how the core dynamo, differential rotation, and energies behave in this zone. As mentioned in Section 3.3.1, the group "MHD" models the whole star, while the group "zMHD" model the convective core and only a portion of the radiative envelope (see Section 3.3.2). In both cases, the analysis was made during the thermally and magnetically relaxed state of the simulations.

A publication presenting the results of this chapter is in preparation.

5.1 Simulations

This setup has a convection zone spanning 20% of the radial extent, i.e., in the core of the star. The heat conductivity coefficient $K = 0.1K_0$ leads to such configuration in the thermally relaxed state (see Figure 1 of Hidalgo et al. 2023). The diffusivities are given by $\nu = 5.45 \cdot 10^7$ [m^2/s], $\eta = 7.78 \cdot 10^7$ [m^2/s], and $\chi_{\rm SGS} = 2.61 \cdot 10^8$ [m^2/s] in the core, and therefore $\mathrm{Pr_M} = 0.7$ and $\mathrm{Pr_{SGS}} \approx 0.21$.

However, ν and η have radial jumps around $0.35R$, with a smooth transition over a width of $0.06R$. Above such jump, diffusivities are 10^2 times smaller, as a way to avoid the spreading of flows and magnetic fields into the radiative envelope. The runs indicated by * (the group MHD*) also have this profile, but the jump is at $0.3R$ and the width is $0.03R$. Runs in this group start already from saturated snapshots of the respective simulation with the same rotation rate in the MHD group. The runs, as well as the diagnostic quantities (computed from the time series), are listed in Table 5.1.1. All simulations were run on a grid of 200^3.

Table 5.1.1: Summary of all the "main-sequence" model runs. From left to right the columns correspond to the rotation period $P_{\rm rot} = 2\pi/\Omega_0$, the volume-averaged (over the convective zone) root-mean-square flow velocity $\langle u_{\rm rms}\rangle$, the volume-averaged root-mean-square magnetic field $\langle B_{\rm rms}\rangle$, the Coriolis number, the SGS Péclet number, the fluid and magnetic Reynolds numbers.

Run	$P_{\rm rot}$ [days]	$\langle u_{\rm rms}\rangle$ [m/s]	$\langle B_{\rm rms}\rangle$ [kG]	Co	Pe	Re	$\mathrm{Re_M}$
MHDr1	20	179	no dynamo	1.8	31	146	102
MHDr2	15	82	113	5.3	14	67	47
MHDr2*	15	80	114	5.4	14	65	46
MHDr3	10	62	111	10.4	11	51	36
MHDr3*	10	61	122	10.7	10	50	35
MHDr4	8	56	110	14.4	10	46	32
MHDr4*	8	56	103	14.5	10	46	32
zMHDr1	20	138	no dynamo	2.3	24	113	79
zMHDr2	15	77	97	5.6	13	63	44

5.1.1 Root-mean-square magnetic fields

In Figure 5.1.1 the temporal evolution of the volume-averaged (over the convective zone) root-mean-square magnetic field $B_{\rm rms}$ from three simulations corresponding to the MHD group is shown.

For MHDr2, the period between roughly 7 and 23 years corresponds to the kinematic phase, where the magnetic fields grow exponentially, and after 23 years we have the relaxed phase, where the magnetic field saturates. The faster rotators MHDr3 and MHDr4, have shorter kinematic phases. However, MHDr4 starts this phase almost at the same time as MHDr2, while for MHDr3 this happens a few years before.

From Table 5.1.1, it is visible that all simulations have very similar $\langle B_{\rm rms}\rangle$. It is

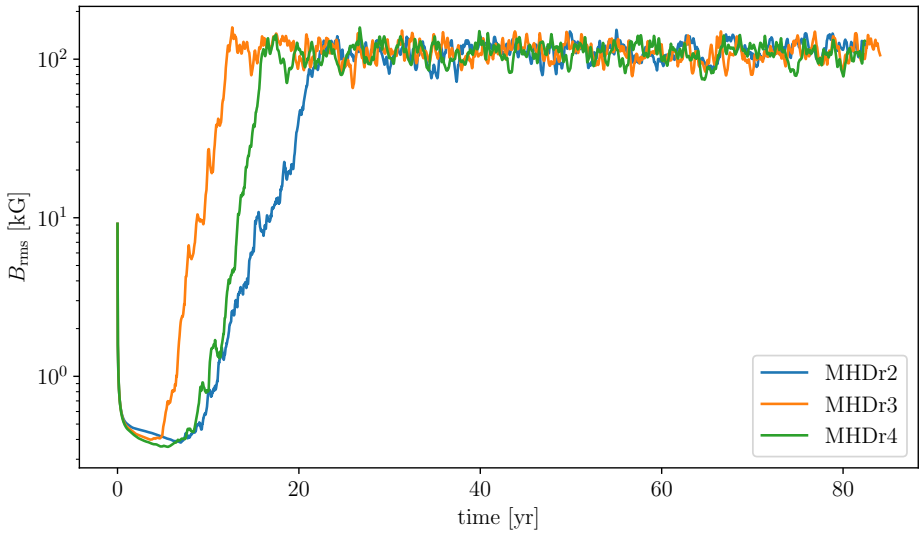

Figure 5.1.1: Time evolution of the volume-averaged root-mean-square magnetic field from the runs in MHD group that generate core dynamos.

worth mentioning that all runs from groups MHD and MHD* have maximum $B_{\rm rms}$ values around ~ 160 kG, where the highest is given by MHDr3* with 169 kG.

5.1.2 Stratification

The density and entropy profiles of three of the "whole star" simulations are shown in Figure 5.1.2. More specifically, we choose the run with no dynamo, and the slowest rotators from groups MHD and MHD*. The density stratification between the center and the surface of the star is $\overline{\rho}_{\rm center}/\overline{\rho}_{\rm surface} \approx 13$ in all runs. From the lower panel of Figure 5.1.2, we can infer an entropy gradient close to zero from $r = 0$ to $r \approx 0.5 R_\odot$ and a positive gradient at the rest of the radius, which is the expected configuration for a A-type main-sequence star. Furthermore, the stratification between the center and the surface of the convective core is given by $\overline{\rho}_{\rm center}/\overline{\rho}_{\rm surfcore} \approx 1.3$ in all simulations.

The temperature profiles of the same simulations are shown in Figure 5.1.3. The same physical units as in Chapter 4 are used here. The ratio between the averaged temperature in the core and at the surface of the star is given by $\overline{T}_{\rm center}/\overline{T}_{\rm surface} \approx 2$, while the ratio between the value of the center and the surface of the convective core is given by $\overline{T}_{\rm center}/\overline{T}_{\rm surfcore} \approx 1.25$.

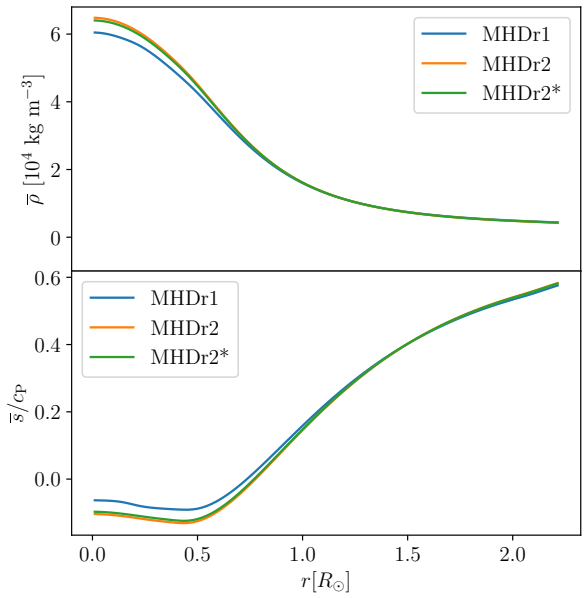

Figure 5.1.2: *Top panel*: Density profile from the slowest rotating run (with no dynamo), and the magnetic slowest rotators. *Lower panel*: Entropy profiles from the same runs. Both quantities are time-averaged over the thermally relaxed phase.

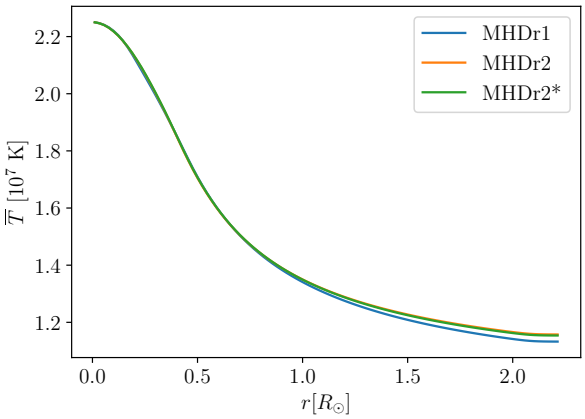

Figure 5.1.3: Temperature profile from same runs as in Figure 5.1.2. $\overline{T}$ is averaged over the thermally relaxed phase.

The density, entropy, and temperature profiles for both runs from group zMHD are shown in Figure 5.1.4. The density ratio between the center of the star and the outer edge of the radiative zone inside our domain is $\overline{\rho}_{\text{center}}/\overline{\rho}_{\text{edge}} \approx 4.15$ for both runs, and $\overline{\rho}_{\text{center}}/\overline{\rho}_{\text{surfcore}} \approx 1.27$, similar to the value obtained from group MHD. Finally, the ratio between the temperature at the center and at the edge of our domain is given by $\overline{T}_{\text{center}}/\overline{T}_{\text{edge}} \approx 1.6$, while $\overline{T}_{\text{center}}/\overline{T}_{\text{surfcore}} \approx 1.22$ in both

runs, again, similar to group MHD.

.

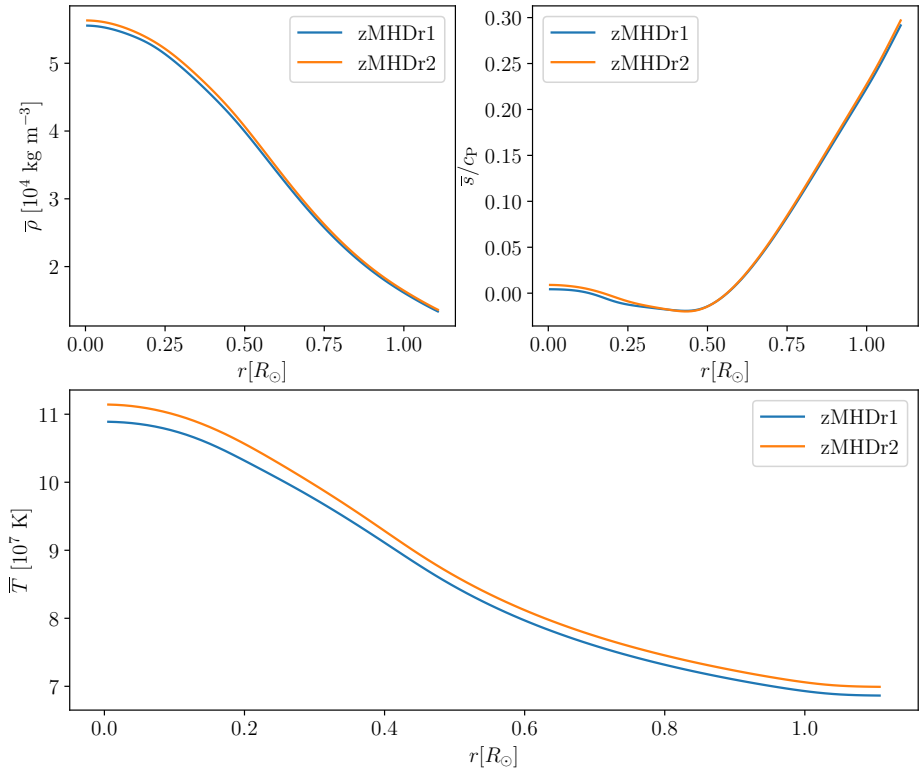

Figure 5.1.4: Density, entropy (*upper panel*) and temperature (*lower panel*) profiles from the simulations from group zMHD. All the quantities are averaged over the thermally relaxed phase.

5.2 Dynamo solutions

Run MHDr1 did not generate a dynamo. This is likely an issue related to too low resolution. However, its counterpart zMHDr1 has a growing magnetic field, but in practical effects it is not relevant in this study. This is because after the magnetic field seed decayed to its lowest value, it began to be amplified with a growth rate close to marginal, therefore, it never saturated. During the whole running time the $B_{\rm rms}$ increased 0.01 kG, which is still 100 smaller than the initial $B_{\rm rms}$ of the seed field. It is worth mentioning that this slow increasing field was not seen in MHDr1 at all. Here, the magnetic field only decayed.

All the remaining runs in all groups act as dynamos. In this section the azimuthally

averaged toroidal magnetic field $\overline{B}_\phi(r, \theta, t)$ was analyzed at two different radii. First at $r = 0.2R$, in order to have a better understanding of the magnetic field generated in the core. And then at $r = R$, same as in Chapter 4, as a way to study the magnetic field at the surface of the star.

5.2.1 Dynamos driven in the core

The azimuthally averaged toroidal magnetic field at $r = 0.2R$ as a function of time and latitude for the runs in group MHD is shown in Figure 5.2.1. It is clearly visible that all the generated magnetic fields are cyclic and hemispheric. MHDr2 and MHDr3 are similar, and the magnetic field is concentrated in the southern hemisphere, however, the sign reversals of MHDr2 seem to happen faster than in MHDr3, for example, in MHDr2 there are many reversals between 60 and 70 years, while in MHDr3 there are fewer inside this same range of time. This behavior is related with the magnetic cycle period of the dynamo and it is discussed in Section 5.4.

All these core dynamos have roughly the same field strength, as we can see in Table 5.2.1. These $\overline{B}_\phi$ values have the same order of magnitude as in the fully convective runs.

The azimuthally averaged toroidal magnetic field at $r = 0.2R$ for group MHD* is shown in Figure 5.2.2. The generated magnetic fields are again hemispheric. In MHDr2*, the magnetic field is concentrated in the southern hemisphere, same as in MHDr2, but then it moves to the northern hemisphere. This is a unique behavior in these runs and it is unclear why it is happening. This kind of behavior was also found by Brown et al. (2020), in spherical simulations of fully convective M dwarfs, with no conclusive reason either. However, in Brown et al. (2020) the run continued as a northern-hemisphere dynamo during the rest of the simulated time (see their Fig. 1). It is unclear if MHDr2* will follow this pattern or not, as more running time is required to make a proper comparison between both runs. Interestingly, this run is the only one that has higher maximum and minimum $\overline{B}_\phi$ values compared to their counterpart in the MHD group, but the root-mean-square $\overline{B}_\phi^{\rm rms}$ is slightly smaller than in MHDr2 (see Table 5.2.1). MHDr3* is very similar to MHDr3, a dynamo operating in the southern hemisphere, the main difference is that its maximum, mean, and minimum values differ. MHDr4* seems to have a cyclic dynamo acting in both hemispheres, during the early part of

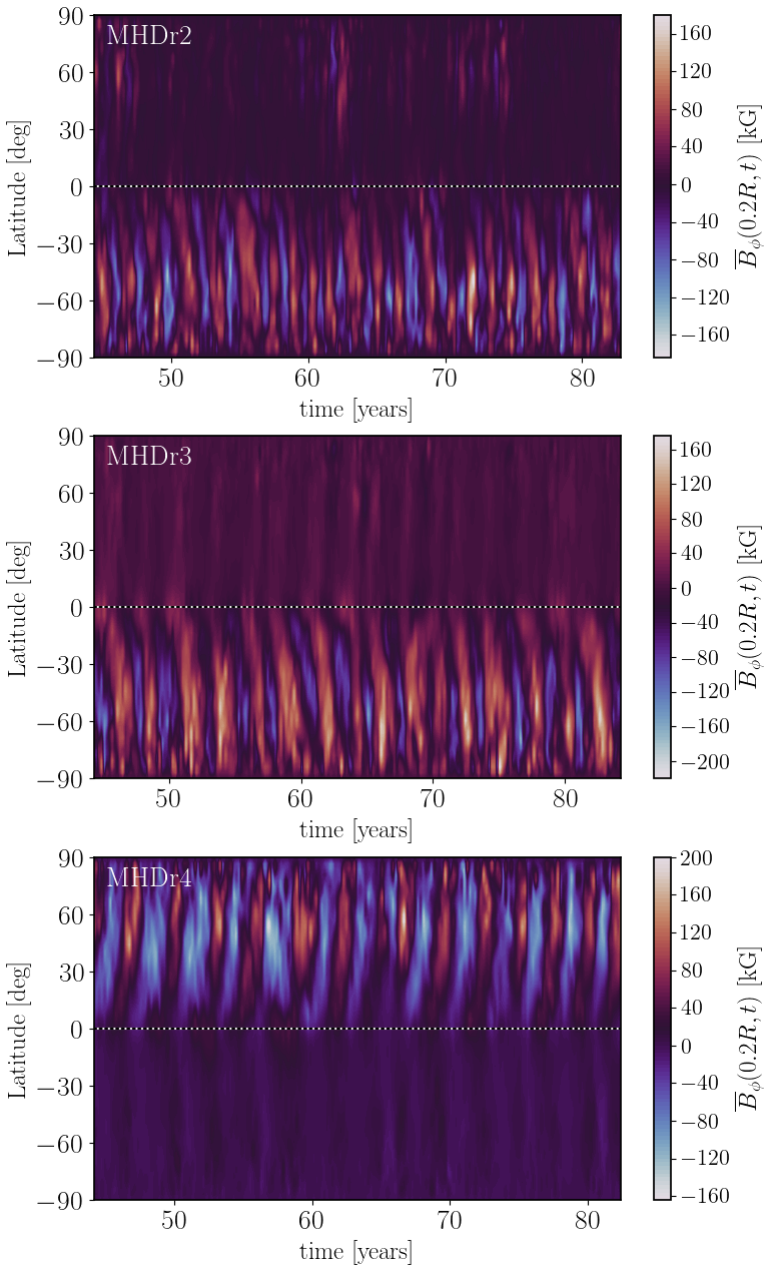

Figure 5.2.1: Time-latitude diagrams of the azimuthally averaged toroidal magnetic field $\overline{B}_\phi(r = 0.2R, \theta, t)$ of the MHD group, where the run is indicated in the upper left of each plot.

the simulation. But then, the activity in the southern hemisphere vanishes, and the resulting magnetic field is similar to MHDr4, but with slightly smaller values for the maximum, mean, and minimum. Something similar was found by Brown et al. (2020), where their hemispheric dynamos are initially symmetric on both hemispheres, but after some time strong southern-hemisphere fields replace the original symmetric configuration.

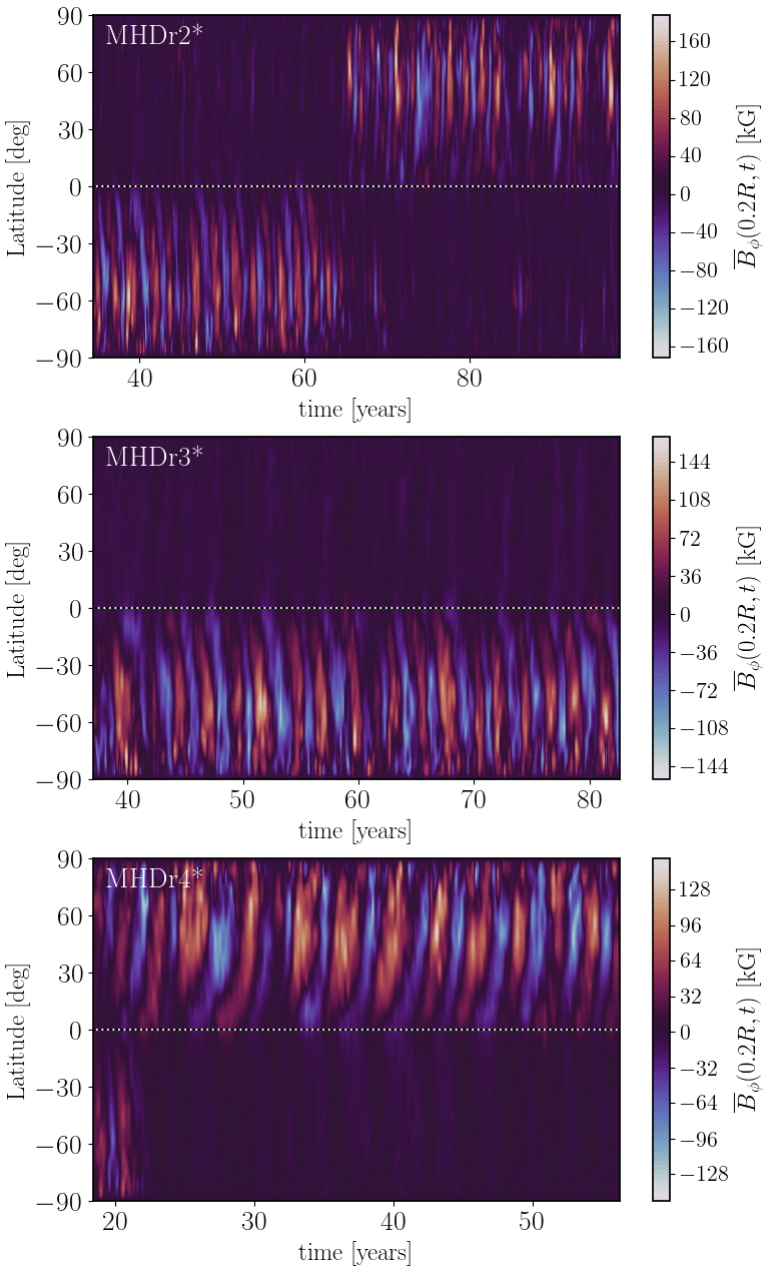

Figure 5.2.2: Time-latitude diagrams of the azimuthally averaged toroidal magnetic field $\overline{B}_\phi(r = 0.2R, \theta, t)$ of the MHD* group, where the run is indicated in the upper left of each plot.

Finally, the azimuthally averaged toroidal magnetic field at the surface of the convective core for zMHDr2 is shown in Figure 5.2.3. In principle, it is very similar to its counterpart in the MHD group, showing a dynamo in the southern hemisphere. However, roughly between 75 and 85 years, it exhibits some activity in the northern hemisphere as well, which seems to slightly reduce the activity in the southern hemisphere. This behavior is also visible in MHDr2 more frequently

Table 5.2.1: Maximum, root-mean-square, and minimum value of the averaged toroidal magnetic field at $r = 0.2R$ from groups MHD, MHD* and zMHD.

Run	$\overline{B}_\phi^{\min}$ [kG]	$\overline{B}_\phi^{\text{rms}}$ [kG]	$\overline{B}_\phi^{\max}$ [kG]
MHDr2	-182.1	31.6	178.0
MHDr3	-216.9	35.2	175.7
MHDr4	-162.0	35.8	197.9
MHDr2*	-171.7	30.0	185.0
MHDr3*	-152.5	29.2	164.7
MHDr4*	-150.7	31.8	152.4
zMHDr2	-182	26.3	179.5

though not very prominent. As we can see from Table 5.2.1, the maximum and minimum values from both runs are basically the same. The root-mean-square values are slightly different, although it is not a big difference. Therefore, we can conclude that at least in terms of the toroidal magnetic field, there are no major differences between the zoom and the whole star models.

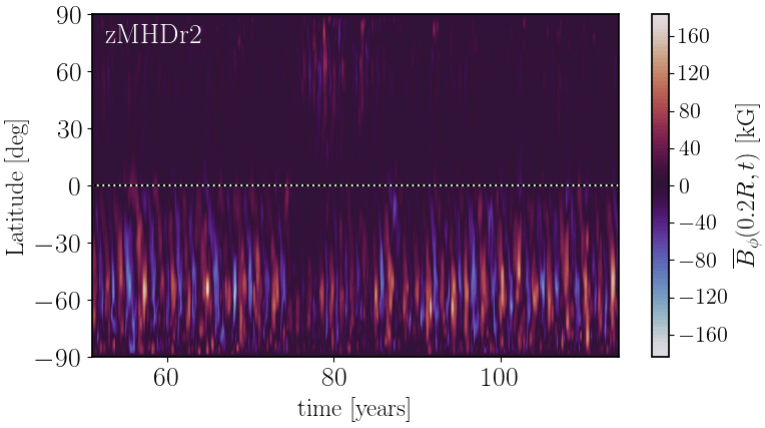

Figure 5.2.3: Time-latitude diagrams of the azimuthally averaged toroidal magnetic field $\overline{B}_\phi(r = 0.2R, t)$ from run zMHDr2.

5.2.2 Surface magnetic fields

As expected, and as we briefly discussed in Section 1.3.1, the magnetic field generated by a core dynamo is unable to create large-scale structures that reach the surface of the star. This is something that we can see in Figure 5.2.4, where the time-latitude diagrams of the averaged toroidal magnetic field at $r = R$ from some of the runs are shown. In the two leftmost panels, we have the surface fields from MHDr2 and MHDr3. The field is nearly zero on almost the whole surface

of the star, except at the poles, where the highest amplitudes appear in MHDr4, with ~ 0.3 kG, and an absolute minimum of -3.8 kG. This magnetic field in the poles is probably being transported by the vertical flows generated in these runs, given by the high Coriolis numbers in these simulations (see Section 5.3). The surface field of MHDr3 is not shown, because it is very similar to that of MHDr2 and it does not add relevant information to this analysis.

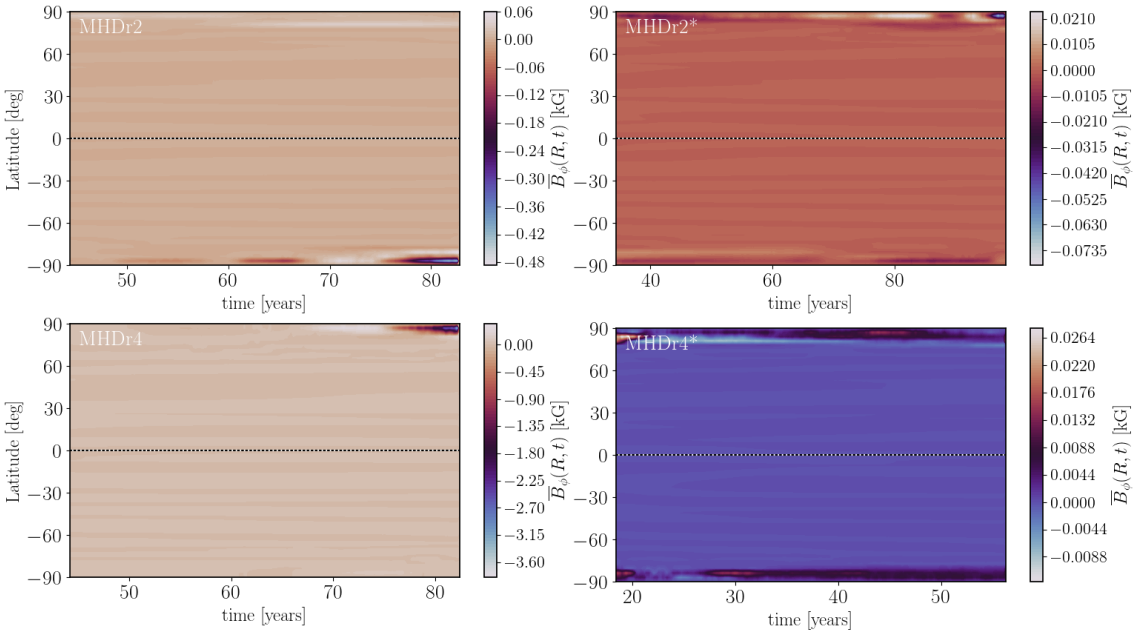

Figure 5.2.4: Time-latitude diagrams of the azimuthally averaged toroidal magnetic field $\overline{B}_\phi(r = R, \theta, t)$ of the groups MHD (*left*) and MHD* (*right*), where the run is indicated in the upper left of each plot.

In the right panels of Figure 5.2.4 we have the toroidal surface fields from MHDr2* and MHDr4*. In these runs, we have a similar result to the MHD group. The magnetic field is almost zero everywhere at the surface except near the poles. However, changing the radial profile of the diffusivities seems to reduce the magnetic fields at the surface significantly. This is clearly visible in the colorbar from these plots, where the maximum and minimum values do not have an amplitude greater than 0.0 kG, and this $\overline{B}_\phi \sim 0$ kG behavior is more intense in the fast rotator MHDr4*. Again, the run MHDr3* was not included because its surface magnetic field is very similar to that of MHDr2*.

5.3 Large-scale flows

In Chapter 4 we studied the large-scale flows using the averaged rotation rate given by equation (4.3.1). Here, we use the same approach but with a reduced domain, showing the star up to $r = 1R_\odot$. This is to analyze better the motions inside the convective zone. Moreover, as we can see from Figure 5.3.1, the radiative zones in these models have $\overline{\Omega}(\varpi, z) \sim \Omega_0$, and thus, showing the whole star does not add relevant information to the analysis.

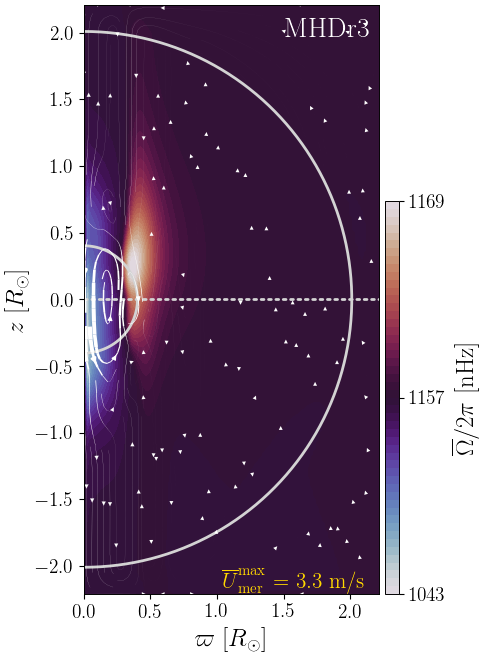

Figure 5.3.1: Profile of the temporally and azimuthally averaged rotation rate $\overline{\Omega}(\varpi, z)$ for MHDr3 in the whole star.

Differential rotation was studied using the differential rotation parameters (4.3.3). However, it is relevant to also analyze the rotation of the convective core, as it has been reported to have differential rotation in previous studies (Browning et al., 2004). Therefore, we introduced the following quantities:

$$\Delta_\Omega^{\mathrm{CZ}(r)} = \frac{\overline{\Omega}(r_{\rm CZ}, \theta_{\rm eq}) - \overline{\Omega}(r_{\rm bot}, \theta_{\rm eq})}{\overline{\Omega}(r_{\rm CZ}, \theta_{\rm eq})}, \quad \Delta_\Omega^{\mathrm{CZ}(\bar{\theta})} = \frac{\overline{\Omega}(r_{\rm CZ}, \theta_{\rm eq}) - \overline{\Omega}(r_{\rm CZ}, \bar{\theta})}{\overline{\Omega}(r_{\rm CZ}, \theta_{\rm eq})}. \quad (5.3.1)$$

These are the equivalent to the parameters (4.3.3), but $r_{\rm CZ} = 0.2R$ is the outer radius of the convective core. Also, here $r_{\rm bot}$ was slightly decreased to $\sim 0.05R$

due to the coarse grid inside the core. The definition of $\theta_{\rm eq}$ and $\overline{\theta}$ remain the same as before. Both parameters, (4.3.3) and (5.3.1), are summarized in Table 5.3.1.

Table 5.3.1: Differential rotation parameters for all simulations, obtained from the averaged (azimuthally and temporally) angular velocity $\overline{\Omega}(r,\theta)$.

Run	$\Delta_\Omega^{\mathrm{CZ}(r)}$	$\Delta_\Omega^{\mathrm{CZ}\overline{\theta}}(60°)$	$\Delta_\Omega^{\mathrm{CZ}\overline{\theta}}(75°)$	$\Delta_\Omega^{(r)}$	$\Delta_\Omega^{\overline{\theta}}(60°)$	$\Delta_\Omega^{\overline{\theta}}(75°)$
MHDr1	0.3870	0.2785	0.4132	0.1539	-0.0002	-0.0018
MHDr2	0.1131	0.0699	0.1142	0.0505	-0.0001	-0.0006
MHDr2*	0.1101	0.0683	0.1133	0.0485	-0.0001	-0.0006
MHDr3	0.0538	0.0295	0.0484	0.0251	-0.0000	-0.0004
MHDr3*	0.0489	0.0283	0.0438	0.0224	-0.0001	-0.0006
MHDr4	0.0405	0.0213	0.0350	0.0197	-0.0000	-0.0003
MHDr4*	0.0387	0.0208	0.0333	0.0169	-0.0001	-0.0006
zMHDr1	0.3742	0.2442	0.3729	-	-	-
zMHDr2	0.1291	0.0739	0.1294	-	-	-

From columns 5,6 and 7 of Table 5.3.1, we can clearly see that the stellar surface rotates nearly as a rigid body, because $|\Delta_\Omega^{\overline{\theta}}|$ is $\sim 10^{-4}$ for both latitudes. This implies no difference between the averaged rotation at the chosen latitudes and the equator. This is similar of what happens with the Sun, whose radiative interior has approximately rigid rotation (see Howe 2009). $\Delta_\Omega^{(r)}$ has positive values, this is because the innermost part of the core is rotating slower than the stellar surface, as we can see in Figure 5.3.3. Columns 2,3, and 4, list the parameters related to the core. Positive values of $\Delta_\Omega^{\mathrm{CZ}\overline{\theta}}$ indicate that the convective core is rotating faster in the equator than in other latitudes, and therefore, we have a solar-like differential rotation in all the runs. This is also visible in Figure 5.3.2, and Figure 5.3.3.

In Figure 5.3.2, the averaged $\overline{\Omega}(\varpi, z)$ profiles for group MHD are shown. As already discussed, all the runs have solar-like differential rotation. Also, we can see vertical structures that are parallel to the axis of rotation, due to the Taylor-Proudman theorem. This is similar to what happened to fast rotators in Chapter 4, and to the fast rotator from Brun et al. 2005 (see their Fig. 9). However, these flows are not very prominent in a single snapshot. For example, in Figure 5.3.4 we show a snapshot of the radial component of the flow velocity from MHDr3. The vertical flows, although visible, do not stand out in the same way as the core motions. However, it seems that these flows influence the rotation profile of the star, and also, they are probably the reason why we have magnetic fields at the stellar surface, especially at the poles. The radial profiles of the viscosity

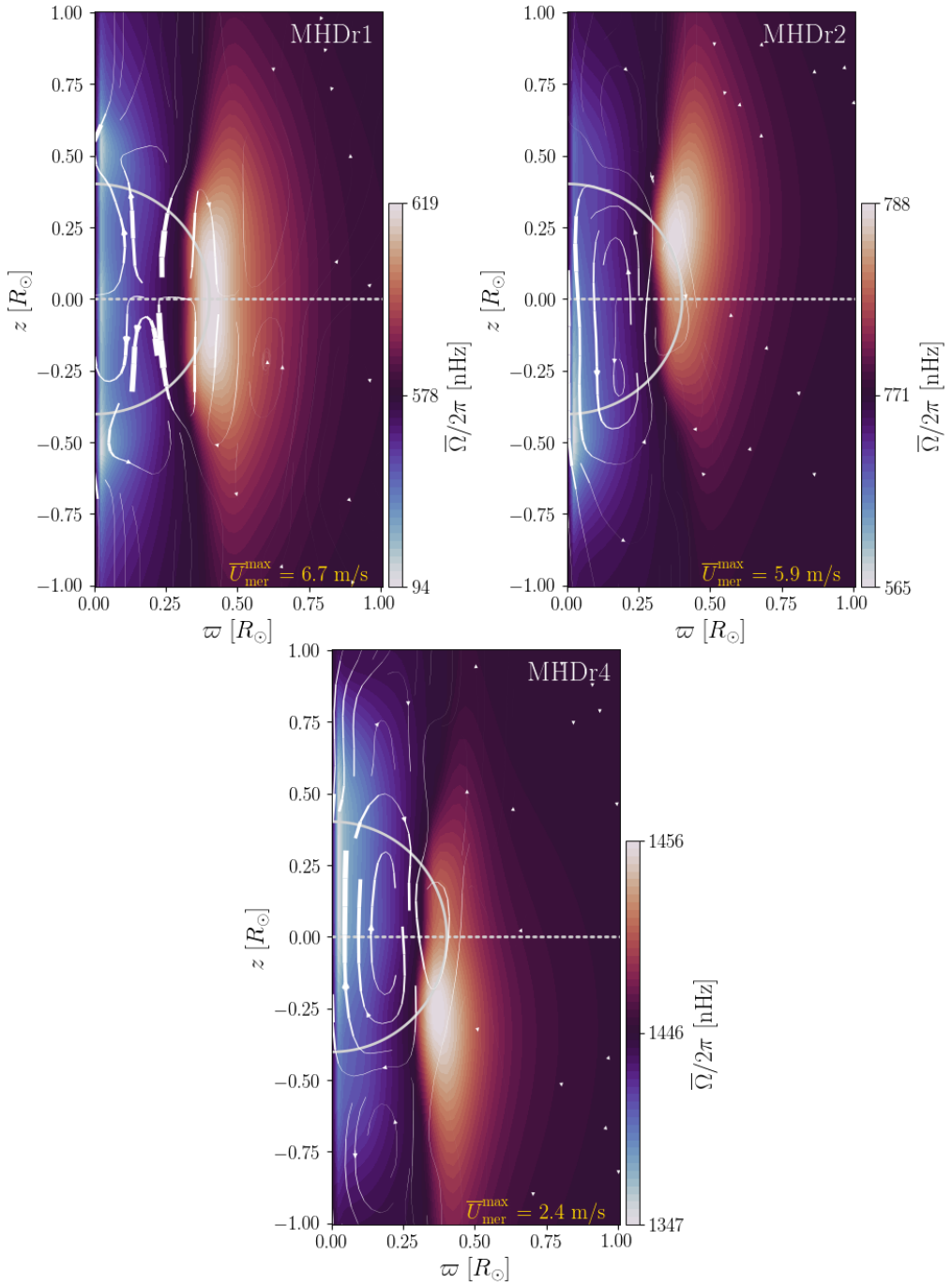

Figure 5.3.2: Profiles of the temporally and azimuthally averaged rotation rate $\overline{\Omega}(\varpi, z)$ for runs from the MHD group. The streamlines indicate the mass flux due to meridional circulation and the maximum averaged meridional flow is indicated in the lower left side of each plot. The dashed line represents the equator.

should reduce the intensity of these flows, but we are limited by the resolution, and the high rotation rates that we are exploring.

Notice that, MHDr1 in the left upper panel of Figure 5.3.2 is symmetric with

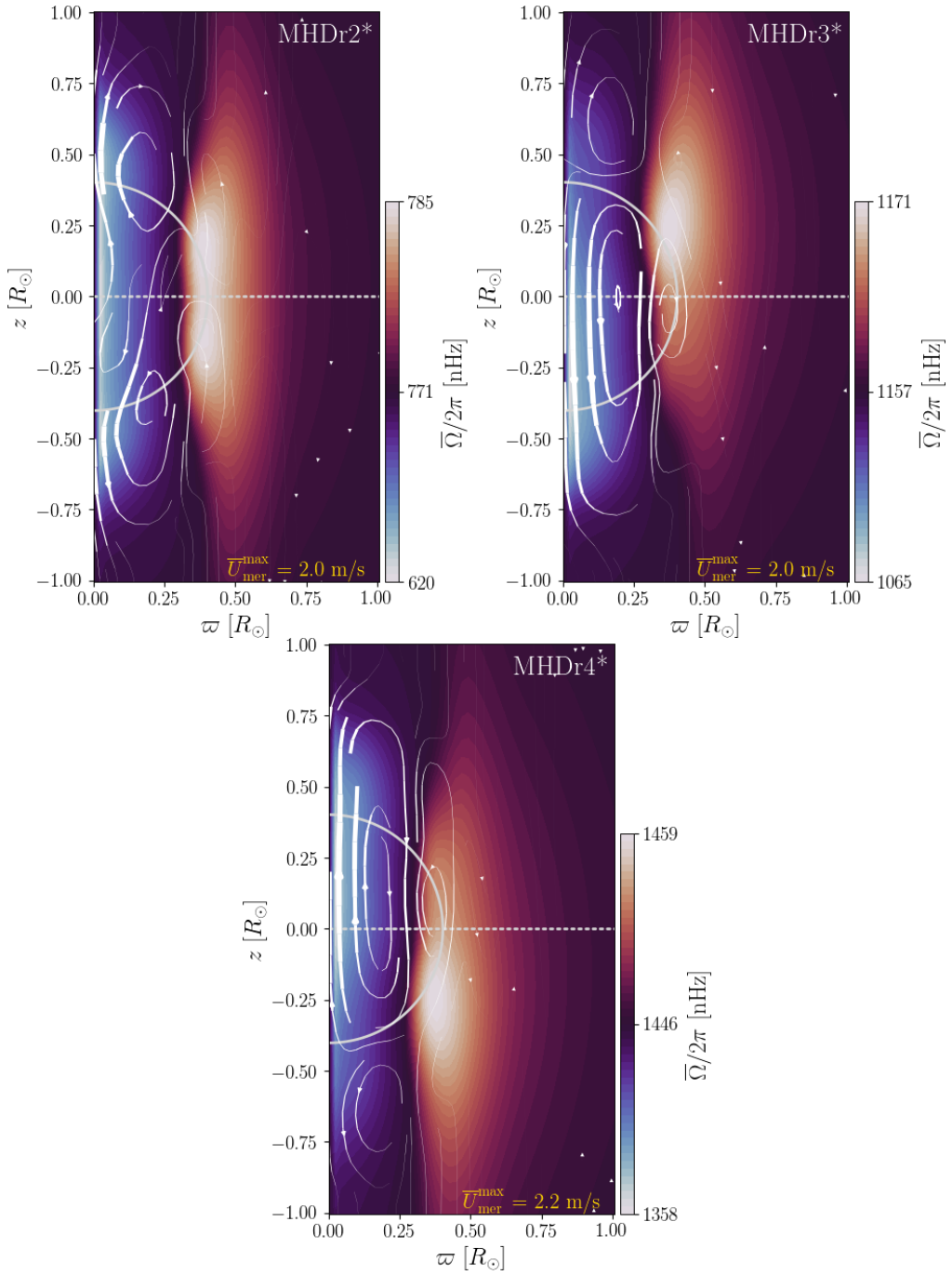

Figure 5.3.3: Profiles of the temporally and azimuthally averaged rotation rate $\overline{\Omega}(\varpi, z)$. Same as Figure 5.3.2 but for runs from the MHD* group.

respect to the equator. This is because this run does not have a core magnetic field. MHDr2 and MHDr3 are asymmetric with respect to the equator. This is because the hemispheric dynamos visible in Figure 5.2.1, are reducing the intensity of the differential rotation in the zone where they are located. In MHDr3 the same is happening, but the plot was not included because it is very similar to MHDr2,

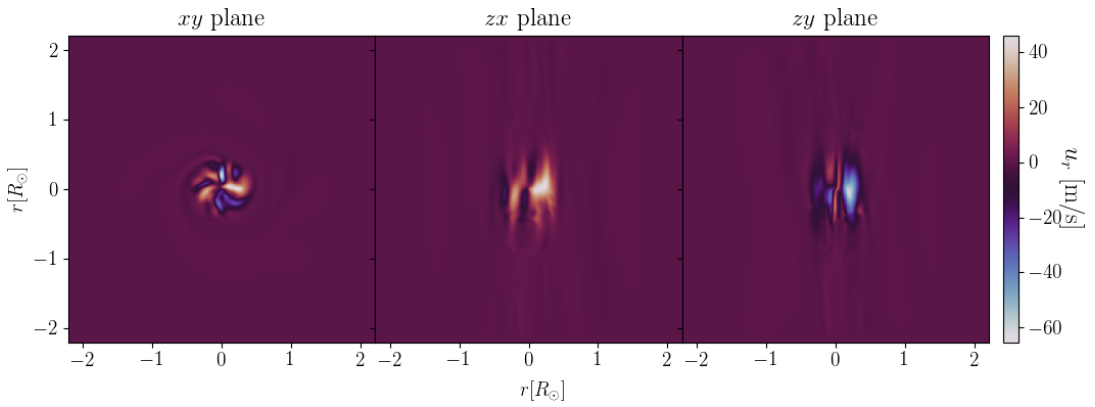

Figure 5.3.4: Snapshot from MHDr3 at $t = 82$ [yr]. The left plot corresponds to the equatorial plane, and the middle and right plots to the planes that contain the axis of rotation (zx and zy respectively). The colorbar represents the radial component of the flow velocity u_r.

but with a maximum and minimum of 1169 nHz and 1043 nHz respectively, as we can see in Figure 5.3.1.

For the MHD* group something similar happens, as can be seen from Figure 5.3.3. The rotation profile of MHDr2* looks very similar to that of MHDr1, even though this run has a core dynamo. This is probably because the magnetic field of this run starts in the southern hemisphere, quenching the differential rotation below the equator, but then, the magnetic field moves to the northern hemisphere, and the differential rotation is affected above the equator. What we observe in the plot is the result of an averaging over this process, because $\overline{\Omega}(\varpi, z)$ is temporally averaged during a period that include this behavior in the magnetic field. MHDr3* is very similar to MHDr3 and MHDr2, while MHDr4* is similar to MHDr4. The mass flux due to meridional circulation seems to be slightly different in both groups.

From Figure 5.3.5 we see that similarly to what happened with the toroidal magnetic field in the core of the star, the rotation profiles for the group zMHD are very similar to their MHD counterparts, with similar maximum and minimum values of $\overline{\Omega}/2\pi$, and slightly higher maximum values of the averaged meridional flow. However, in the zMHD set we can clearly distinguish more structures than in the MHD group. This is due to the increase of grid points inside the convective core, allowing to resolve flows on smaller scales. There seems to be a radius outside the convective core where all the streamlines stop moving parallel to the axis of rotation and change direction. This is a consequence of modifying the radius of

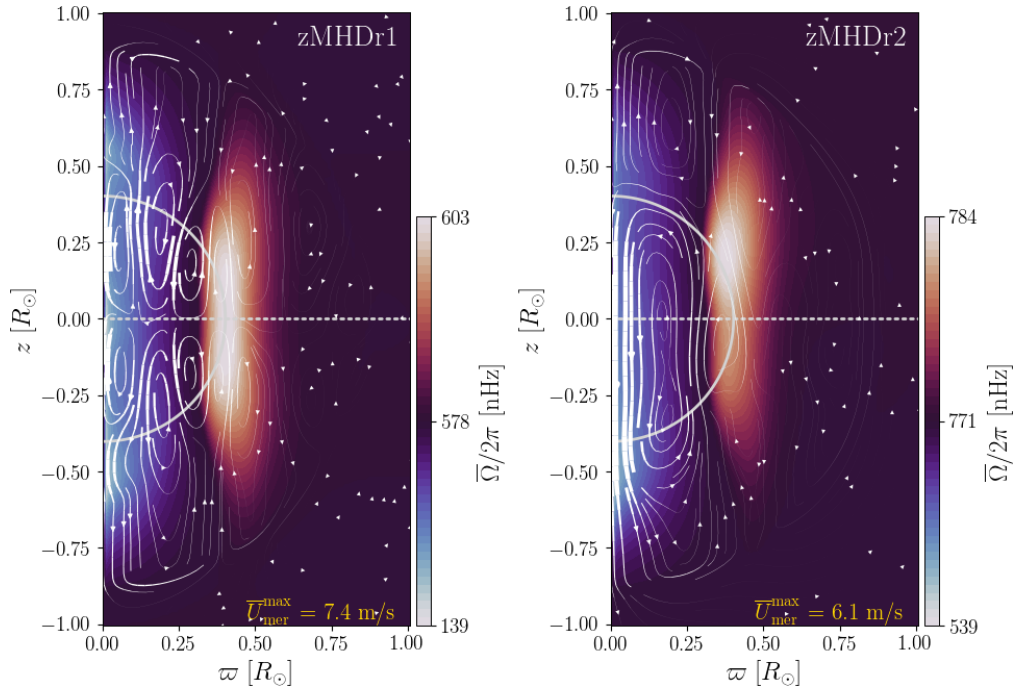

Figure 5.3.5: Profiles of the temporally and azimuthally averaged rotation rate $\overline{\Omega}(\varpi, z)$. Same as Figure 5.3.2 but for runs from the zMHD group.

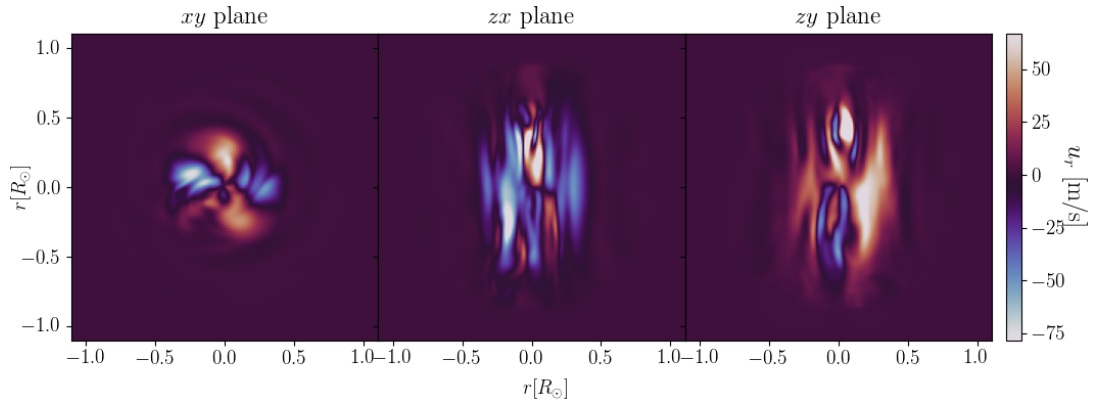

Figure 5.3.6: Snapshot from zMHDr2 at $t = 68$ [yr]. The left plot corresponds to the equatorial plane, and the middle and right plots to the planes that contain the axis of rotation (zx and zy respectively). The colorbar represents the radial component of the flow velocity u_r.

where the damping of flows starts. As we discussed in Section 3.3.2, we defined $r_{\rm damp} = 0.45R_* = 0.9R_\odot$ as a way to give stability to the model and also for convenience. Therefore, unlike the full model where $r_{\rm damp}$ starts near the surface, in the group zMHD it starts inside the radiative zone, vanishing the streamlines and the vertical flows. This is something clearly visible in Figure 5.3.6, which corresponds to a snapshot of zMHDr2 at $t = 68$ yr, showing the radial component

of the flow velocity analogously to Figure 5.3.4.

5.4 Rotational scaling of magnetic cycles

As discussed in Section 5.2.2, the magnetic field is nearly zero on almost the whole stellar surface, so here there is no magnetic cycle to analyze. However, the core does indeed exhibit cyclic magnetic fields. As a way to estimate the magnetic cycle period $P_{\rm cyc,c}$ of the core dynamo we computed the spectral density of an average of the magnetic field from the active hemisphere using the Welch's method (Welch, 1967). The peak value of this power spectrum corresponds to the frequency of the magnetic cycle.

Now, to obtain a consistent relation between the magnetic cycle and rotation periods, we have to compute the rotation period at the surface of the core. As discussed in Section 5.3, the convective core has differential rotation, so we take the average value of $\overline{\Omega}$ at $r = 0.2R$. The obtained values of $P_{\rm cyc,c}$ and $P_{\rm rot,c}$ are listed in Table 5.4.1.

Table 5.4.1: Magnetic cycle period $P_{\rm cyc,c}$, and the averaged rotation period $P_{\rm rot,c} = 2\pi/\overline{\Omega}$ at $r = 0.2R$.

Run	$P_{\rm cyc,c}$ [years]	$P_{\rm rot,c}$ [days]
MHDr2	1.43	15.45
MHDr3	2.36	10.12
MHDr4	3.21	8.07
MHDr2*	2.00	15.44
MHDr3*	2.58	10.09
MHDr4*	3.47	8.05
zMHDr2	1.95	15.58

The values of $P_{\rm rot,c}$ from the core do not differ significantly from $P_{\rm rot}$ shown in Table 5.1.1, that was computed directly using Ω_0, increasing $\sim 3.8\%$ in the most extreme case (zMHDr2). This is because, as seen in Section 5.3, the differential rotation of the core is not very strong, so $\overline{\Omega}(\varpi, z)$ does not differ very much from Ω_0.

There is a clear trend that $P_{\rm cyc,c}$ increases as $P_{\rm rot,c}$ decreases. This is visible in Figure 5.4.1. Furthermore, our best power-law fit shows $P_{\rm cyc,c} \propto P_{\rm rot,c}^{-1.26\pm0.06}$ in the MHD group, and $P_{\rm cyc,c} \propto P_{\rm rot,c}^{-0.87\pm0.20}$ in the MHD* group. The zMHD group

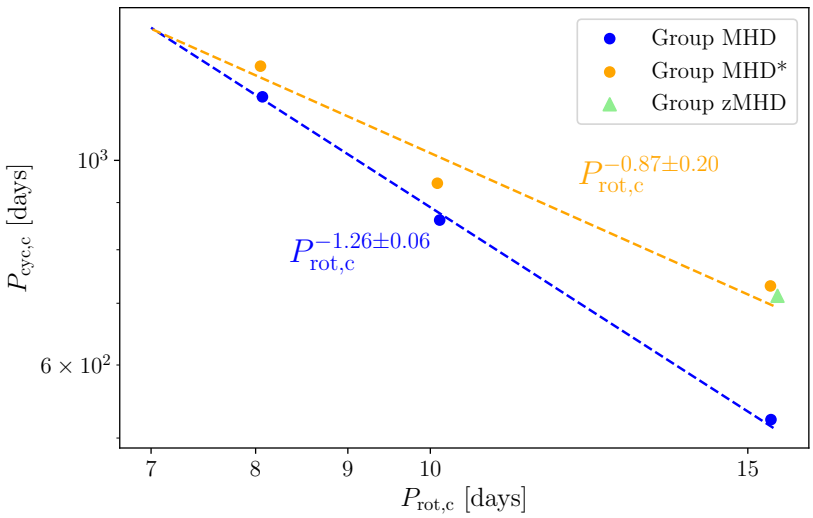

Figure 5.4.1: The magnetic cycle period $P_{\rm cyc,c}$ as a function of the averaged rotation period of the core $P_{\rm rot,c}$. The dashed lines are the best power-law fits to the data.

does not have enough data to do a fit. However, the periods of zMHDr2 are very similar to those of their MHD* counterpart, this is visible in Table 5.1.1 and in Figure 5.4.1. The relation between the magnetic cycle of the dynamo driven in the convective core and its rotation has not been studied before. However, simulations of solar-like stars have also shown a similar relation. Data from Warnecke (2018) indicate $P_{\rm cyc} \propto P_{\rm rot}^{-0.33\pm0.05}$ whereas data from Strugarek et al. (2018) indicate $P_{\rm cyc} \propto P_{\rm rot}^{-1.06}$.

In Figure 5.4.2, we show the ratio between the magnetic cycle period to the rotation period of the core as a function of the Coriolis number. Notice that although this relation is from the core of the star, we dropped the ",c" in the notation to avoid confusions in the comparison with other studies. We present a relation $P_{\rm rot}/P_{\rm cyc} \propto {\rm Co}^{\beta}$ in the core dynamo of an A-type star for the first time, with $\beta = -1.41 \pm 0.05$ for the MHD group, and $\beta = -1.11 \pm 0.12$ for the MHD* group. This has been found by other studies; simulations of a fully convective M dwarf from Ortiz-Rodríguez et al. (2023) report $\beta = -1.30 \pm 0.26$ and $\beta = -2.98 \pm 1.13$. Furthermore, data from simulations of solar-like stars from Warnecke (2018) and Strugarek et al. (2018) show $\beta = -0.99 \pm 0.05$ and $\beta = -1.58 \pm 0.11$ respectively, as visible in Figure 5.4.2. However, stellar observations suggest inactive and active branches with $\beta > 0$ (Brandenburg et al., 1998, 2017), which fits with the results reported by Guerrero et al. (2019) and Käpylä (2022). Nevertheless, the exact

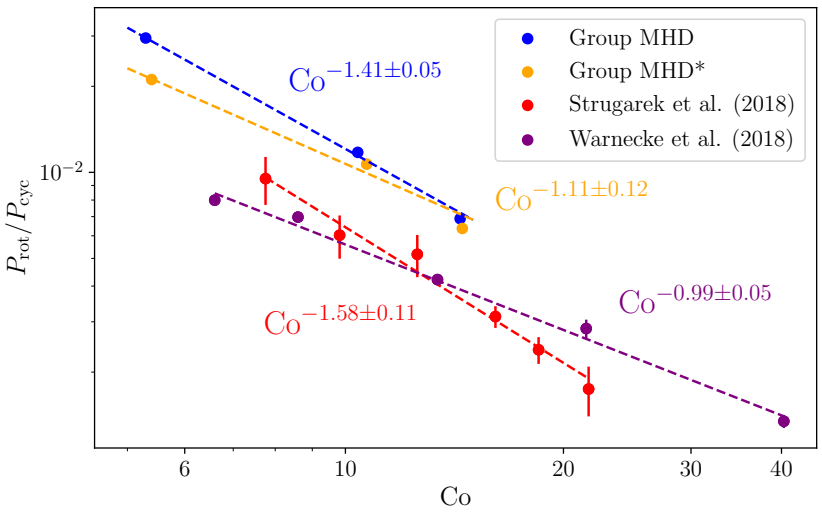

Figure 5.4.2: Ratios of rotation to cycle period as a function of the Coriolis number. Simulations from groups MHD and MHD* are indicated in blue and orange respectively. Additional data are from (Strugarek et al., 2018, red), and (Warnecke, 2018, purple). The dashed lines are the best power-law fits to the data.

nature of these branches is unclear.

5.5 Energy analysis

5.5.1 Global and core energies

Here we analyze the kinetic and magnetic energies from the simulations using the same expressions defined in Section 4.4. All the equations were defined using a volume average inside $r < R$. In this analysis, we compute the energies following this definition as a way to study them inside the whole star. However, to have representative values for the energies inside the convective core, we compute the same expressions averaged inside $r < 0.2R$. These values from all (magnetic) simulations are listed in Table 5.5.1.

Similarly to what happens in Chapter 4, the slowest rotators have the highest kinetic energies. In this set of simulations, all the differential rotation energies are very similar with $E_{\mathrm{kin}}^{\mathrm{DR}}/E_{\mathrm{kin}} \sim 0.3$. This is an expected result considering that in Section 5.3 we showed that all the runs have a similar rotation profile, i.e. a quasi-rigid radiative envelope and a differentially rotating convective core.

Table 5.5.1: Kinetic and magnetic energies, averaged over time and volume. The total kinetic and magnetic energies have units of 10^{33}J, while the rest of energies are written as fractions of these quantities.

Run	$E_{\rm kin}$	$E_{\rm kin}^{\rm DR}/E_{\rm kin}$	$E_{\rm kin}^{\rm MC}/E_{\rm kin}$	$E_{\rm mag}$	$E_{\rm mag}^{\rm tor}/E_{\rm mag}$	$E_{\rm mag}^{\rm pol}/E_{\rm mag}$
Whole star						
MHDr2	61.79	0.398	0.017	19.91	0.294	0.061
MHDr2*	61.95	0.391	0.018	20.49	0.277	0.059
MHDr3	35.43	0.323	0.011	19.62	0.226	0.077
MHDr3*	36.34	0.315	0.010	25.31	0.264	0.074
MHDr4	28.91	0.323	0.008	19.73	0.300	0.086
MHDr4*	29.73	0.317	0.006	22.04	0.266	0.069
Core						
MHDr2	6.88	0.349	0.026	1.30	0.136	0.100
MHDr2*	6.94	0.343	0.028	1.16	0.127	0.101
zMHDr2	7.02	0.375	0.035	0.89	0.131	0.096
MHDr3	3.99	0.297	0.017	1.53	0.143	0.111
MHDr3*	3.79	0.249	0.016	1.40	0.136	0.105
MHDr4	3.25	0.313	0.012	1.30	0.185	0.121
MHDr4*	3.06	0.261	0.009	1.19	0.168	0.110

The magnetic and kinetic energies considering the whole star are always larger in the group MHD* than in MHD. However, this behavior disappears after averaging the values over the core, as we can see in the final rows of Table 5.5.1. With $r < 0.2R$ the values of the magnetic energy in group MHD* are smaller than in group MHD, while the values of the kinetic energy, although quite close, do not seem to show any difference between groups. Similarly to the differential rotation energies, the toroidal magnetic energies are very similar, with values of $E_{\rm mag}^{\rm tor}/E_{\rm mag}$ between 0.226 and 0.3 for $r < R$, and between 0.127 and 0.185 for $r < 0.2R$. In both cases, the highest value is given by MHDr4, same as with the poloidal magnetic energy. This makes sense, because MHDr4 has the largest averaged toroidal magnetic field at the surface (~ 0.3 kG) and in the core with 197.9 kG; see Table 5.2.1. However, the maximum $E_{\rm mag}$ occurs in MHDr3* for the whole star, and in MHDr3 for the core.

There does not seem to be a big difference between the kinetic energies of MHDr2 and its zoom version zMHDr2 except in the meridional circulation energy, where the ratio $E_{\rm kin}^{\rm MC}/E_{\rm kin}$ is higher in zMHDr2. However, the total magnetic energy of zMHDr2 is lower, being the lowest in this set of simulations, while the values of the toroidal and poloidal energies from both simulations are close to each other.

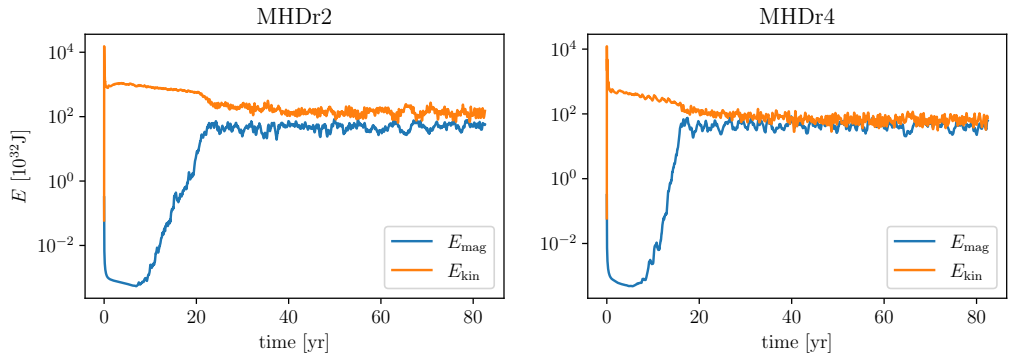

Figure 5.5.1: Temporal evolution of the magnetic (blue) and kinetic (orange) energies extracted from the time series of the runs MHDr2 (*left*) and MHDr4 (*right*).

Similarly to what happened in Chapter 4, the slow rotators have magnetic energies below equipartition. However, although still sub-equipartition, the values of the ratio $E_{\rm mag}/E_{\rm kin}$ are larger when considering the whole star instead of just the core. As the rotation rate increases, this ratio also gets closer to unity, with 0.741 for MHDr4*. This behavior is visible in Figure 5.5.1, where the total magnetic and kinetic energies are shown according to equations (4.4.1) with the variables given by the time series. In MHDr2, we can see that the magnetic energy has smaller values than the kinetic energy, while in MHDr4 the energies are closer to each other. This near equipartition regime was also found by Brun et al. (2005), and later in Featherstone et al. (2009). MHDr3 was not added to the figure, because (as expected from Table 5.5.1) it shows a behavior in between MHDr2 and MHDr4.

5.5.2 Energy fluxes and luminosities

The luminosities can be studied in terms of their respective energy flux. The luminosities related to the radiative, enthalpy, kinetic energy, viscosity, cooling and heating fluxes, are defined as (Käpylä, 2021):

$$\overline{L}_{\rm rad} = -4\pi r^2 \langle K \rangle_{\theta\phi t} \frac{\partial \langle T \rangle_{\theta\phi t}}{\partial r}, \qquad \overline{L}_{\rm enth} = 4\pi r^2 c_{\rm P} \langle (\rho u_r)' T' \rangle_{\theta\phi t},$$

$$\overline{L}_{\rm kin} = 2\pi r^2 \langle \rho \boldsymbol{u}^2 u_r \rangle_{\theta\phi t}, \qquad \overline{L}_{\rm visc} = -8\pi r^2 \nu \langle \rho u_i \boldsymbol{S}_{ir} \rangle_{\theta\phi t},$$

$$\overline{L}_{\rm cool} = -\int_0^r 4\pi r^2 \langle \mathcal{C} \rangle_{\theta\phi t} dr, \qquad \overline{L}_{\rm heat} = \int_0^r 4\pi r^2 \langle \mathcal{H} \rangle_{\theta\phi t} dr,$$

where the prime indicates fluctuations from the mean value, index r denotes the radial component, and $\langle . \rangle_{\theta\phi t}$ horizontal and temporal averaging. Notice that the total convective luminosity is given by $\overline{L}_{\rm conv} = \overline{L}_{\rm kin} + \overline{L}_{\rm enth}$.

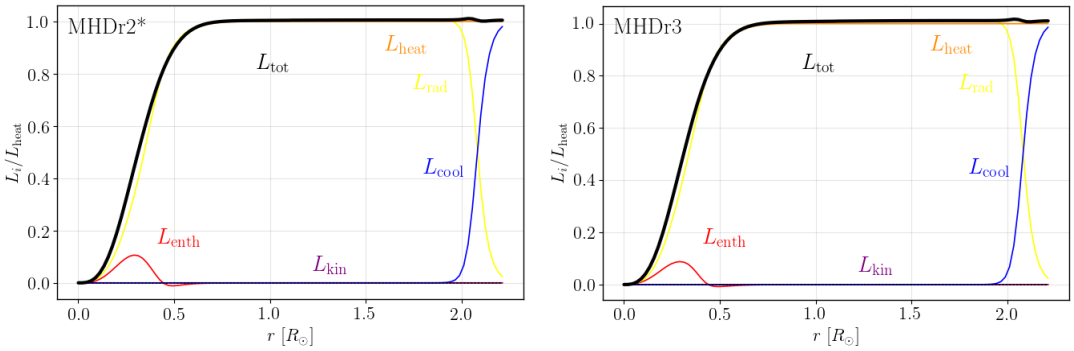

Figure 5.5.2: Luminosity contributions from kinetic energy, enthalpy, radiative, cooling and heating fluxes from MHDr2* (*left panel*) and MHDr3 (*right panel*).

The contributions to the total luminosity from runs MHDr3 and MHDr2* are shown in Figure 5.5.2. The luminosity due to the viscous energy flux is not included in the figure, because these values are negligible, reaching maximally 0.06% of the total flux at $r \approx 0.16 R_\odot$. The luminosity due to the enthalpy flux has its highest values from 0 to $\sim 0.5 R_\odot$. This is because, as we mentioned before, this luminosity is related to convection, and the convective core of the star has a radial extent up to roughly these values. In the majority of the star, the contribution due to the radiative energy flux dominates. This is also due to the internal structure of the star, where the main energy transfer mechanism is radiation (where the radiative zone is roughly 80% of the radial extent). However, near the surface of the star the cooling becomes effective and it starts to dominate the total luminosity. The rest of the runs from groups MHD and MHD* have almost the same luminosity profile, as we can already notice from MHDr2* and MHDr2, that have no significant differences. These profiles are similar to those of Augustson et al. (2016) and Brun et al. (2005), see their Fig. 3 and Fig. 13, respectively.

The luminosity contributions from runs zMHDr1 and zMHDr2 are shown in Figure 5.5.3. These profiles are also very similar to the ones shown in Figure 5.5.2, having a non-zero enthalpy flux where the convective core is, whereas the rest of the radius is dominated by the radiative energy flux. However, these profiles only show the radius up to $r \approx 1.1 R_\odot$, that is the domain of these simulations.

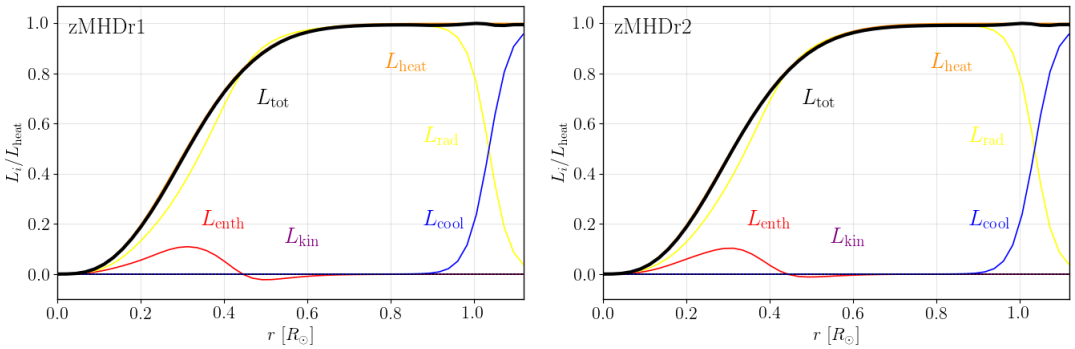

Figure 5.5.3: Luminosity contributions from zMHDr1 (*left panel*) and zMHDr2 (*right panel*).

Also, the cooling becomes effective already around $r \approx R_\odot$. This is an artificial consequence of modifying the starting point of the cooling inside the radiative zone, as the surface is no longer included (see Section 3.3.2).

5.6 Power Spectra

Following Section 4.5, the power spectra is computed using the coefficients of the Spherical harmonics decomposition, as described in equation (4.5.5), from $l = 1$ to $l_{\rm max} = 50$, because as in Chapter 4, this is enough to capture all the relevant scales in the simulations.

The power spectra of the velocity and the magnetic field at $r = 0.20R$ from all runs from groups MHD and MHD* are shown in Figure 5.6.1.

As can be seen from the first four plots, MHDr2, MHDr2*, MHDr3, and MHDr3* have the same peaks in the magnetic field spectra (E_M), more specifically, the radial magnetic field (solid green line) peaks at $l = 3$, and the horizontal (dotted green line) and non-axisymmetric (dashed dark green line) magnetic field contributions peak at $l = 1$, which is the largest possible scale. However, the power spectra of the velocity (E_K) from the mentioned runs is different. In MHDr2 all the contributions peak at $l = 3$, similarly to MHDr2* where this peak is also visible for the horizontal (dotted blue line) and non-axisymmetric (dashed dark blue) velocity contributions, while the radial velocity (solid blue line) peaks at $l = 4$. MHDr3* is very similar to MHDr2, sharing all the peaks except for the horizontal contribution, which peaks at $l = 1$. However, after this maximum value a secondary peak occurs at $l = 3$. In MHDr3 the situation is slightly different, with a radial peak at $l = 5$,

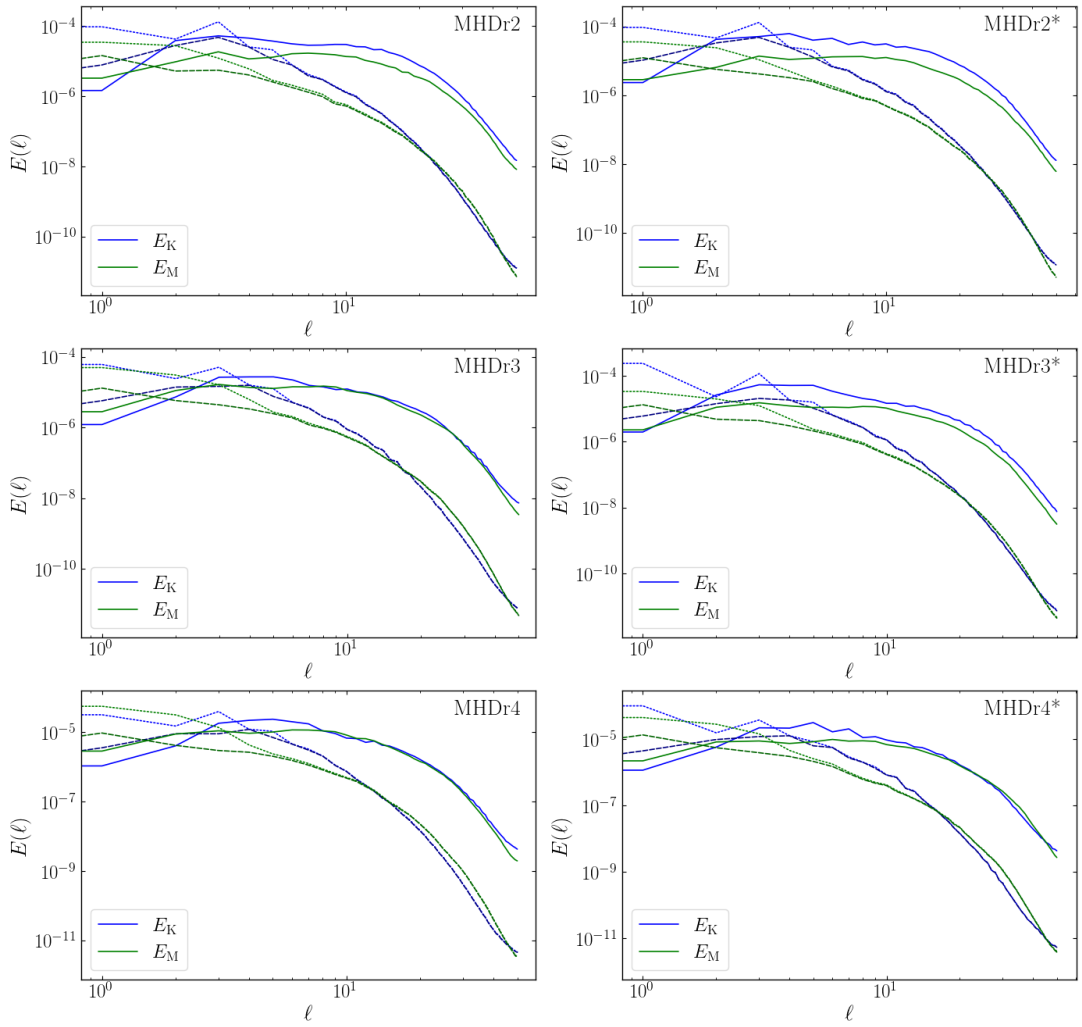

Figure 5.6.1: Power spectra of the velocity (E_K) and the magnetic field (E_M). The solid line represents the radial component, the dotted line the horizontal, and the dashed (slightly darker) line the non-axisymmetric contributions ($m \neq 0$).

and an horizontal and non-axisymmetric peaks at $l = 1$ and $l = 4$ respectively. Here, we also highlight that on small scales the radial velocity almost matches the radial magnetic field. In the rest of the mentioned plots, this behavior seems to happen with the non-axisymmetric contributions of the velocity and the magnetic field.

In the fast rotators MHDr4 and MHDr4*, the radial magnetic field has its peak at $l = 6$, and the horizontal and non-axisymmetric magnetic field contributions have their peaks at $l = 1$, similarly as earlier runs. Nevertheless, the peaks of the velocity of MHDr4* are exactly the same as MHDr3, and the only difference with MHDr4, is that in this run the horizontal velocity has its peak at $l = 3$, which

as discussed, is the second peak of MHDr3*, but also of MHDr3, and MHDr4*. Notice that in Chapter 4, the power spectra of the fast rotators have a clear scale difference, with the magnetic field appearing at large scales, and the velocity in small scales. In these runs that behavior is not so clearly visible, and both, magnetic field and velocity, seem to have similar scales, with almost the same values in small scales.

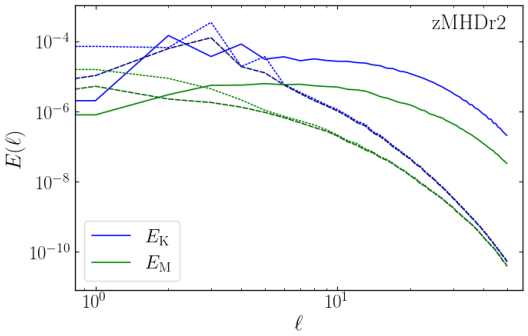

Figure 5.6.2: Same as Figure 5.6.1, but for run zMHDr2.

Finally, the power spectra of zMHDr2 is shown in Figure 5.6.2. This run is similar to its counterpart MHDr2, having the same peaks for the velocity contributions, except for the radial velocity which has its peak at $l = 2$. And the radial contribution of the magnetic field peaks at $l = 5$, while the horizontal and the non-axisymmetric contributions peak at $l = 1$, the largest scale, same as all of the previous runs.

Chapter 6

Summary and conclusions

The origin of the magnetism in Ap/Bp stars is a long-standing problem. In this thesis, we performed 3D magnetohydrodynamic simulations using the star-in-a-box model adapted from Käpylä (2021, 2022) as a way to understand possible explanations of the magnetism in these stars, solving the fully-compressible non-ideal MHD equations using The Pencil Code (Pencil Code Collaboration et al., 2021).

To model a star representative of the late pre-main-sequence evolution of an Ap star, we develop a setup of a 2 $M_\odot$ fully convective star (descending the Hayashi track). We explore rotation periods from 20 to 280 days, to study the protostellar phase of the star. We find strong toroidal magnetic fields, with maximum values in the range of $\sim 80 - 180$ kG, and root-mean-square magnetic fields in the range of $50 - 152$ kG. Also, we find mostly steady dynamo configurations with anti-solar differential rotation, similar to what has been found in low mass fully convective slowly rotating stars (Dobler et al., 2006; Käpylä, 2021; Ortiz-Rodríguez et al., 2023). These resulting magnetic fields could be potential inputs in our main-sequence model, as a way to test their stability inside the radiative envelope and study them as fossil fields. It is worth mentioning that no cyclic solutions are found. This could be a consequence of not exploring the intermediate rotation regime. In the A group there is a gap in the explored Coriolis numbers, jumping from 10 to ~ 30, while in the B group only slow rotation is explored.

We also develop a main-sequence model consisting of a 2 $M_\odot$ A-type star with a convective core covering 20% of its radial extent, surrounded by a radiative

envelope. Similar to the spherical simulations presented by Browning et al. (2004), Brun et al. (2005) and Featherstone et al. (2009), but using the star-in-a-box setup, including the stellar surface in our domain. Our main objective is to study and characterize the core dynamo of such stars, including the first quantitative analysis of the relation between magnetic activity cycle and rotation period. We explore rotation periods from 8 to 20 days, and did three different sets of simulations. First, the MHD and the MHD* groups, that differ in the radial profiles of the kinematic viscosity and the magnetic diffusivity. Both groups model the whole star as a way to study the magnetism from the core to the surface. We also develop the zMHD group, that is a zoom-in version of the MHD group, taking into account the core and a part of the radiative envelope at higher resolution. All the dynamos driven in the convective core of the star are hemispheric and have a cyclic behavior, with toroidal magnetic fields with maximum values in the range of 150 to 200 kG, with root-mean-squares $\overline{B}_{\phi}^{\rm rms}$ around ~ 30 kG. In MHDr2*, the magnetic activity migrated from the southern to the northern hemisphere. This behavior was reported by Brown et al. (2020) in fully convective M drawfs, and the reason behind it is not clear. There is some magnetic activity at the surface of the star. However, it is weak everywhere except at the poles, where the maximum value is in MHDr4 with ~ 0.3 kG. In the group MHD* the surface magnetic fields are even weaker, and none of the maximum values is higher than 0.02 kG, which seems to indicate the relevance of the radial profiles of diffusivities in the simulations. These weak magnetic fields might be transported from the core to the surface by the vertical flows produced by the Taylor-Proudman theorem, due to the high Coriolis numbers in our simulations.

We find that at the surface of the convective core the magnetic cycle period is related to the rotation period as $P_{\rm cyc} \propto P_{\rm rot}^{-1.26\pm0.06}$ for the MHD group, and $P_{\rm cyc} \propto P_{\rm rot}^{-0.87\pm0.20}$ for the MHD* group. Furthermore, we found a scaling of $P_{\rm rot}/P_{\rm cyc} \propto {\rm Co}^{\beta}$, with $\beta = -1.41 \pm 0.05$ and $\beta = -1.11 \pm 0.12$ for the MHD and MHD* groups respectively, being the first time that this has been done in the core dynamo of an A-type star. It is worth mentioning that negative values of β have been found in data from simulations of other types of stars (Warnecke, 2018; Strugarek et al., 2018; Viviani et al., 2018; Ortiz-Rodríguez et al., 2023).

All the simulations have an approximately rigidly rotating radiative envelope, like the radiative interior of the Sun, and a solar-like differential rotation in the

convective core. The location of the hemispheric dynamo seems to affect the location of the maximum values of the averaged rotation rate, i.e., the magnetic field is quenching the differential rotation. There is no clear difference between the MHD and MHD* groups in their rotation profiles. Furthermore, the zoom zMHD group has similar results as the MHD group as well. However, due to the higher spatial resolution inside the convective core, more and smaller structures are visible, but without changing the main conclusions. Similarly, the magnetic activity of zMHDr2 is very similar to that of MHDr2, having roughly the same configuration and maximum and minimum values. As we increase the rotation rate, the magnetic energy gets closer to the equipartition values with the kinetic energy, and in the fast rotators MHDr4 and MHDr4* both energies are comparable. This nearly equipartition regime was found by Brun et al. (2005), and later in Featherstone et al. (2009). Unlike Augustson et al. (2016), none of our runs reached super-equipartition values. This might be a consequence of the different values of the dimensionless diagnostic parameters in their simulations, e.g. $\mathrm{Re_M}$ and Re are higher than those of our study. All groups have almost the same luminosity profile, which is similar to those presented in Brun et al. (2005) and Augustson et al. (2016). However, it is important to take into account that in the zMHD group the cooling was manually moved within the radiative zone to preserve the thermal equilibrium of the star, because the stellar surface is no longer in the model and therefore, we can not include radiative losses there. Finally, it is worth mentioning that this study contributes to increase the number of available simulations of core dynamos, allowing the first proper assessment of the magnetic activity cycles, with a clear visualization as time-latitude diagrams.

Our simulations indicate that the magnetic field created by a core dynamo is not enough to explain the large-scale structures observed at the surface of Ap/Bp stars. This makes sense considering the wide range of magnetic field strengths observed at the surface of stars whose convective cores are predicted to be of similar size. In future studies, different mechanisms should be included. Although the presence of a strong core dynamo should not be omitted.

As already mentioned, the zoom model has very similar results compared to the whole star model, i.e., no dynamo in the slowest rotator, and a solar-like differential rotation core with a cyclic hemispheric magnetic field in the run with a rotation period of 15 days. However, in the zoom model the magnetic field seems

to be slightly weaker, this is visible from root-mean-square magnetic field $\langle B_{\rm rms} \rangle$ and the magnetic energy $E_{\rm mag}$. This might be something completely related with the resolution. Therefore, although the main results were not affected, performing these simulations in a higher grid might capture some details that change the intensity of the magnetic field.

A logical step to follow in the future is to add a fossil field into our main-sequence model, and study how these magnetic configurations affect the nature of the hemispheric dynamo that was obtained in practically all the magnetic runs. Ideally, as discussed, the input field can be one of the steady configurations found in our protostellar models in Chapter 4. However, different configurations can be implemented as well as a way to test their stability and how they interact with an existing core dynamo, similarly to Featherstone et al. (2009) but also modelling the whole star and seeing how the resulting magnetic field behaves at the stellar surface. Furthermore, more rotation rates can be explored, although it is true that Ap stars can rotate very slow ($P_{\rm rot} = 300$ years), most of them have rotation periods between 1 and 10 days (Braithwaite and Spruit, 2017), so the "fast rotator regime" remains unexplored.

As we already mentioned, the star-in-a-box setup has been used to model fully convective M dwarfs (Käpylä, 2021; Ortiz-Rodríguez et al., 2023), solar-like stars (Käpylä, 2022), and A-type stars. However, in the future it can be used to model different types of stars, like other early-type stars with a bigger convective core, like B-type stars, as well as low mass partially convective stars, and red giants.

Bibliography

Abt, H. A. and Morrell, N. I. (1995). The Relation between Rotational Velocities and Spectral Peculiarities among A-Type Stars. *ApJS*, 99:135.

Andrassy, R., Herwig, F., Woodward, P., and Ritter, C. (2020). 3D hydrodynamic simulations of C ingestion into a convective O shell. *MNRAS*, 491(1):972–992.

Arfken, G. B., Weber, H. J., and Harris, F. E. (2013). Chapter 15 - legendre functions. In Arfken, G. B., Weber, H. J., and Harris, F. E., editors, *Mathematical Methods for Physicists (Seventh Edition)*, pages 715–772. Academic Press, Boston, seventh edition edition.

Augustson, K. C., Brun, A. S., and Toomre, J. (2016). The Magnetic Furnace: Intense Core Dynamos in B Stars. *ApJ*, 829(2):92.

Aurière, M., Wade, G. A., Silvester, J., Lignières, F., Bagnulo, S., Bale, K., Dintrans, B., Donati, J. F., Folsom, C. P., Gruberbauer, M., Hui Bon Hoa, A., Jeffers, S., Johnson, N., Landstreet, J. D., Lèbre, A., Lueftinger, T., Marsden, S., Mouillet, D., Naseri, S., Paletou, F., Petit, P., Power, J., Rincon, F., Strasser, S., and Toqué, N. (2007). Weak magnetic fields in Ap/Bp stars. Evidence for a dipole field lower limit and a tentative interpretation of the magnetic dichotomy. *A&A*, 475(3):1053–1065.

Babcock, H. W. (1947). Zeeman Effect in Stellar Spectra. *ApJ*, 105:105.

Babcock, H. W. (1960). The 34-KILOGAUSS Magnetic Field of HD 215441. *ApJ*, 132:521.

Baraffe, I., Clarke, J., Morison, A., Vlaykov, D. G., Constantino, T., Goffrey, T., Guillet, T., Le Saux, A., and Pratt, J. (2023). A study of convective core overshooting as a function of stellar mass based on two-dimensional hydrodynamical simulations. *MNRAS*, 519(4):5333–5344.

Bartelmann, M. (2021). *Theoretical Astrophysics: An Introduction.*

Becerra, L., Reisenegger, A., Valdivia, J. A., and Gusakov, M. E. (2022). Evolution of random initial magnetic fields in stably stratified and barotropic stars. *MNRAS*, 511(1):732–745.

Bernstein, I. B., Frieman, E. A., Kruskal, M. D., and Kulsrud, R. M. (1958). An

Energy Principle for Hydromagnetic Stability Problems. *Proceedings of the Royal Society of London Series A*, 244(1236):17–40.

Biermann, L. (1932). Untersuchungen über den inneren Aufbau der Sterne. IV. Konvektionszonen im Innern der Sterne. (Veröffentlichungen der Universitäts-Sternwarte Göttingen, Nr. 27.) Mit 5 Abbildungen. *Z. Astrophys.*, 5:117.

Böhm-Vitense, E. (1958). Über die Wasserstoffkonvektionszone in Sternen verschiedener Effektivtemperaturen und Leuchtkräfte. Mit 5 Textabbildungen. *Z. Astrophys.*, 46:108.

Boyer, D. W. and Levy, E. H. (1984). Oscillating dynamo magnetic field in the presence of an external nondynamo field - The influence of a solar primordial field. *ApJ*, 277:848–861.

Braithwaite, J. (2008). On non-axisymmetric magnetic equilibria in stars. *MNRAS*, 386(4):1947–1958.

Braithwaite, J. and Nordlund, Å. (2006). Stable magnetic fields in stellar interiors. *A&A*, 450(3):1077–1095.

Braithwaite, J. and Spruit, H. C. (2017). Magnetic fields in non-convective regions of stars. *Royal Society Open Science*, 4(2):160271.

Brandenburg, A. and Dobler, W. (2002). Hydromagnetic turbulence in computer simulations. *Computer Physics Communications*, 147(1-2):471–475.

Brandenburg, A., Mathur, S., and Metcalfe, T. S. (2017). Evolution of Co-existing Long and Short Period Stellar Activity Cycles. *ApJ*, 845(1):79.

Brandenburg, A., Nordlund, A., and Stein, R. F. (2000). Astrophysical convection and dynamos. In *Geophysical and Astrophysical Convection*, pages 85–105.

Brandenburg, A., Saar, S. H., and Turpin, C. R. (1998). Time Evolution of the Magnetic Activity Cycle Period. *ApJ*, 498(1):L51–L54.

Brandenburg, A. and Sarson, G. R. (2002). Effect of Hyperdiffusivity on Turbulent Dynamos with Helicity. *Phys. Rev. Lett.*, 88(5):055003.

Brandenburg, A. and Subramanian, K. (2005). Astrophysical magnetic fields and nonlinear dynamo theory. *Phys. Rep.*, 417(1-4):1–209.

Briquet, M. (2015). Magnetic fields in O-, B- and A-type stars on the main sequence. In *European Physical Journal Web of Conferences*, volume 101 of *European Physical Journal Web of Conferences*, page 05001.

Brown, B. P., Oishi, J. S., Vasil, G. M., Lecoanet, D., and Burns, K. J. (2020). Single-hemisphere Dynamos in M-dwarf Stars. *ApJ*, 902(1):L3.

Browning, M. K. (2008). Simulations of Dynamo Action in Fully Convective Stars. *ApJ*, 676(2):1262–1280.

Browning, M. K., Brun, A. S., and Toomre, J. (2004). Simulations of Core Convection in Rotating A-Type Stars: Differential Rotation and Overshooting. *ApJ*, 601(1):512–529.

Brun, A. S., Browning, M. K., and Toomre, J. (2005). Simulations of Core Convection in Rotating A-Type Stars: Magnetic Dynamo Action. *ApJ*, 629(1):461–481.

Buresti, G. (2015). A note on stokes' hypothesis. *Acta Mechanica*, 226(10):3555–3559.

Cantiello, M. and Braithwaite, J. (2011). Magnetic spots on hot massive stars. *A&A*, 534:A140.

Cantiello, M., Langer, N., Brott, I., de Koter, A., Shore, S. N., Vink, J. S., Voegler, A., Lennon, D. J., and Yoon, S. C. (2009). Sub-surface convection zones in hot massive stars and their observable consequences. *A&A*, 499(1):279–290.

Chan, K. L. and Sofia, S. (1986). Turbulent Compressible Convection in a Deep Atmosphere. III. Tests on the Validity and Limitation of the Numerical Approach. *ApJ*, 307:222.

Charbonneau, P. (2014). Solar dynamo theory. *Annual Review of Astronomy and Astrophysics*, 52(1):251–290.

Charbonneau, P. (2020). Dynamo models of the solar cycle. *Living Reviews in Solar Physics*, 17(1):4.

Choudhuri, A. R. (1998). *The Physics of Fluids and Plasmas: An Introduction for Astrophysicists*. Cambridge University Press.

Cowling, T. G. (1945). On the Sun's general magnetic field. *MNRAS*, 105:166.

Cox, J. P. and Giuli, R. T. (1968). *Principles of stellar structure*.

Davidson, P. (2002). An introduction to magnetohydrodynamics. *American Journal of Physics*, 70:781.

Dobler, W., Stix, M., and Brandenburg, A. (2006). Magnetic Field Generation in Fully Convective Rotating Spheres. *ApJ*, 638(1):336–347.

Featherstone, N. A., Browning, M. K., Brun, A. S., and Toomre, J. (2009). Effects of Fossil Magnetic Fields on Convective Core Dynamos in A-type Stars. *ApJ*, 705(1):1000–1018.

Gough, D. (1977). The current state of stellar mixing-length theory. In Spiegel, E. A. and Zahn, J. P., editors, *Problems of Stellar Convection*, volume 71, pages 15–56.

Grunhut, J. H., Wade, G. A., Neiner, C., Oksala, M. E., Petit, V., Alecian, E., Bohlender, D. A., Bouret, J. C., Henrichs, H. F., Hussain, G. A. J., Kochukhov, O., and MiMeS Collaboration (2017). The MiMeS survey of Magnetism in

Massive Stars: magnetic analysis of the O-type stars. *MNRAS*, 465(2):2432–2470.

Guerrero, G., Zaire, B., Smolarkiewicz, P. K., de Gouveia Dal Pino, E. M., Kosovichev, A. G., and Mansour, N. N. (2019). What Sets the Magnetic Field Strength and Cycle Period in Solar-type Stars? *ApJ*, 880(1):6.

Hale, G. E. (1908). On the Probable Existence of a Magnetic Field in Sun-Spots. *ApJ*, 28:315.

Hayashi, C., Hōshi, R., and Sugimoto, D. (1962). Evolution of the Stars. *Progress of Theoretical Physics Supplement*, 22:1–183.

Heger, A., Langer, N., and Woosley, S. E. (2000). Presupernova Evolution of Rotating Massive Stars. I. Numerical Method and Evolution of the Internal Stellar Structure. *ApJ*, 528(1):368–396.

Hidalgo, J. P., Käpylä, P. J., Ortiz-Rodríguez, C. A., Navarrete, F. H., Toro, B., and Schleicher, D. R. G. (2023). Origin of magnetism in early-type stars. *arXiv e-prints*, page arXiv:2303.10707.

Hoover, W., Ladd, A., Hickman, R., and Holian, B. (1980). Bulk viscosity via nonequilibrium and equilibrium molecular dynamics. *Physical Review A - PHYS REV A*, 21:1756–1760.

Howe, R. (2009). Solar Interior Rotation and its Variation. *Living Reviews in Solar Physics*, 6(1):1.

Iglesias, C. A., Rogers, F. J., and Wilson, B. G. (1992). Spin-Orbit Interaction Effects on the Rosseland Mean Opacity. *ApJ*, 397:717.

Johansen, A. and Klahr, H. (2005). Dust Diffusion in Protoplanetary Disks by Magnetorotational Turbulence. *ApJ*, 634(2):1353–1371.

Jones, S., Andrassy, R., Sandalski, S., Davis, A., Woodward, P., and Herwig, F. (2017). Idealized hydrodynamic simulations of turbulent oxygen-burning shell convection in 4π geometry. *MNRAS*, 465(3):2991–3010.

Joyce, M. and Tayar, J. (2023). A Review of the Mixing Length Theory of Convection in 1D Stellar Modeling. *Galaxies*, 11(3):75.

Käpylä, P. J. (2021). Star-in-a-box simulations of fully convective stars. *A&A*, 651:A66.

Käpylä, P. J. (2022). Solar-like Dynamos and Rotational Scaling of Cycles from Star-in-a-box Simulations. *ApJ*, 931(2):L17.

Käpylä, P. J., Gent, F. A., Olspert, N., Käpylä, M. J., and Brandenburg, A. (2020). Sensitivity to luminosity, centrifugal force, and boundary conditions in spherical shell convection. *Geophysical and Astrophysical Fluid Dynamics*, 114(1-2):8–34.

Käpylä, P. J., Korpi, M. J., Brandenburg, A., Mitra, D., and Tavakol, R. (2010). Convective dynamos in spherical wedge geometry. *Astronomische Nachrichten*, 331(1):73.

Käpylä, P. J., Mantere, M. J., Cole, E., Warnecke, J., and Brandenburg, A. (2013). Effects of Enhanced Stratification on Equatorward Dynamo Wave Propagation. *ApJ*, 778(1):41.

Kippenhahn, R., Ruschenplatt, G., and Thomas, H. C. (1980). The time scale of thermohaline mixing in stars. *A&A*, 91(1-2):175–180.

Kippenhahn, R., Weigert, A., and Weiss, A. (2013). *Stellar Structure and Evolution*.

Kochukhov, O. (2021). Magnetic fields of M dwarfs. *A&ARv*, 29(1):1.

Kochukhov, O. and Bagnulo, S. (2006). Evolutionary state of magnetic chemically peculiar stars. *A&A*, 450(2):763–775.

Krause, F. and Oetken, L. (1976). On Equatorially Symmetric Models for Magnetic Stars as Suggested by Dynamo Theory. In Weiss, W. W., Jenkner, H., and Wood, H. J., editors, *IAU Colloq. 32: Physics of Ap Stars*, page 29.

Krause, F. and Rädler, K. H. (1980). *Mean-field magnetohydrodynamics and dynamo theory*.

Landstreet, J. D. and Mathys, G. (2000). Magnetic models of slowly rotating magnetic Ap stars: aligned magnetic and rotation axes. *A&A*, 359:213–226.

Lignières, F., Petit, P., Böhm, T., and Aurière, M. (2009). First evidence of a magnetic field on <ASTROBJ>Vega</ASTROBJ>. Towards a new class of magnetic A-type stars. *A&A*, 500(3):L41–L44.

Lyra, W., McNally, C. P., Heinemann, T., and Masset, F. (2017). Orbital Advection with Magnetohydrodynamics and Vector Potential. *AJ*, 154(4):146.

MacDonald, J. and Mullan, D. J. (2004). Magnetic fields in massive stars: dynamics and origin. *MNRAS*, 348(2):702–716.

MacGregor, K. B. and Cassinelli, J. P. (2003). Magnetic Fields in Massive Stars. II. The Buoyant Rise of Magnetic Flux Tubes through the Radiative Interior. *ApJ*, 586(1):480–494.

Markey, P. and Tayler, R. J. (1973). The adiabatic stability of stars containing magnetic fields. II. Poloidal fields. *MNRAS*, 163:77–91.

Markey, P. and Tayler, R. J. (1974). The adiabatic stability of stars containing magnetic fields-III. Additional results for poloidal fields. *MNRAS*, 168:505–514.

Mathys, G. (2008). Extremely slowly rotating magnetic Ap stars: recent results. *Contributions of the Astronomical Observatory Skalnate Pleso*, 38(2):217–222.

Mathys, G. (2015). (Very) Slow Rotation of Magnetic Ap Stars. In Balega, Y. Y., Romanyuk, I. I., and Kudryavtsev, D. O., editors, *Physics and Evolution of Magnetic and Related Stars*, volume 494 of *Astronomical Society of the Pacific Conference Series*, page 3.

Michaud, G. (1970). Diffusion Processes in Peculiar a Stars. *ApJ*, 160:641.

Mitchell, J. P., Braithwaite, J., Reisenegger, A., Spruit, H., Valdivia, J. A., and Langer, N. (2015). Instability of magnetic equilibria in barotropic stars. *MNRAS*, 447(2):1213–1223.

Moss, D. (1989). The origin and internal structure of the magnetic fields of the CP stars. *MNRAS*, 236:629–644.

Moss, D. (2001). Magnetic Fields in the Ap and Bp Stars: a Theoretical Overview. In Mathys, G., Solanki, S. K., and Wickramasinghe, D. T., editors, *Magnetic Fields Across the Hertzsprung-Russell Diagram*, volume 248 of *Astronomical Society of the Pacific Conference Series*, page 305.

Moss, D. (2003). The survival of fossil magnetic fields during pre-main sequence evolution. *A&A*, 403:693–697.

Ortiz-Rodríguez, C. A., Käpylä, P. J., Navarrete, F. H., Schleicher, D. R. G., Mennickent, R. E., Hidalgo, J. P., and Toro-Velásquez, B. (2023). Simulations of dynamo action in slowly rotating M dwarfs: Dependence on dimensionless parameters. *A&A*, 678:A82.

Parker, E. N. (1955). Hydromagnetic Dynamo Models. *ApJ*, 122:293.

Parker, E. N. (1979). The Instability of a Horizontal Magnetic Field in an Atmosphere Stable Against Convection. *Ap&SS*, 62(1):135–142.

Paxton, B., Bildsten, L., Dotter, A., Herwig, F., Lesaffre, P., and Timmes, F. (2011). Modules for Experiments in Stellar Astrophysics (MESA). *ApJS*, 192(1):3.

Paxton, B., Cantiello, M., Arras, P., Bildsten, L., Brown, E. F., Dotter, A., Mankovich, C., Montgomery, M. H., Stello, D., Timmes, F. X., and Townsend, R. (2013). Modules for Experiments in Stellar Astrophysics (MESA): Planets, Oscillations, Rotation, and Massive Stars. *ApJS*, 208(1):4.

Paxton, B., Marchant, P., Schwab, J., Bauer, E. B., Bildsten, L., Cantiello, M., Dessart, L., Farmer, R., Hu, H., Langer, N., Townsend, R. H. D., Townsley, D. M., and Timmes, F. X. (2015). Modules for Experiments in Stellar Astrophysics (MESA): Binaries, Pulsations, and Explosions. *ApJS*, 220(1):15.

Paxton, B., Schwab, J., Bauer, E. B., Bildsten, L., Blinnikov, S., Duffell, P., Farmer, R., Goldberg, J. A., Marchant, P., Sorokina, E., Thoul, A., Townsend, R. H. D., and Timmes, F. X. (2018). Modules for Experiments in Stellar Astrophysics (MESA): Convective Boundaries, Element Diffusion, and Massive Star Explosions. *ApJS*, 234(2):34.

Paxton, B., Smolec, R., Schwab, J., Gautschy, A., Bildsten, L., Cantiello, M., Dotter, A., Farmer, R., Goldberg, J. A., Jermyn, A. S., Kanbur, S. M., Marchant, P., Thoul, A., Townsend, R. H. D., Wolf, W. M., Zhang, M., and Timmes, F. X. (2019). Modules for Experiments in Stellar Astrophysics (MESA): Pulsating Variable Stars, Rotation, Convective Boundaries, and Energy Conservation. *ApJS*, 243(1):10.

Pencil Code Collaboration, Brandenburg, A., Johansen, A., Bourdin, P., Dobler, W., Lyra, W., Rheinhardt, M., Bingert, S., Haugen, N., Mee, A., Gent, F., Babkovskaia, N., Yang, C.-C., Heinemann, T., Dintrans, B., Mitra, D., Candelaresi, S., Warnecke, J., Käpylä, P., Schreiber, A., Chatterjee, P., Käpylä, M., Li, X.-Y., Krüger, J., Aarnes, J., Sarson, G., Oishi, J., Schober, J., Plasson, R., Sandin, C., Karchniwy, E., Rodrigues, L., Hubbard, A., Guerrero, G., Snodin, A., Losada, I., Pekkilä, J., and Qian, C. (2021). The Pencil Code, a modular MPI code for partial differential equations and particles: multipurpose and multiuser-maintained. *The Journal of Open Source Software*, 6(58):2807.

Petit, P., Böhm, T., Folsom, C. P., Lignières, F., and Cang, T. (2022). A decade-long magnetic monitoring of Vega. *A&A*, 666:A20.

Petit, P., Lignières, F., Aurière, M., Wade, G. A., Alina, D., Ballot, J., Böhm, T., Jouve, L., Oza, A., Paletou, F., and Théado, S. (2011). Detection of a weak surface magnetic field on Sirius A: are all tepid stars magnetic? *A&A*, 532:L13.

Petit, P., Lignières, F., Wade, G. A., Aurière, M., Böhm, T., Bagnulo, S., Dintrans, B., Fumel, A., Grunhut, J., Lanoux, J., Morgenthaler, A., and Van Grootel, V. (2010). The rapid rotation and complex magnetic field geometry of Vega. *A&A*, 523:A41.

Petitdemange, L., Marcotte, F., and Gissinger, C. (2023a). Spin-down by dynamo action in simulated radiative stellar layers. *Science*, 379(6629):300–303.

Petitdemange, L., Marcotte, F., Gissinger, C., and Daniel, F. (2023b). Tayler-Spruit dynamos in simulated radiative stellar layers. *arXiv e-prints*, page arXiv:2306.11711.

Pols, O. (2011). *Stellar Structure and Evolution*. Astronomical Institute Utrecht.

Prandtl, L. (1925). 7. Bericht über Untersuchungen zur ausgebildeten Turbulenz. *Zeitschrift Angewandte Mathematik und Mechanik*, 5(2):136–139.

Richard, O., Michaud, G., and Richer, J. (2001). Iron convection zones in b, a, and f stars. *The Astrophysical Journal*, 558(1):377.

Rossby, C.-G. (1939). Relation between variations in the intensity of the zonal circulation of the atmosphere and the displacements of the semi-permanent centers of action. *Journal of Marine Research*, 2:38–55.

Royer, F., Zorec, J., and Gómez, A. E. (2007). Rotational velocities of A-type stars. III. Velocity distributions. *A&A*, 463(2):671–682.

Schekochihin, A. (2021). Lectures on kinetic theory and magnetohydrodynamics of plasmas. *University of Oxford*.

Schleicher, D. R. G., Hidalgo, J. P., and Galli, D. (2023). Survival of fossil fields during the pre-main sequence evolution of intermediate-mass stars.

Schleicher, D. R. G. and Mennickent, R. E. (2017). A dynamo mechanism as the potential origin of the long cycle in double periodic variables. *A&A*, 602:A109.

Schmidt, A. (1917). Deutsche Meteorologische Gesellschaft. *Naturwissenschaften*, 5(47):710–711.

Schuessler, M. and Paehler, A. (1978). Diffusion of a strong internal magnetic field through the radiative envelope of a 2.25 M sun-star. *A&A*, 68(1-2):57–62.

Sharma, B. and Kumar, R. (2019). Estimation of bulk viscosity of dilute gases using a nonequilibrium molecular dynamics approach. *Phys. Rev. E*, 100:013309.

Siess, L., Dufour, E., and Forestini, M. (2000). An internet server for pre-main sequence tracks of low- and intermediate-mass stars. *A&A*, 358:593–599.

Spruit, H. C. (2002). Dynamo action by differential rotation in a stably stratified stellar interior. *A&A*, 381:923–932.

Steenbeck, M., Krause, F., and Rädler, K.-H. (1966). Berechnung der mittleren lorentz-feldstärke für ein elektrisch leitendes medium in turbulenter, durch coriolis-kräfte beeinflußter bewegung. *Zeitschrift für Naturforschung A*, 21(4):369–376.

Strugarek, A., Beaudoin, P., Charbonneau, P., and Brun, A. S. (2018). On the Sensitivity of Magnetic Cycles in Global Simulations of Solar-like Stars. *ApJ*, 863(1):35.

Tayler, R. J. (1973). The adiabatic stability of stars containing magnetic fields-I.Toroidal fields. *MNRAS*, 161:365.

Taylor, G. I. (1915). Eddy Motion in the Atmosphere. *Philosophical Transactions of the Royal Society of London Series A*, 215:1–26.

Vitense, E. (1953). Die Wasserstoffkonvektionszone der Sonne. Mit 11 Textabbildungen. *Z. Astrophys.*, 32:135.

Viviani, M., Warnecke, J., Käpylä, M. J., Käpylä, P. J., Olspert, N., Cole-Kodikara, E. M., Lehtinen, J. J., and Brandenburg, A. (2018). Transition from axi- to nonaxisymmetric dynamo modes in spherical convection models of solar-like stars. *A&A*, 616:A160.

Warnecke, J. (2018). Dynamo cycles in global convection simulations of solar-like stars. *A&A*, 616:A72.

Weiss, A., Hillebrandt, W., Thomas, H.-C., and Ritter, H. (2004). *Cox and Giuli's Principles of Stellar Structure*, volume -1.

Welch, P. (1967). The use of fast fourier transform for the estimation of power spectra: A method based on time averaging over short, modified periodograms. *IEEE Transactions on Audio and Electroacoustics*, 15(2):70–73.

Williamson, J. (1980). Low-storage runge-kutta schemes. *Journal of Computational Physics*, 35(1):48–56.

Wright, G. A. E. (1973). Pinch instabilities in magnetic stars. *MNRAS*, 162:339–358.